0 0 0 0 5 4 0 0 6 7 1 5

UC-34 ~~UC-34a~~

LBL-9527 c.1

Lawrence Berkeley Laboratory

UNIVERSITY OF CALIFORNIA

Materials & Molecular Research Division

PHOTOELECTRON SPECTROSCOPY OF HEAVY ATOMS AND MOLECULES

Michael George White
(Ph.D. thesis)

July 1979

RECEIVED
LAWRENCE
BERKELEY LABORATORY

FEB 21 1980

LIBRARY AND
DOCUMENTS SECTION

For Reference

Not to be taken from this room

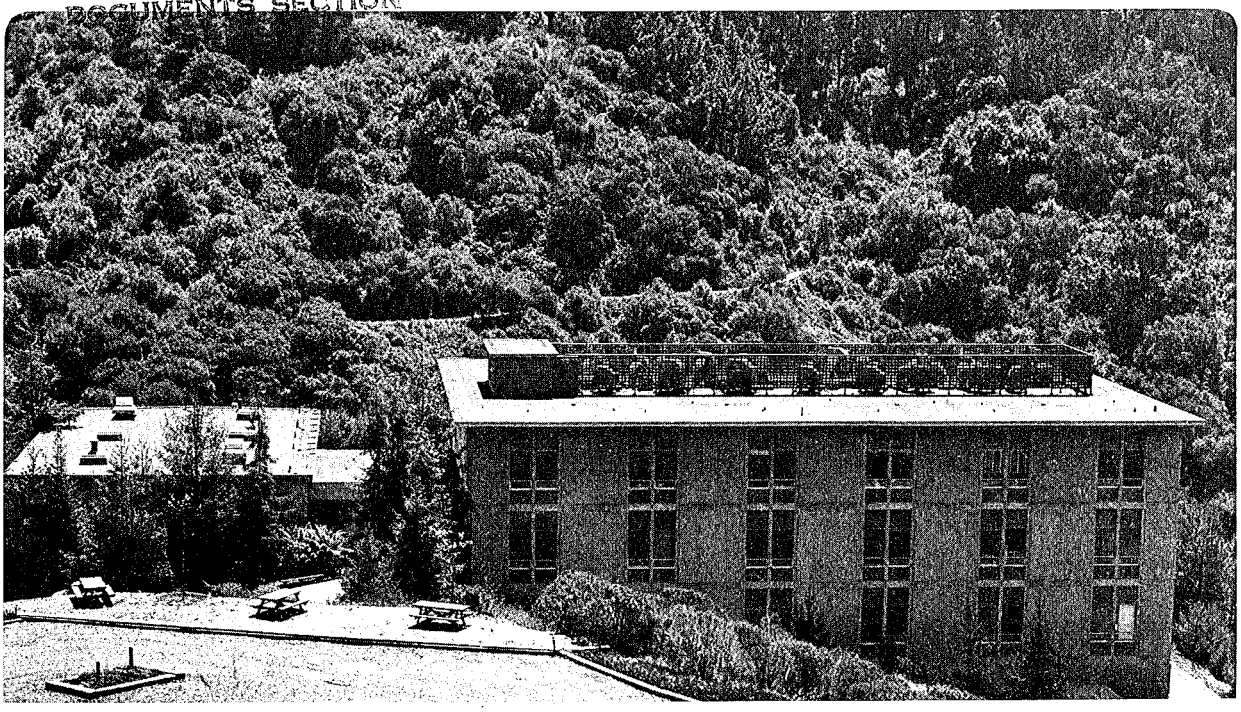

LBL-9527 c.1

Prepared for the U.S. Department of Energy under Contract W-7405-ENG-48

DISCLAIMER

Photoelectron Spectroscopy of Heavy Atoms and Molecules

Michael George White
Lawrence Berkeley Laboratory

Abstract

The importance of relativistic interactions in the photoionization of heavy atoms and molecules has been investigated by the technique of photoelectron spectroscopy. In particular, experiments are reported which illustrate the effects of the spin-orbit interaction in the neutral ground state, final ionic states and continuum states of the photoionization target.

Both synchrotron radiation and a conventional laboratory radiation source (HeI) were employed as excitation sources for the photoelectron measurements. Laboratory experiments were performed on a commercial photoelectron spectrometer which had been highly-modified for high-temperature studies. A gas-phase time-of-flight (TOF) photoelectron spectrometer was designed and built for use at the Stanford Synchrotron Radiation Laboratory (SSRL). The TOF apparatus exploits the excellent time structure and high degree of linear polarization of the synchrotron radiation available at SSRL to measure photoelectron angular distributions with high efficiency and medium energy resolution (≤3%).

The angular distribution of Xe 5s→εp photoelectrons was measured at kinetic energies near the Cooper minimum. The measured asymmetry parameters, β_{5s}, differ markedly from the non-relativistic value of 2 as a direct consequence of spin-orbit effects in the continuum. Additional angular distribution measurements were performed on HBr and HI where the asymmetry parameters for the $(p\pi)_{3/2}$ and $(p\pi)_{1/2}$ orbitals were found

to be equal (within experimental uncertainty) despite the large spin-orbit splittings of these heavy molecules. Finally, the general electronic structures of the heavy Group IV-VI diatomics GeO, GeS, GeSe, GeTe, SnS, SnSe, SnTe were investigated through their HeI photoelectron spectra. Particular attention was paid to the influence of spin-orbit interactions in the final ionic states of these systems.

Table of Contents

Chapter		Page
I	Introduction	1
	A. General Aspects of Photoelectron Spectroscopy	1
	B. Relativistic Effects in Photoionization	4
	References Chapter I	8
II	Experimental	10
	A. Introduction	10
	B. Properties of Synchrotron Radiation	12
	C. Time-of-Flight Photoelectron Spectroscopy of Gases Using Synchrotron Radiation	14
	References Chapter II	30
III	Spin-Orbit Effects in the Xe 5s → εp Photoelectron Angular Distribution	62
	A. Theoretical Description of the ns → εp Photoelectron Angular Distributions of the Rare Gases	63
	B. Experimental	69
	C. Results and Discussion	70
	References Chapter III	75
Appendix A - Dipole Matrix Elements in jj Coupling		80
	References Appendix A	83
Appendix B - Determination of LS-jj Coupling Transformation for $Xe(5s\varepsilon p)_{J=1}$ Final States		84
	References Appendix B	88
IV	The Photoelectron Angular Distributions of HBr and HI at $h\nu = 21.2$ eV	89
	A. Introduction	90
	B. Experimental	91
	C. Results and Discussion	92

Table of Contents (continued)

Chapter		Page
	References Chapter IV.	98
V	The He I Photoelectron Spectroscopy of Heavy Group IV-VI Diatomics. The GeX (X = O, S, Se, Te) and SnX(X = S, Se, Te) Diatomics	104
	A. Introduction	105
	B. Experimental	106
	C. Theory	108
	D. Results.	111
	1. The GeX Series	112
	2. The SnX Series	116
	E. Discussion	118
	References Chapter V	125
Appendix C -	Evaluation of the $\mathcal{H}_{so}$ Matrix Elements for the Group IV-VI Diatomics	143
	References Appendix C.	148
Acknowledgements		149

Chapter I

Introduction

This thesis is primarily concerned with the investigation of relativistic effects in heavy atoms and molecules through the use of photoelectron spectroscopy. Although photoelectron spectroscopy has been used to study the electronic structure of atoms and molecules for over a decade, only a handful of these experiments have been concerned with relativistic perturbations in the photoionization of heavy atoms and molecules.[1] This situation is partly the result of the experimental difficulties in producing the heavier species in the gas-phase, i.e., most relativistic systems require high-temperature vaporization. In addition, certain experiments require the use of a tunable radiation source in the vacuum ultraviolet (VUV) and soft x-ray regions, which until the advent of sccessible synchrotron radiation facilities in recent years, did not exist. In this work are presented the results of photoelectron measurements on relativistic systems which have necessitated high temperature techniques and the use of synchrotron radiation.

A. General Aspects of Photoelectron Spectroscopy

Before discussing relativistic effects in photoionization in more detail, it is useful to introduce the reader to some of the basic concepts and relationships upon which the discussions presented in latter chapters are based. The general photoionization reaction is given by

$$A(\Psi_N^{(0)}) + h\nu \rightarrow A^+(\Psi_I^{(f)}) + e^-(f) \quad f = 0,1,2,\ldots \tag{1}$$

where the neutral atom or molecule is in its ground state $\Psi_N^{(0)}$ and

ionization leaves the target in either its ground ($f = 0$) or higher excited ionic states $\Psi_I^{(f)}$ ($f = 1,2,\ldots$). The kinetic energy of the detected photoelectron associated with the ionic state f is given by the familiar conservation expression

$$KE(f) = h\nu - BE(f), \tag{2}$$

where BE(f) the "binding energy" of the ejected electron is given by

$$BE(f) = E(\Psi_I^{(f)}) - E(\Psi_N^{(0)}). \tag{3}$$

The energies on the r.h.s. of the above equation are appropriate for the full hamiltonians for the N-1 and N electron systems, respectively. The use of the term "binding energy" as defined in Equation (3) originates from the use of the single-particle Hartree-Fock approximation for constructing the eigenfunctions $\Psi_I^{(f)}$ and $\Psi_N^{(0)}$. In this approximation, better known as Koopman's theorem,[2] Equation (3) becomes

$$BE(f)_{HF} = -\varepsilon_f \tag{4}$$

where ε_f is the usual HF eigenvalue or binding energy of the electron in the orbital f. This expression is the basis for much qualitative interpretation in photoelectron spectroscopy, since many of the features in the photoionization of atoms and molecules can be well understood in terms of the initial orbitals. We note, however, that Equation (4) explicitly neglects the effects of relaxation of the final state and many-electron correlation effects, both which can be very important for the accurate prediction of binding energies and photoionization intensities.[3]

Of considerable importance in latter discussions is the differential photoionization cross section which in the dipole approximation is given by[4-6]

$$\frac{d\sigma_{f\leftarrow i}}{d\Omega} = \frac{\sigma_{f\leftarrow i}}{4\pi}\left(1 + \beta_{f\leftarrow i}\, P_2(\cos\theta)\right) \tag{5}$$

where $\sigma_{f\leftarrow i}$ is the integrated cross section for the photoionization transition from initial state i to final state f(ion core plus photoelectron), $\beta_{f\leftarrow i}$ is the asymmetry parameter, $P_2(x)$ is the second order Legendre polynomial, $\frac{3}{2}x^2 - 1/2$, and θ is the angle between the photoelectron direction and the polarization vector of the radiation. Equation (5) is appropriate for randomly oriented targets and linearly polarized radiation although analogous formulae for other radiation polarizations have also been derived.[7] The integrated cross section appearing in Equation (5) is given by

$$\sigma_{f\leftarrow i} = \frac{4}{3}\pi^2 \alpha a_0 h\nu \sum_k \left|\langle \Psi_I^{(f)}(N-1)\Psi_\epsilon^{(k)}(1)\left|\vec{u}\cdot\vec{\nabla}\right|\Psi_I^{(0)}(N)\rangle\right|^2 \tag{6}$$

where ν and $\vec{u}$ are the frequency and polarization vector of the radiation, α is the fine structure constant (1/137), a_0 is the Bohr radius (5.29×10^{-9} cm) and where we have explicitly shown the final state as including both the ionic core and continuum wavefunctions. The sum over k represents the fact that more than one continuum wave may couple with the ionic core to give the correct overall symmetry required for a dipole process from the ground state. Again, it is useful to employ the Hartree-Fock approximation for constructing the state functions in Equation (6), i.e., determinantal wavefunctions built-up from one-electron orbitals, by which the dipole matrix element becomes[3]

$$|\langle\Psi_I^{(f)}(N-1),\ \Psi_\epsilon^{(k)}(1)|\vec{u}\cdot\vec{\nabla}|\Psi_I^{(0)}(N)\rangle|^2_{HF}$$

$$= |\langle\Psi_\epsilon^{(k)}(1)|\vec{u}\cdot\vec{\nabla}|\phi_f(1)\rangle|^2 \qquad (7)$$

where we have implicitly ignored relaxation of the final state and where ϕ_f is the orbital from which the electron has been removed. Because of its computational tractability, Equation (7) has found great utility in the interpretation of photoelectron spectra.

It is clear from Equation (5) that the angular distribution is completely characterized by the asymmetry parameter, $\beta_{f\leftarrow i}$. In general, the asymmetry parameter can vary between -1 and 2 as function of kinetic energy; this energy dependence is a consequence of variations in the transition strengths to the dipole allowed continuum channels (Eqn. (7)), variations of the continuum phase shifts and the *interference* between these terms. In these respects, angular distribution measurements are *a priori* much more powerful than cross section experiments, since the contribution of individual continuum channels can be determined rather than just the sum of these contributions (see Eqn. (6)). Theoretical expressions for $\beta_{f\leftarrow i}$ have been derived at various levels of approximation and coupling conditions for atoms[6,8] and molecules.[9] These expressions will be discussed in more detail in Chapters III and IV with particular reference to the influence of relativistic effects on the asymmetry parameter.

B. Relativistic Effects in Photoionization

The most important and most readily identifiable relativistic perturbation in the photoelectron spectra of heavy systems is the spin-orbit (s-o) interaction. Other perturbations, such as the mass-velocity and

the Darwin relativistic "s-shift" corrections,[10] are "intrinsic" properties of the orbitals, since they affect primarily the energy positions of these levels. Hence, these effects can only be investigated in photoelectron spectroscopy by the comparative study of a series of related systems in which these effects are large enough to be observable as a definite trend from the non-relativistic to relativistic systems.[11] The effects of the s-o interaction are "extrinsic" in that they can lead to additional peaks in the photoelectron spectrum of an isolated relativistic atom or molecule and can also have a strong influence on the energies and intensities of these peaks.

In particular, the effects of s-o interactions as observed in photoionization can be roughly separated into three categories:

1. Initial State s-o Interactions
2. Final Ionic State s-o Interactions
3. Continuum State s-o Interactions.

Spin-orbit effects in the initial state refers primarily to perturbations of the initial one-electron orbitals. For atoms (molecules) the s-o interaction leads to differences between the radial functions of the $j = \ell + 1/2$ ($\omega = \lambda + 1/2$) and $j = \ell - 1/2$ ($\omega = \lambda - 1/2$) components of an $n\ell(n\lambda)$ orbital (ℓ, $\lambda > 0$).[12] Hence, the resulting photoionization cross sections and angular distributions will be different for the two s-o states. These effects are most important for those orbitals which penetrate closest to the nucleus, for example, atomic np ($\ell = 1$) shells show greater deviations from the non-relativistic limit than nd($\ell = 2$) or nf($\ell = 3$) shells.[13] In addition, the s-o interaction can also cause different closely-lying multiplets of the same total angular momentum and parity to be mixed (intermediate coupling) into the initial state

wavefunction. This effect has been shown to be extremely important for the rationalization of peak intensities in the photoelectron spectra of open shell systems.[14]

As described above, the s-o interaction can lead to the mixing of multiplets of different spin and orbital angular momentum but of the same total angular momentum and parity. For relativistic molecules these interactions are more often observed in their final ionic states, since most have closed shell ground states and ionization leads to many closely spaced ionic state multiplets of different symmetry. The s-o configuration mixing affects both the energy and the character, e.g., σ or π, of the resulting intermediately coupled wavefunctions and has been shown to be very important for understanding the ionic state level structure of several relativistic molecules.[15] In addition, the relaxation of symmetry conditions for configuration mixing of multiplets within the final ionic states makes many-electron correlation effects increasingly important for relativistic systems. These s-o induced correlation effects can lead to the appearance of additional "satellite" lines which represent photoelectric excitation to ionic states which are normally forbidden by dipole processes.

Analogous to initial state perturbations, continuum s-o interactions are interpreted in terms of the differences between the s-o components of the continuum orbitals. In general, these interactions are very difficult to isolate from differences in the initial bound orbitals. For example, in atomic photoionization the dipole selection rule $\Delta j = 0, \pm 1$ (appropriate for jj coupling) leads to three possible continuum channels for ionization from each of the s-o $(n\ell)_{j=\ell\pm 1/2}$ bound states. Without some *a priori* knowledge of the strengths of the individual photoionization channels it is very difficult to assign differences in the resulting

photoelectron cross section or angular distributions to differences in the continuum orbitals due to s-o effects. For $ns_{1/2}$ shell ionization, however, dipole selection rules restrict the continuum channels to $\varepsilon p_{1/2}$ and $\varepsilon p_{3/2}$ waves only. Hence, in this case where there are no s-o effects on the bound orbital, continuum s-o interactions can be studied directly. In general, s-o interactions on continuum orbitals are very small[13] and even for $ns_{1/2}$ ionization lead to only small deviations from the non-relativistic result at most photon energies. At photon energies near Cooper minima, where in the non-relativistic limit the nl photoionization cross section is zero, s-o effects are "amplified" and dramatic deviations from the non-relativistic limit can occur which can be interpreted directly in terms of the different s-o continuum channels.[16]

The above separation of the effects of spin-orbit coupling is somewhat artificial, since in many instances all three types play an important and indistinguishable role in the photoionization of a relativistic system. In the chapters that follow, however, each system or group of related systems illustrates mainly the effects of s-o coupling from one of the above categories. In Chapter III the effects of continuum s-o interactions are discussed in detail in regards to the photoelectron angular distribution of the 5s subshell of atomic Xe. The effects of s-o coupling on the initial π orbitals of the hydrogen halide molecules is considered in Chapter IV and Chapter V includes the effects of s-o interactions in the final ionic states of the heavy Group IV-VI diatomic molecules.

References Chapter I

1. For recent reviews of photoelectron spectroscopy including relativistic effects see: J. L. Dehmer, Journal De Physique, Supplement #7, 39, C4-42 (1978); G. V. Marr, Introduction to the Theory of Photoelectron Spectroscopy for Experimentalists, Daresbury Laboratory, Lecture Notes #2, 1975; T. E. H. Walker and J. T. Waber, J. Phys., B7, 674 (1974).

2. Note that Equation (4) was first derived by Koopmans using Hartree product wavefunctions which do not properly treat the Pauli exclusion principle. It is a trivial exercise, however, to prove that Equation (4) is also correct for properly asymmetrized HF determinantal wavefunctions, see T. Koopmans, Physica, 1, 104 (1933).

3. For an excellent discussion on relaxation and many-electron effects in photoionization see: R. L. Martin, Ph.D. Thesis, University of California, LBL-5167 (1976).

4. H. A. Bethe, In Handbuch der Physik, eds. H. Geiger and K. Sheel (Springer-Verlag, Berlin), Vol. 24/1, p. 482.

5. C. N. Yang, Phys. Rev., 24, 764 (1948).

6. J. Cooper and R. N. Zare, J. Chem. Phys., 48, 942 (1968).

7. V. L. Jacobs, J. Phys., B5, 2257 (1972); J. A. R. Samson, Phil. Trans. Roy. Soc., A268, 141 (1970); V. Schmidt, Phys. Lett., A45, 63 (1973).

8. U. Fano and D. Dill, Phys. Rev., A6, 185 (1972); T. E. H. Walker and J. T. Waber, J. Phys., B6, 1165 (1973); D. Dill, A. F. Starace and S. T. Manson, Phys. Rev., A11, 1596 (1975); M. Ya. Amusia and N. A. Cherepkov, Case Studies in At. Phys., 5, 47 (1975).

9. A. D. Buckingham, B. J. Orr and J. M. Sichel, Phil. Trans. Roy. Soc., A268, 147 (1970); J. C. Tully, R. S. Berry and B. J. Dalton, Phys. Rev., 176, 95 (1968); Y. Itikawa, Chem. Phys., 28, 461 (1978).

10. For a general discussion of relativistic perturbations, see F. Herman and S. Skillman, Atomic Structure Calculations (Prentice-Hall, Englewood Cliffs, NJ, 1963), Chapter 2.

11. The effects of the mass-velocity and Darwin relativistic perturbations have been studied in photoelectron spectra of Tl, Pb and Bi solids. See R. A. Pollak, L. Ley, S. Kowalczyk and D. A. Shirley, Phys. Lett., A41, 429 (1972).

12. Here ℓ and j refer to the orbital and total angular momentum (jj coupling) and λ and ω are the molecular analogues except that they represent the projections of angular momenta on the internuclear axis (ω,ω coupling).

13. See the second citation under Reference (8).

14. S. Süzer, M. S. Banna and D. A. Shirley, J. Chem. Phys., 63, 3473 (1975); S.-T. Lee, S. Süzer and D. A. Shirley, Chem. Phys. Lett., 41, 25 (1976).

15. See Chapter V and references therein.

16. N. A. Cherepkov, Phys. Lett., A66, 204 (1978).

17. W. R. Johnson and K. T. Cheng, Phys. Rev. Lett., 40, 1167 (1978).

Chapter II

Experimental

A. Introduction

In this chapter, the experimental apparatus used to obtain the data presented in the remaining chapters is discussed in detail. It is appropriate that this chapter should be a major part of this thesis, since much of my time as a graduate student was spent in the laboratory performing the rituals of "nutzin and boltzin." My experimental work fell into two categories:

(i) Photoelectron spectroscopy of high temperature molecular vapors employing standard laboratory photon sources.

(ii) Time-of-Flight photoelectron spectroscopy of gases using synchrotron radiation.

The experiments included in the first category were performed on a commercial UV photoelectron spectrometer (Perkin-Elmer PS-18) modified for high temperature work. This spectrometer was the "workhorse" of the gas-phase group for several years and from this work evolved important new insights into the effects of electron correlation on the photoionization of heavy atoms.[1] The studies on heavy molecules were initiated after the observation of Bi_2^+ in the photoelectron spectrum of bismuth vapor.[2] On the suggestion of Dr. Shuit-Tong Lee*, I began the study of the large class of Group IV-VI diatomics, the results of which are discussed in Chapter V. Although the resolution of the spectrometer was not ideally suited for molecular studies ($\Delta E \sim 80$ meV),

---

* Present address, Kodak Research Laboratories, Rochester, NY.

it was sufficient to resolve the main features of the level structure of these ions. The high-temperature oven and spectrometer have been ably described elsewhere[3,4] and additional details pertaining to individual experiments can be found in Chapter V.

This chapter is primarily concerned with the description of the time-of-flight (TOF) photoelectron spectrometer which was built for use with synchrotron radiation. Because of its wide tunability and high degree of linear polarization, synchrotron radiation permits the study of the energy and angular dependence of a wide range of photoionization processes not possible with conventional laboratory sources. With this impetus and the close proximity of the Stanford Synchrotron Radiation Laboratory (SSRL), design of the spectrometer was begun in the summer of 1977. The "prototype" instrument with a single TOF analyzer was used at Stanford in June, 1978. The data obtained during this run was suspect for a number of reasons, the most damaging being poor magnetic shielding, and needed to be repeated. Because of a combination of inadequate beam time and storage-ring down time over the next year (1978-1979), most of the single analyzer experiments could not be redone. In this same period, however, I collaborated with Richard Rosenberg* on the resonant photoelectron spectroscopy of Ba vapor using synchrotron radiation and the TOF spectrometer.[5] In April, 1979, the second TOF analyzer was added to the spectrometer and angular distribution experiments were attempted in May and June, 1979. Again (and frustratingly so) we were confronted with storage-ring difficulties during our scheduled run and most of our experiments were left untried except for those

---

* Present address, Michelson Laboratories, China Lake, CA.

presented in this thesis. It should be noted, however, that these few successful experiments clearly indicated the usefulness and potential of the TOF spectrometer for the study of photoionization processes.

B. Properties of Synchrotron Radiation

As is well-known, a non-relativistic electron ($v/c \ll 1$) which is confined to an orbital path by a centripetal acceleration, emits radiation in the characteristic dipole pattern (case I, Fig. 1). At relativistic velocities, however, the emission pattern is dramatically altered and the radiation is confined to the forward direction of the electron's motion (case II, Fig. 1). The general properties of this synchrotron radiation[6] and its applications to a variety of spectroscopies[7] has been extensively reviewed in recent years. Those characteristics of synchrotron radiation which are of particular relevance to the TOF apparatus are summarized below.

(i) Continuous Energy Spectrum: synchrotron radiation provides high intensity over a broad spectral range from the near infra-red through the vacuum ultraviolet (VUV) to the x-ray region. The "high flux" part of the above statement is particularly true in the x-ray region ($h\nu \geq 1$ KeV) where synchrotron radiation sources provide more than 100,000 times more flux than state-of-the-art rotating anode x-ray tubes.[8] In the VUV, however, the intensity is one to two orders of magnitude lower than that of standard rare gas discharge lamps which are commonly used in laboratory photoelectron spectrometry. In addition, the line width of the discharge radiation is very narrow, i.e., essentially the atomic line width (~.1 Å for the HeI line @ 21.2 eV), whereas the band pass on most VUV synchrotron radiation beam line monochromators must be kept to ≥1 Å to maintain useable flux for photoelectron measurements. This disadvantage in flux, however, is more than offset by the wide tunability of synchrotron radiation.

(ii) Time Structure: synchrotron radiation sources have an inherent time structure governed by the orbital period of the electron bunches in the storage ring. The synchrotron radiation produced at the Stanford Positron Electron Accelerator Ring (SPEAR) operating in the single-bunch

mode is pulsed, with a pulse width of ~ 300 psec and pulse repetition period of 780 nsec.[9] This time structure is particularly well suited for timing experiments on the nanosecond time scale and has been used for fluorescence decay measurements,[10,11] and as described in this chapter, time-of-flight electron measurements.

(iii) Highly Polarized: synchrotron radiation emitted from the storage ring is highly plane polarized (≥ 75%) parallel to the plane of the electron orbit. By careful design of the optical geometries within individual beam lines, e.g., all vertical reflections, the polarization can be further increased to ≥95%. That the polarization of the radiation should be important for TOF photoelectron measurements can be seen by considering the expressions for the differential photoionization cross sections for unpolarized and linearly polarized radiation

$$\frac{d\sigma}{d\Omega} = \frac{\sigma}{4\pi}\left[1 - \frac{\beta}{2} P_2(\cos\gamma)\right]_{un}$$

$$\frac{d\sigma}{d\Omega} = \frac{\sigma}{4\pi}\left[1 + \beta P_2(\cos\theta)\right]_{lin}.$$

where σ, β and $P_2(x)$ have been defined in Chapter I and γ is the angle between the ejected electron and propagation vector of the unpolarized radiation, and θ is the angle between the ejected photoelectron and the polarization vector of the linearly polarized light. Since the goal of angularly resolved measurements is to determine β, we see that the expression for unpolarized light is less sensitive (by a factor of 2) to changes in the angle γ than the corresponding equation for linearly polarized light is to changes in θ. Hence, angular measurements employing unpolarized light must have a higher accuracy to obtain a β value with statistics equal to that obtained from lower accuracy experiments with linearly polarized light. This difference in sensitivity to the angular distribution has important consequences for our TOF apparatus since β values are calculated from measurements at <u>only two</u> angles.

(iv) Highly Collimated: as shown in Figure 1, synchrotron radiation is highly collimated in the forward direction with an extremely small vertical divergence given by $\theta_v \sim mc^2/E$ where E is the electron energy (for typical operating conditions at SPEAR, E = 2.5 GeV and $\theta_v \sim .27$ mrad). This high collimation leads to small source dimensions, typically 2 mm × 2 mm in cross section. As discussed below, the source size plays a critical role in determining the overall energy resolution of the TOF apparatus.

C. Time-of-Flight Photoelectron Spectroscopy of Gases Using Synchrotron Radiation*

1. General

The unique features of synchrotron radiation as a vacuum ultraviolet (VUV) light source offer tremendous advantages over laboratory sources for the study of photoionization processes in atoms and molecules. The tunability and high degree of linear polarization of synchrotron radiation allows the study of photoionization cross sections and angular distributions over a wide range of electron kinetic energies. Such data are particularly useful for the critical evaluation of theoretical models describing the interactions between the ion core and the continuum electron. In addition, direct resonant excitation to highly excited Rydberg levels of the neutral species (which subsequently autoionize into the ionization continuum) is made possible. Thus the basic electronic structure of these Rydberg levels and their coupling to the excited ionic states can be investigated directly.

Photoelectron spectroscopy of gases using present day synchrotron radiation sources, however, is a comparatively low counting rate experiment. This is a result of both the relatively small photon fluxes available in the VUV (typically $<10^{11}$ sec^{-1} - cm^{-2}) and the small sample densities ($<10^{14}$ cm^{-3}) normally employed in gas-phase photoelectron measurements. Also, angle-resolved experiments require an angular resolution of at least ±5°, implying a collection solid angle of $\leq 10^{-2}$ sterdians. These factors lead to typical counting rates of 10 - 100 sec^{-1}, depending on the cross section of the species being studied. It is

---

* A summary of this work was published in collaboration with R. A. Rosenberg, G. Gabor, E. D. Poliakoff, G. Thornton, S. H. Southworth and D. A. Shirley, Rev. Sci. Instrum., 50, 53 (1979).

therefore imperative to develop very efficient electron analyzers to avoid prohibitively long counting times. To date nearly all gas-phase photoelectron experiments using synchrotron radiation have employed electrostatic deflection electron analyzers, either a 127° cylindrical mirror sector[13] or a cylindrical mirror analyzer.[14] Although these analyzers have high resolving capabilities, they are intrinsically inefficient because only electrons in a narrow energy range are collected at any one time.

An alternative and much more efficient method of electron kinetic energy analysis is by the time-of-flight (TOF) technique. A TOF analyzer measures the time required for a photoelectron to travel over a fixed distance of field free space after an ionizing event. Using standard timing/coincidence techniques, TOF analysis permits the entire energy spectrum within a given time window to be analyzed simultaneously. The counting efficiency is therefore increased relative to the more conventional deflection-type analyzers by a factor equal to the number of collecting channels (typically 10^3). Since all the peaks in a given spectrum are collected simultaneously it is not necessary to normalize relative peak areas for fluctuations in sample pressure and beam decay. In addition, because TOF is a coincidence technique, random background contributions such as electron multiplier dark noise are equally divided among the time channels of a collection window which includes the entire repetition period of the pulsed source. Hence, the background contribution to any given time channel is significantly reduced and signal-to-background ratios of 1:1 or smaller can be tolerated. Because the actual collection time window is normally smaller than the full repetition period, a further improvement in the total signal-to-background ratio is obtained.

In practice, TOF analysis requires either a pulsed radiation source or, in the case of continuous excitation, that the electrons be pulsed from the interaction region by applied external fields. The latter approach suffers from the disadvantages that photoelectrons are produced continuously, introducing additional background and broadening of peaks and that the collection solid angle varies with electron kinetic energy. Unfortunately, with laboratory photon sources in the VUV it is generally not feasible to attain the repetition frequencies (≥10 KHz) and small pulse widths (≤1 nsec) necessary for optimal electron TOF measurements. The pulsed nature of synchrotron radiation from large storage rings, however, provides an ideal time base for electron TOF analysis. Recently, Bachrach, et al.,[15] performed solid state photoemission experiments employing a prototype TOF analyzer and the pulsed synchrotron radiation at the Stanford Positron Electron Accelerator Ring (SPEAR). These measurements clearly established the feasibility and usefulness of the TOF technique based on pulsed synchrotron radiation.

In this chapter the design of a gas-phase photoelectron spectrometer employing a TOF electron energy analyzer is discussed. TOF detection is facilitated by the excellent time structure (0.3 nsec pulse width and a 780 nsec repetition period) of the radiation produced at SPEAR. These timing characteristics are ideal for electron TOF analysis because the very narrow pulse imparts only a small kinetic energy spread to the ejected electrons (40 meV at 10 eV). Furthermore, the relatively long repetition period permits kinetic energies from 1 eV to several hundred eV to be analyzed using practical drift tube lengths (~30 cm).

The TOF apparatus described here is significantly different from other gas-phase TOF instruments using VUV radiation recently developed by Tsai, et al.,[16] and Guyon, et al.[17] In those spectrometers only

near-threshold (≤1 eV) photoelectrons are detected, and they are collected over large solid angles, yielding spectra which are somewhat angle-integrated. These limitations would preclude certain studies of autoionization phenomena and photoelectron anisotropies. Because synchrotron radiation is ideally suited for probing resonant phenomena and angular distributions, our TOF detector was designed to analyze electrons over a wide energy range at medium energy resolution and high angular resolution.

2. Apparatus

The TOF apparatus shown schematically in Figure 2 was designed for experiments on the 8° beam line at the Stanford Synchrotron Radiation Laboratory (SSRL). A detailed description of this facility is given elsewhere.[18] Briefly, 3.2 milliradians of radiation from the storage ring is subtended by a mirror and focused onto the grating of 1-meter Seya-Namioka monochromator (GCA/McPherson). The radiation entering the sample chamber is 97% polarized in the horizontal plane. Photon energies of between 4 eV and 36 eV are available with the optics presently employed on the 8° line.

After final focusing, the beam passes through the window isolation fore chamber located between two pneumatically operated gate valves (Torr Vacuum). This section of the apparatus is used to isolate the sample chamber, which is operated at a relatively high pressure of $\sim 2 \times 10^{-5}$ Torr, from the monochromator and beam line in which pressures below 10^{-9} Torr are maintained. Isolation is accomplished by ultra-thin (~1500 Å) In and Aℓ windows which are capable of withstanding differential pressures of up to 1 Torr and have acceptable transmission for the photon energies of interest.[19] For typical running conditions of 2×10^{-5} Torr

in the sample chamber, the leak rate through the windows is estimated to be $\sim 10^{-9}$ Torr-ℓ-sec^{-1}. This leakage is pumped by a small ion pump (Hi-Q, Varian) located on the window isolation section with an effective pumping speed of ~1 ℓ-sec^{-1}. This arrangement is sufficient to insure the vacuum integrity of the beam line without the necessity of multiple-stage differential pumping chambers. In addition, the pneumatic gate valve closest to the beam line was specially constructed for fast closing (<300 msec) and is fully interlocked against vacuum failures which would burst the window.

In Figure 3 we show the relative photon flux versus photon energy for the 8° beam line at SSRL employing both the In and Aℓ windows. The relative flux represents a combination of the throughput of the Seya-Namioka monochromator and the transmission of the two windows. At the peak transmittance wavelength, ~570 Å, the photon flux is estimated to be 5×10^{9} sec^{-1} - cm^{-2} for typical operating conditions of 2 Å band pass and 10 mA SPEAR electron ring current. A sodium salicylate scintillator and optical phototube (RCA, 8850) are used to continuously monitor the beam intensity.

The gas sample enters the vacuum chamber through a 1 mm diameter disc of 10 μm diameter, 1 mm long microchannels (Galileo Corp.) located approximately 5 mm above the interaction volume (see Fig. 4). The microchannel array serves to collimate the gas source, increasing the forward intensity over that of a simple effusive source of the same backing pressure. Based on the work of Johnson, et al.,[20] and Jones, et al.,[21] we estimate the increase in forward intensity, the "peaking factor",[21] to be ~7 for a 5 Torr backing pressure with a half-intensity beam angle of $\Theta_{\frac{1}{2}} = 6.5°$. Here $\Theta_{\frac{1}{2}}$ is defined by $I(\Theta_{\frac{1}{2}})/I(0°) = \frac{1}{2}$. This can be

compared to the 60° half intensity angle of an effusive beam source, indicating that significant collimation is achieved by expansion through the channel array. Backing pressures typically ranged between 5 Torr and 20 Torr as measured by a capacitance manometer (MKS Instruments, Inc.) and were controlled by an interfaced servo-driven variable leak valve (Granville-Phillips). At these backing pressures, the particle density is predicted to be $\sim 10^{13}$ cm^{-3}, which is consistent with the observed photoelectron counting rates. The resultant gas jet is pumped by two 500 ℓ-sec^{-1} turbo-molecular pumps (Airco Temescal) mounted on the main vacuum chamber which maintain a background pressure of $\sim 2 \times 10^{-5}$ Torr.

3. Time-of-Flight Analyzer

Photoelectrons enter the TOF analyzer through a 2.[illegible] mm orifice located 2.3 cm from the center of the interaction region. The orifice collimates the ejected electron signal and also acts as a conduction barrier between the sample chamber and detector housing for the purpose of differential pumping. A total flight path of 28.5 cm was chosen to give an angular acceptance of ±3° and is limited by the diameter of the active area of the electron detector (2.84 cm). This angular resolution represents a compromise between limiting the variation in electron flight paths, which degrades the overall energy resolution, and insuring a sufficient collection solid angle (8.6×10^{-3} sr). Typical flight times for this distance are 480 nsec and 96 nsec for 1 eV and 25 eV electrons, respectively.

The drift tube is constructed from aluminum and provides the electrostatic shield for the field free flight path. The entire flight tube as well as the detector assembly is gold plated to eliminate contact

potentials. In addition, the inside of the drift tube was coated with a colloidal graphite spray to reduce secondary electron emission caused by photoelectrons striking the walls of the shield. The entire flight path, from the interaction point to electron multiplier, was magnetically shielded by a combination of high permeability μ-metal cylinders surrounding the flight tube and the central volume of the vacuum chamber (see Fig. 2). The residual magnetic field in the drift space was measured to be less than 20 mG. The TOF analyzer with its electrostatic and magnetic shields is shown in Figures 5 and 6.

The electron amplifier is a tandem pair of microchannel plates (MCP) whose output is collected on a conical anode (Fig. 7). The MCP amplifier is similar in design to those recently employed for fast timing measurements of nuclear particles[22] and heavy ions[23,24] and the TOF electron detectors of Kennerly[25] and Bachrach, et al.[15] The general operating characteristics of MCP's and their timing capabilities have been discussed in detail in the literature cited above and hence will not be repeated here. It is sufficient to note that because of the small time dispersion in a MCP's amplifying process, single particle events can be timed with a resolution of <100 psec.

The electrons which have drifted through the field free region are accelerated by 100 V before impinging on the first MCP. The MCP's electron detection efficiency is >96% and is uniform for input kinetic energies of 100 eV to 700 eV.[26] Two MCP's (Varian Series 8900, 40 mm diameter, 8° bias angle) in a Chevron arrangement were employed as the subnanosecond amplifier with up to 10^7 gain. Bias voltages from a divider chain (shown schematically in Fig. 7; see also Fig. 8) were applied to the front and rear conducting surfaces of each MCP through

.05 mm thick gold-plated brass rings. The contact rings between the two MCP's were isolated by a .05 mm Mylar spacer, giving a total separation of .15 mm between the two MCP's. The emerging electron cascade is collected on a coaxial anode whose surface diameter (2.84 cm) determines the useful active area of the detector. The coaxial anode cone is designed to have the impedance of the anode increase from a minimum value of 16 Ω at the collection surface to the output impedance of 50 Ω. In this way a larger collection surface area is possible for a given MCP geometry than with a coaxial design in which the entire anode is fixed at 50 Ω impedance. The anode shield is coupled to the back surface of the second MCP by a capacitor made from .5 mm double faced printed circuit board. The anode is at a virtual ground with respect to the anode shield, but the whole anode assembly is floated at the full positive high voltage potential. A fast coaxial transformer (see Fig. 9) decouples the output signal to ground reference before passing through a high vacuum floating-shield coaxial BNC feedthrough (Ceramaseal, Inc.).

At an applied voltage of 2.5 kV, the detector provides a gain of 10^6 and a dark noise count rate of 1 - 10 sec^{-1}. The output pulses are very sharp, with a 10% - 90% rise time of ≤.5 nsec and pulse amplitudes of ~75 mV.

4. Electronics

Photoelectron spectra are generated using the photon-electron coincidence counting circuit shown schematically in Figure 7. Pulses from the electron multiplier are first amplified (×9) and discriminated. Because of the poor electron signal pulse height distributions (characteristic of MCP amplifiers),[27] it was necessary to employ a zero-crossing or constant fraction discriminator (CFD) to reduce the time "jitter" in

the output timing signals. The CFD's used in this work were designed and built by G. Gabor (Electronics Engineering, LBL) and have a measured time "jitter" of ≤20 psec. The CFD output is then used as a start signal for the time-to-amplitude converter (TAC). The stop pulse is provided by a signal from an induction coil located in the storage ring. This arrangement of stop and start signals avoids reset-time losses in the TAC. The pulse-height spectrum is then analyzed and accumulated in a multichannel analyzer. The data can then be plotted or transferred to magnetic tape for latter analysis.

5. Resolution

The energy resolution for TOF analysis is given by[28]

$$\left(\frac{\Delta E}{E}\right)_{TOF} = \sqrt{\left(\frac{2\Delta t}{t}\right)^2 + \left(\frac{2\Delta \ell}{\ell}\right)^2} \qquad (1)$$

where Δt and $\Delta \ell$ represent the total time resolution of the apparatus and the electron flight path uncertaintv, respectively. The time resolution of the TOF detector system is determined by the timing capabilities of the electron multiplier and associated electronics, folded together with the time width of the synchrotron beam pulse. Timing dispersion in the MCP amplifier and electronics is <70 psec and the width (FWHM) of the synchrotron radiation pulse varies from 150 psec to 400 psec depending on the operating conditions of SPEAR. Furthermore, the pulse shape is in general neither gaussian in time nor constant for different electron beam currents.[29] The overall timing resolution of the apparatus was measured directly by the observation of prompt (Rayleigh) photon scattering from the gas sample. A prompt pulse is shown in Figure 10. The measured FWHM of ~300 psec leads to an energy resolution contribution from timing factors of 40 meV at 10 eV and represents the limiting resolution of our TOF apparatus when employed at SSRL.

Differences in the photoelectron flight paths ($\Delta\ell$) result from the finite source volume and finite collection solid angle. The spread in electron flight paths due to the angular acceptance of ±3 contributes only a small energy uncertainty of .25%. A much larger contribution to $\Delta\ell$ results from the relatively large interaction volume from which the photoelectrons originate. With the present focusing optics on the 8° beam line, the photon beam cross section (FWHM) is 2.2 mm high by 1.9 mm wide at the interaction point. Furthermore, the single analyzer experiments were conducted at the "magic angle" (54.7° with respect to the photon polarization vector), hence, the horizontal beam profile at the source point is increased to ~3.3 mm. This source length leads to a flight path dispersion of ~2.3%. Because the intersection of the photon beam and gas jet is better described by a line source than a point source, this number actually represents a lower limit to the path length dispersion. Since this dispersion dominates the first term of Eqn. (1), the energy resolution $(\Delta E/E)_{TOF}$ is essentially constant over the kinetic energy range of 1 to 50 eV.

Although it is possible to use space focusing to reduce or eliminate the energy spread caused by the finite source width,[28] the accompanying restrictions on the other design parameters of the TOF analyzer are severe. In the single acceleration field design, the length of the drift region is restricted to $\ell = 2s$ where s is the distance between the extraction elements. Hence, only near-threshold electrons can be analyzed, i.e., the first term in Eqn. (1) is kept small.[16] In both the single and double accelerating field system described in Ref. 28, the electrons are extracted from the ionization region; hence, the effective

angular acceptance of the analyzer is large and it varies with the kinetic energy of the electrons.

The total energy resolution is given by

$$\left(\frac{\Delta E}{E}\right)_{TOTAL} = \sqrt{\left(\frac{\Delta E}{E}\right)^2_{TOF} + \left(\frac{\Delta\lambda}{\lambda}\right)^2} \qquad (2)$$

where λ is the wavelength of the exciting radiation and $\Delta\lambda$ the monochromator band pass. The loss of intensity at higher resolution limited the usable band pass to 2.5 Å in the work presented here. For λ = 584 Å (21.2 eV), $\Delta\lambda/\lambda$ = .4% and 10 eV photoelectrons, the total energy resolution is ~2.4%. This overall resolution is sufficient to resolve the vibrational structure of many small molecular ions and is also adequate for the separation of spin-orbit substates of heavy atoms and molecules.

6. Performance

The TOF photoelectron spectrum of the 5p shell of atomic Xe at $h\nu$ = 21.2 eV is shown in Figure 11. This spectrum was recorded in only 5 minutes and represents the time-to-energy converted raw data. The marked asymmetry of the peaks towards lower energies is again due to the "magic angle" geometry employed. This results in the analyzer accepting more electrons with longer flight paths and hence apparent lower kinetic energies.

The measured resolution for both the $^2P_{1/2}$ and $^2P_{3/2}$ ionic states was found to be ~3%, in reasonable agreement with the predicted value of 2.4%. The discrepancy presumably arises from an underestimation of the source volume used to calculate the energy resolution as discussed above. Although a resolution of 3% at 10 eV is somewhat inferior in comparison to deflection-type analyzers (typically, ≤1%), it is as good or better

than previous TOF electron analyzers. In the low energy (≤2 eV) electron spectrometers of Tsai, et al.,[16] Land, et al.,[30] Baldwin,[31] and Wilden, et al.,[32] energy resolutions ($\Delta E/E$) of 10% at 50 meV, 6% at 150 meV, 13% at 1 eV and 3.3% at 1 eV, respectively, were reported. Because the resolving capabilities of those spectrometers are limited by the time resolution of the detector (5-12 nsec), only the first term of Eqn. (1), i.e., $\frac{2\Delta t}{t}$, contributes significantly to the energy resolution. Hence, ΔE is proportional to $E^{3/2}$ and their energy resolution will deteriorate rapidly with increasing kinetic energy. For detection of photoelectrons with energies greater than 1 eV, only the TOF apparatus of Kennerly[25] has better resolution than the present spectrometer (.67% at 12 eV). The time dispersions in both spectrometers are essentially identical (300 psec), however, a longer flight path (50 cm) and much smaller flight path uncertainty ($\Delta \ell$ = .1 cm) significantly improves the overall energy resolution obtainable by Kennerly.

From the discussion above it is clear that to improve the energy resolution further, the flight path uncertainty must be reduced. Three approaches which are presently feasible for 8° line work are:

(i) physically reduce the size of the photon beam by apertures or slits. Although simplest, one must deal with a concurrent loss of flux. For experiments on systems of high cross section (≥10 Mb) it appears acceptable as a "quick and dirty" solution.

(ii) refocus the synchrotron beam to smaller spot size. This is a significantly more difficult and expensive approach since the beam must be refocused in both the vertical and horizontal planes. This would require either a torroidal mirror which is extremely expensive and difficult to make or two mirrors which are less expensive and easier to make, however, one now has two reflections instead of one (for VUV radiation each reflection will reduce the flux by 40-60%).

(iii) By the use of 70 mm diameter MCP's (now available from Galileo, Corp.) the flight path can be increased to nearly 60 cm while maintaining the same collection solid angle as the present TOF analyzers. In this way flight path dispersion can be decreased to ~1%.

In the long run the third approach is best, since then the performance of the apparatus is least dependent on the characteristics of the beam line on which it is being used.

7. Angular Distribution Measurements

As discussed in Chapter I, the angular distribution is completely described by the determination of the asymmetry parameter β. Furthermore, measurements at just two angles are sufficient to experimentally determine β. This has been discussed in detail by Huang, et al.,[33] who conclude that it is statistically more accurate to take several measurements at just two angles, than to take the same number of measurements over many angles. In addition, the two measurements are best made at 0° and 90° with respect to the photon polarization vector so that the maximum change in the differential cross section can be exploited (see Eqn. (5), Chap. I). Our spectrometer vacuum chamber was designed along this line of reasoning and can accept TOF analyzers at 0°, 54.7° and 90° with respect to the polarization vector. For the experiments reported in this thesis two identical TOF analyzers were placed at 0° and 54.7°. This particular geometry was chosen over the 0° - 90° combination for the following reasons:

(i) To calibrate the apparatus for the asymmetry in detection efficiencies of the two TOF detectors, a gas of known β must be run. The most convenient and most accurate procedure involves using He as calibrant gas, whose β = 2 for kinetic energies of interest in this work. Unfortunately, the differential cross section is zero at 90° for β = 2 and therefore the calibration procedure is not valid for this geometry. Although other gases have known β values, the available data does not cover a sufficient kinetic energy range and is not of high enough accuracy to be trusted for calibration runs.

(ii) The use of 54.7° instead of 90° has a secondary advantage in that the spectra recorded at 54.7° (the "magic" angle) have no angular dependence and therefore cross section information can be obtained directly.

Since calibration of the apparatus is of critical importance for insuring the quality of subsequent data, we opted for the less rigorous 0° - 54.7° geometry. As higher accuracy data becomes available for the other rare gases (with $\beta \neq 2$), it will be possible to employ them as calibrants in a 0° - 90° geometry.

The apparatus and TOF analyzers used for the angular distribution measurements are identical to that described in Sections 2-6. The measurements are performed by collecting spectra at 0° and 54.7° simultaneously, from which a β for that particular photon energy can be computed. This is accomplished by employing the input routing electronics shown in Figure 12. The output of the two TOF detectors are amplified and discriminated and then teed to a fan-in module and also to the router. The fan-in takes the multiple TOF input and outputs these signals on a single level with the pulses separated by the difference in their arrival times. The fan-in output is then used as start signals for a single TAC which is in coincidence with the beam pulse. Simultaneously, the first signal to the router causes a gate signal to be sent to the TAC, preventing it from being restarted by a subsequent detector pulse. In addition, the router addresses the MCA so that the coincidence output just processed by the TAC is analyzed and stored in a particular quadrant of memory corresponding to one of the TOF analyzers. After the signal has been processed by the MCA the gate to the TAC is "opened" and the next timing event can be analyzed. Because the reset time of the PHA/MCA unit is on the order of 25 μsec, individual TOF signal rates must be <2.5 KHz.[34] In addition, should the signal rate of

one detector be ~2KHz and the other significantly less than this, the high signal detector would continually engage the routing and would prevent the lower signal detector output from being processed. Unfortunately, these high counting rates have not been experienced and these conditions present no real restrictions on our experiments at this time.

After the spectra are collected, the asymmetry parameters for individual peaks can be calculated from

$$\beta_i = \frac{I_i(0°)}{I_i(54.7°)} \cdot \frac{1}{f(E)} - 1 \tag{3}$$

where $I_i(\theta)$ is the area of the ith peak measured at angle θ. The efficiency factor $f(E)$ can be related to physical quantities by the expression

$$f(E) = \frac{\Omega(54.7°)}{\Omega(0°)} \cdot \frac{g(54.7°)}{g(0°)} \tag{4}$$

where $\Omega(\theta)$ and $g(\theta)$ are the solid angle collected and electron multiplier gain of the TOF analyzer at angle θ and where we have explicitly shown the dependence of this ratio on the electron kinetic energy. The efficiency function is obtained empirically from calibration of the apparatus with He as discussed above. A typical efficiency curve is shown in Figure 13. The overall shape is characteristic of the transmission of the TOF analyzers, i.e., the collection efficiency versus kinetic energy, and shows a rapid decrease at lower kinetic energies. This is caused by the fact that the low energy electrons are easily deflected out of the collected solid angle by small external fields and each detector's efficiency changes rapidly in this region. For this curve, the ratio of the two detection efficiencies gives a downward

sloping curve, although this is just a coincidence, and in general, f(E) curves are different for each different SSRL run.

As an example of β measurements using the TOF apparatus, the 0° and 54.7° spectrum of atomic Xe taken at hν = 21.2 eV are shown in Figure 14. The measured β values are $\beta(^2P_{3/2}) = 1.89 \pm .06$ and $\beta(^2P_{1/2}) = 1.59 \pm .05$, in reasonable agreement with the most recent literature values of 1.77 ± .05 and 1.63 ± .05.[35] The differences in β for the two spin-orbit substates results from differences in the $5p_{1/2}$ and $5p_{3/2}$ radial wavefunctions and the kinetic energies of the corresponding photoelectrons.[36] Finally, we note that the 0° detector has higher resolution (ΔE/E~2.5%) than the 54.7° analyzer (~3%). This is a result of the fact that the 0° analyzer, being ⊥ to the photon beam, sees a smaller source cross section (2.2 mm × 1.9 mm) and therefore has a smaller path length dispersion.

References Chapter II

1. See for example S. Süzer, S.-T. Lee and D. A. Shirley, Phys. Rev., A13, 1842 (1976).

2. S. Süzer, S.-T. Lee and D. A. Shirley, J. Chem. Phys., 65, 412 (1976).

3. Sefik Süzer, Ph.D. Thesis, University of California, LBL-4922 (1976).

4. R. A. Rosenberg, Ph.D. Thesis, University of California, LBL-8948 (1979).

5. R. A. Rosenberg, M. G. White, G. Thornton and D. A. Shirley, submitted for publication; see also Ref. (4), Chapter V.

6. See for example, M. L. Perlman, E. M. Rowe and R. E. Watson, Phys. Today, p. 30 (July, 1974).

7. See for example, E. E. Koch and B. F. Sonntag, Molecular Spectroscopy with Synchrotron Radiation, DESY Report #F41-78/02 (May, 1978).

8. I. Lindau and H. Winick, Comments in At. and Mol. Phys., 6, 133 (1977).

9. S. Doniach, I. Lindau, W. E. Spicer and H. Winick, J. Vac. Sci. Technol., 12, 1123 (1975).

10. For a detailed description of timing measurements at SSRL, see K. M. Monahan and V. Rehn, Nucl. Instrum. Methods, 152, 255 (1978).

11. E. D. Poliakoff, Ph.D. Thesis, University of California (1979), unpublished.

12. K. Codling, Rep. Prog. Phys., 36, 541 (1973).

13. See for example, L. Torop, J. Morton, and J. B. West, J. Phys. B9, 2035 (1976).

14. See for example, P. C. Kemeny, J. A. R. Samson, and A. F. Storace, J. Phys. B10, L201 (1977).

15. R. Z. Bachrach, F. C. Brown, and S. B. M. Hagstrom, J. Vac. Sci. Tech. 12, 309 (1975).

16. B. Tasi, T. Baer, and M. L. Horowitz, Rev. Sci. Instrum., 45, 494 (1974).

17. P. M. Guyon, T. Baer, L. F. A. Ferreira, I. Nenner, A. Tabché-Fouhailés, R. Botter, and T. R. Govers, J. Phys. B11, L141 (1978).

18. H. Winick, in VUV Radiation Physics, eds., E. E. Koch, et al. (Pergamon-Vieweg, London/Braunschweig, 1974), p. 780; V. Rehn, et al., in VUV Radiation Physics, eds., E. E. Koch, et al. (Pergamon-Vieweg, London/Braunschweig, 1974), p. 780.

19. Luxell Corporation, Santa Barbara, CA.

20. J. C. Johnson, A. T. Stair, Jr., and J. L. Pritchard, J. Appl. Phys. 37, 1551 (1966).

21. R. H. Jones, D. R. Olander, and V. R. Kruger, J. Appl. Phys. 40, 4641 (1969).

22. M. I. Green, P. F. Kenealy, and G. B. Beard, Nucl. Instrum. and Methods 126, 175 (1975).

23. G. Gabor, W. Schimmerling, D. Greiner, F. Bieser, and P. Lindstrom, Nucl. Instrum. and Methods 130, 65 (1975).

24. J. Girard and M. Bolore, Nucl. Instrum. and Methods 140, 279 (1977).

25. R. E. Kennerly, Rev. Sci. Instrum. 48, 1682 (1977).

26. G. Gabor, to be published.

27. W. B. Colson, J. McPherson and F. T. King, Rev. Sci. Instrum., 44, 1694 (1973).

28. W. C. Wiley and I. H. McLaren, Rev. Sci. Instrum. 26, 1150 (1955).

29. A. P. Saversky, in Abstracts of the Third Annual SSRP Users Group Meeting, Stanford, CA, 1976, p. 46.

30. J. E. Land and W. Raith, Phys. Rev. A9, 1592 (1974).

31. G. C. Baldwin, Phys. Rev. A9, 1225 (1974).

32. D. G. Wilden, P. J. Hicks, and J. Comer, J. Phys. B9, 1959 (1976).

33. J. T. J. Huang, J. W. Rabalais, and F. O. Ellison, J. Electron Spectrosc. and Rel. Phen. 6, 85 (1975).

34. For random input, the signal rate should be ~10 times smaller than the reset time in order to keep peak areas accurate to 1%.

35. J. L. Dehmer, W. A. Chupka, J. Berkowitz and W. T. Jivery, Phys. Rev., A12, 1966 (1975).

36. For a general discussion see T. E. H. Walker and J. T. Waber, J. Phys., B7, 674 (1974).

Figure 1. Characteristics of the radiation emitted by non-relativistic (case I) and relativistic (case II) electrons moving in an orbital path. From Ref. (8).

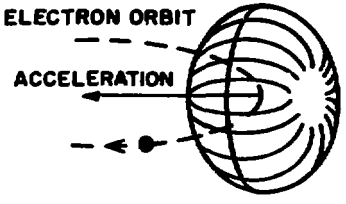

CASE I : $\frac{v}{c} << 1$

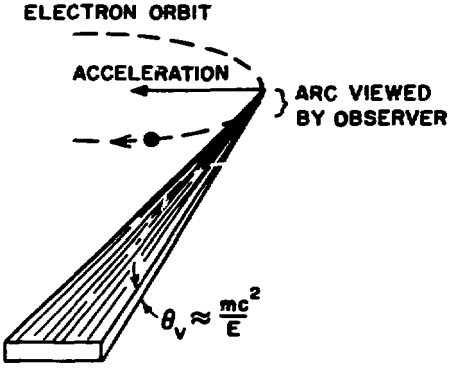

CASE II : $\frac{v}{c} \approx 1$

RADIATION EMISSION PATTERN BY ELECTRONS IN CIRCULAR MOTION

XBL 798-11098

Figure 2. Lay-out of the TOF photoelectron spectrometer. See text for detailed description.

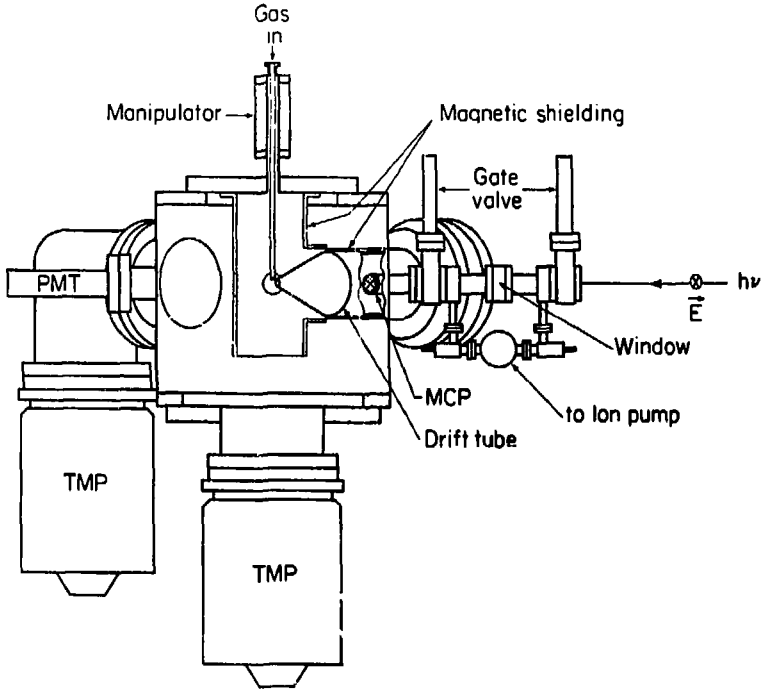
Gas
in
Manipulator
Magnetic shielding
Gate
valve
PMT
hν
E
Window
MCP
to Ion pump
Drift tube
TMP
TMP

XBL 792-8566

Figure 3. Relative transmitted intensity versus photon wavelength for the 8° beam line at SSRL employing In and Al windows.

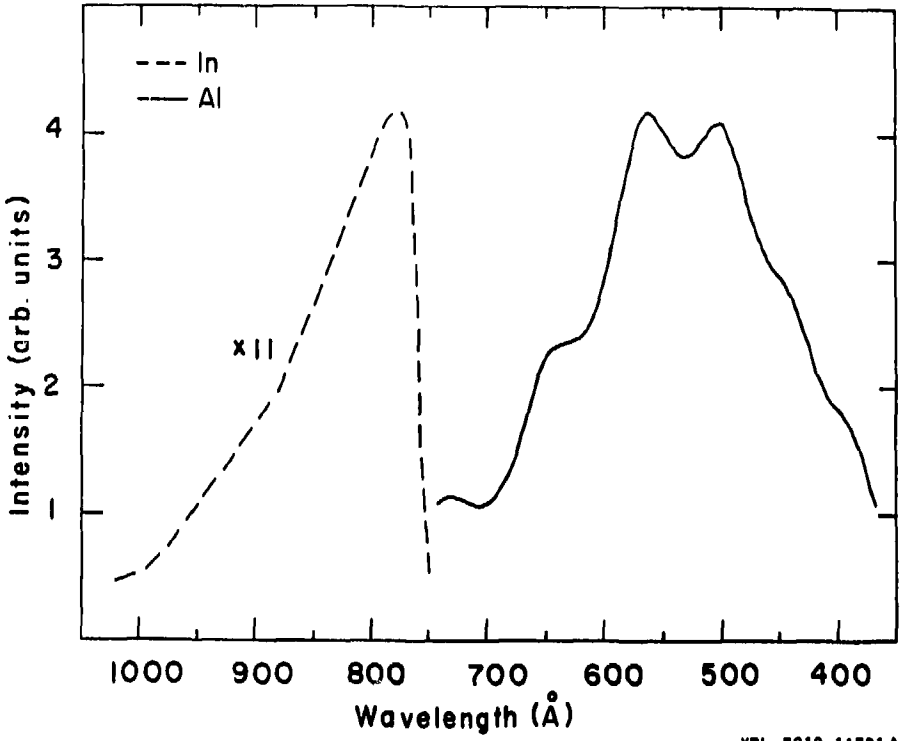

XBL 7810-11701A

Figure 4. Exploded view of gas inlet probe.

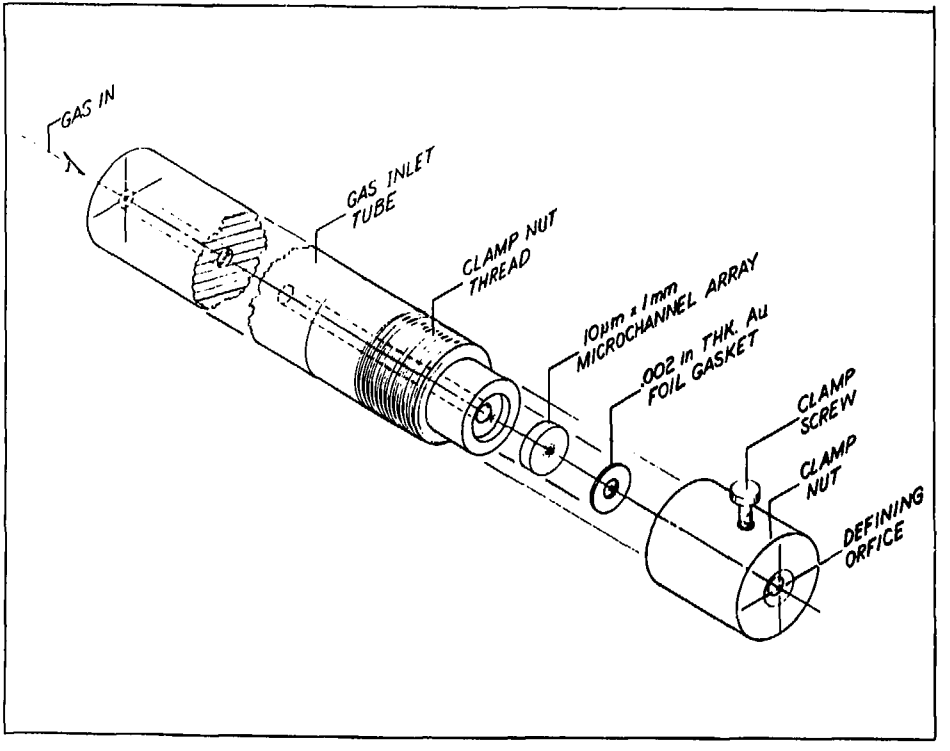

XBL 798-11139

Figure 5. The disassembled TOF analyzer, showing (from left-to-right) the μ-metal shield, detector/electron multiplier and aluminum drift tube with defining aperature.

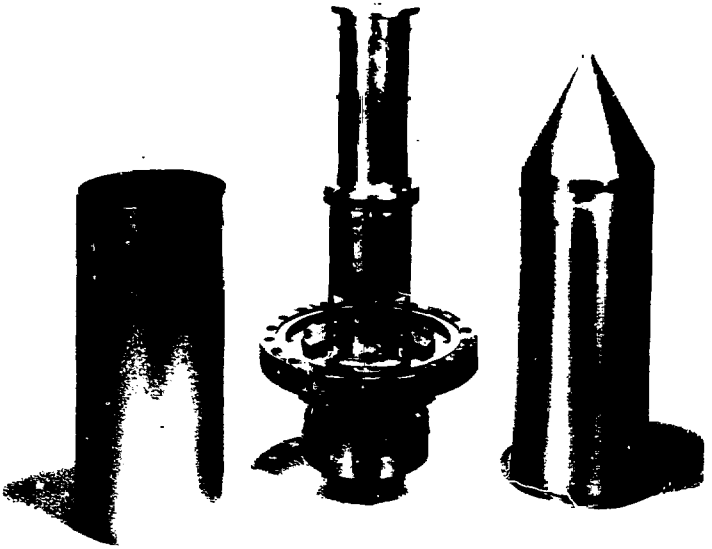

CBB 793-3980

Figure 6. The assembled TOF analyzer.

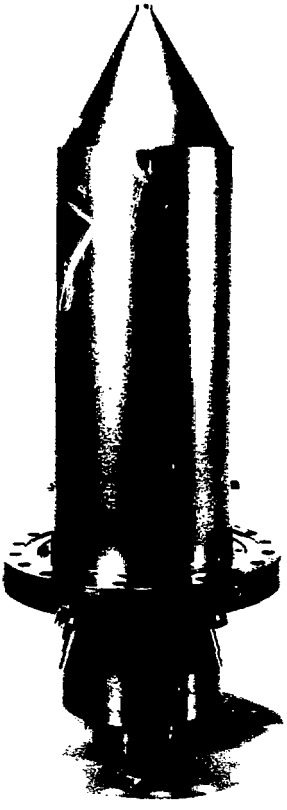

CBB 793-3978

Figure 7. Schematic of the TOF analyzer and associated electronics. A = 1 MΩ, B = 422 kΩ, C = 1 MΩ, D = 619 kΩ, E = 750 kΩ; the voltage divider and power supply were potted in thermally conducting epoxy and were heat sunk to the detector support stalk. MONO = 8° line monochromator. CS = ceramic spacer. MS = mylar spacer. MCP = 40 mm diameter microchannel plate. DC = decoupling capacitor. CA = coaxial anode. DT = decoupling transformer. CFD = constant fraction discriminator. Attn = 0 - 100 db attenuator. DD = differential discriminator. TAC = time-to-amplitude converter. PHA/MCA = combination pulse height analyzer and multichannel analyzer.

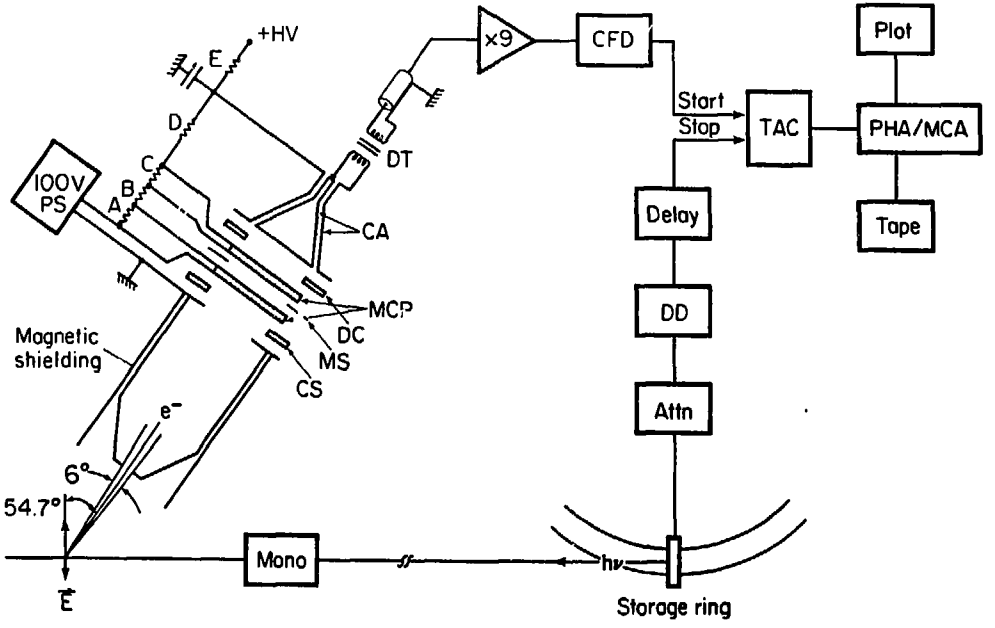
+HV
E
D
C
B
A
100V PS
DT
CA
MCP
DC
MS
CS
Magnetic shielding
e⁻
6°
54.7°
E
Mono
hν
Storage ring
x9
CFD
Start
Stop
TAC
Delay
DD
Attn
Plot
PHA/MCA
Tape

XBL 792-619

Figure 8. High voltage resistor/divider shown before and after potting in thermally conducting epoxy. The cylinder is made of brass and is gold plated.

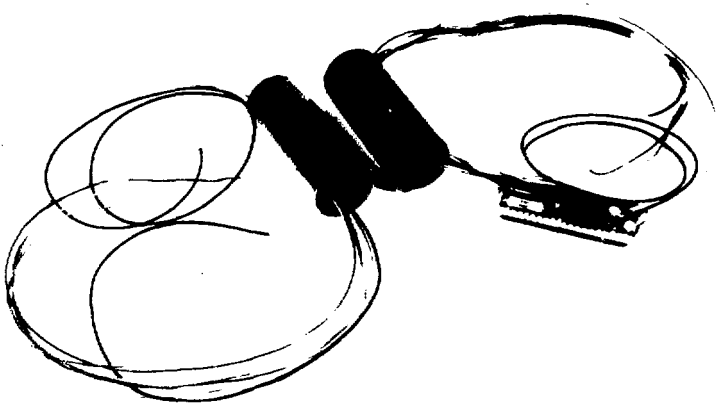

CBB 793-3984

Figure 9. Close-up view of the outer shield of the anode cone and the hand-wound transformer used to decouple the high voltage signal to ground potential. The output signal is collected by a 50 Ω coaxial cable as shown. The anode cone was constructed from brass and gold plated.

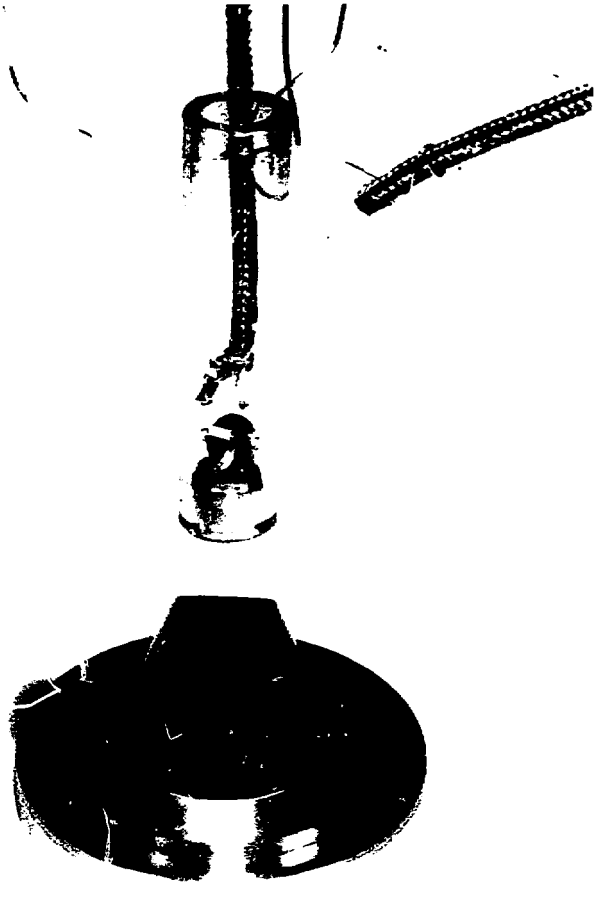

Figure 10. Prompt signal resulting from Rayleigh photon scattering from the gas sample. The shape of the prompt signal and FWHM of 300 psec are characteristic of the synchrotron radiation pulse.

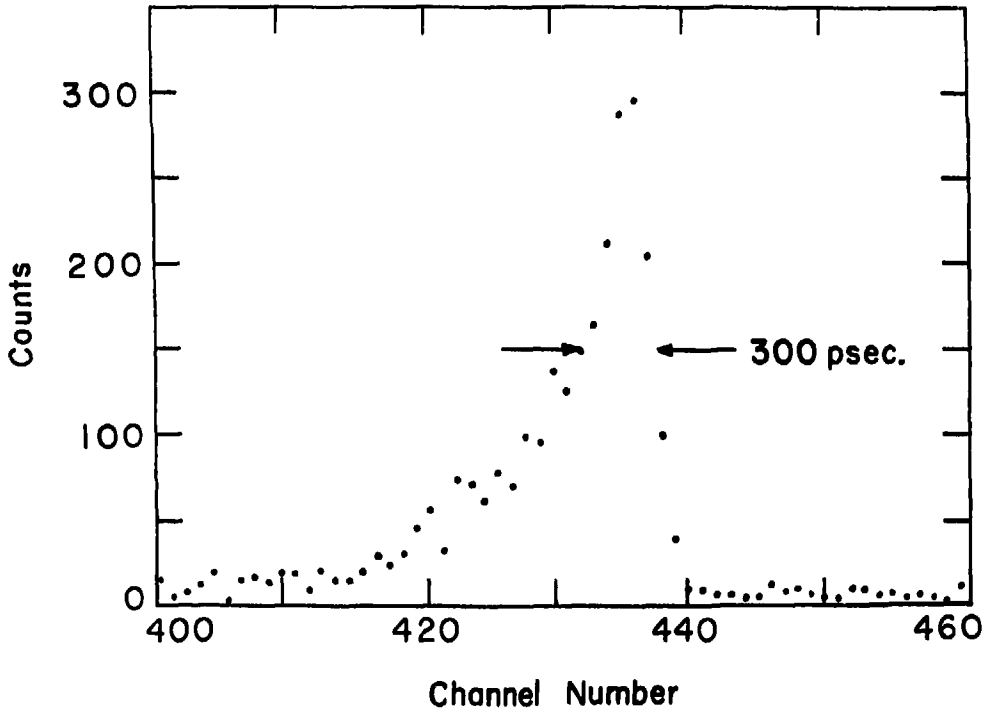

XBL 792-8565

Figure 11. TOF photoelectron spectrum of the 5p shell of atomic Xe taken at 54.7° with respect to the polarization vector of the radiation.

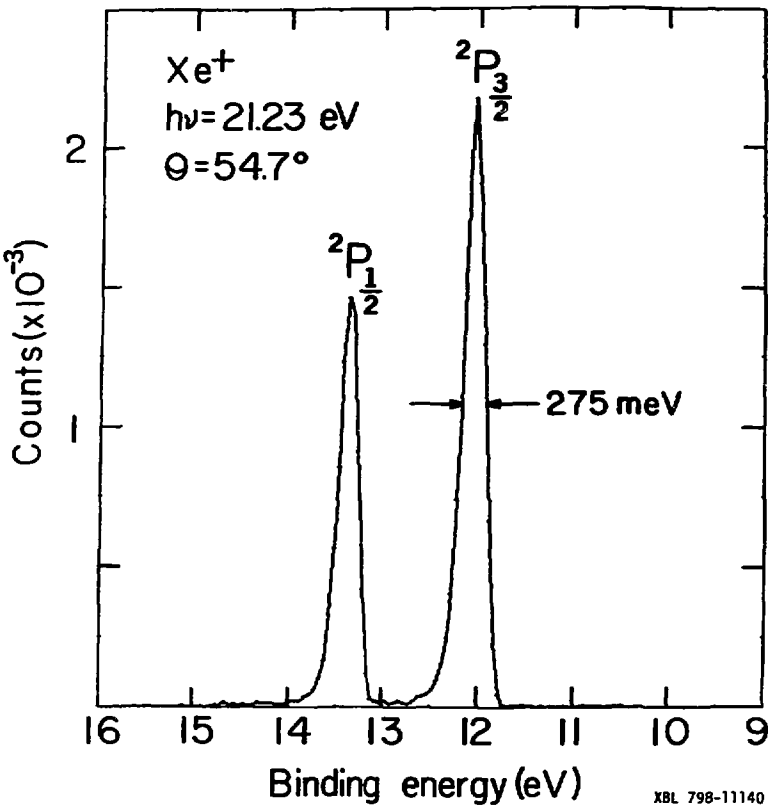
Xe+
hν=21.23 eV
θ=54.7°
²P 3/2
²P 1/2
275 meV
Counts (x10⁻³)
2
1
16
15
14
13
12
11
10
9
Binding energy (eV)
XBL 798-11140

Figure 12. Schematic for the routing electronics to be used for the measurement of photoelectron angular distributions with two TOF analyzers. CFD = constant fraction discriminator. FI = multiple input fan-in. R = router; this component routes the coincidence pulse-height signal resulting from one of the TOF analyzers and the beam signal to the appropriate storage subgroup of the multichannel analyzer. TAC = time-to-amplitude converter. PHA/MCA = combination pulse-height analyzer and multichannel analyzer.

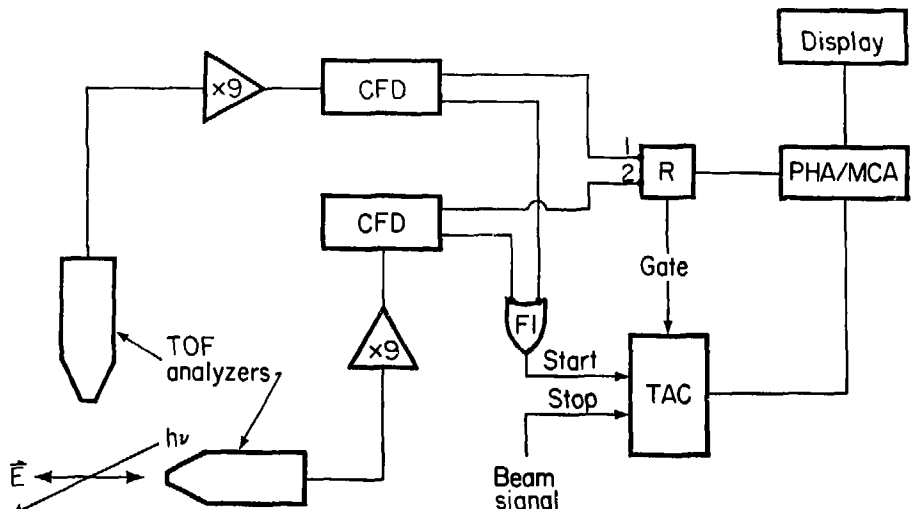
Display
x9
CFD
1
2
R
PHA/MCA
CFD
Gate
FI
x9
TOF
analyzers
Start
Stop
TAC
hν
E
Beam
signal

XBL 792-618

Figure 13. The efficiency function, f(E), versus photoelectron kinetic energy for the SSRL run of May, 1979. The empirical expression is shown as the solid curve and reproduces the data points to within 2%.

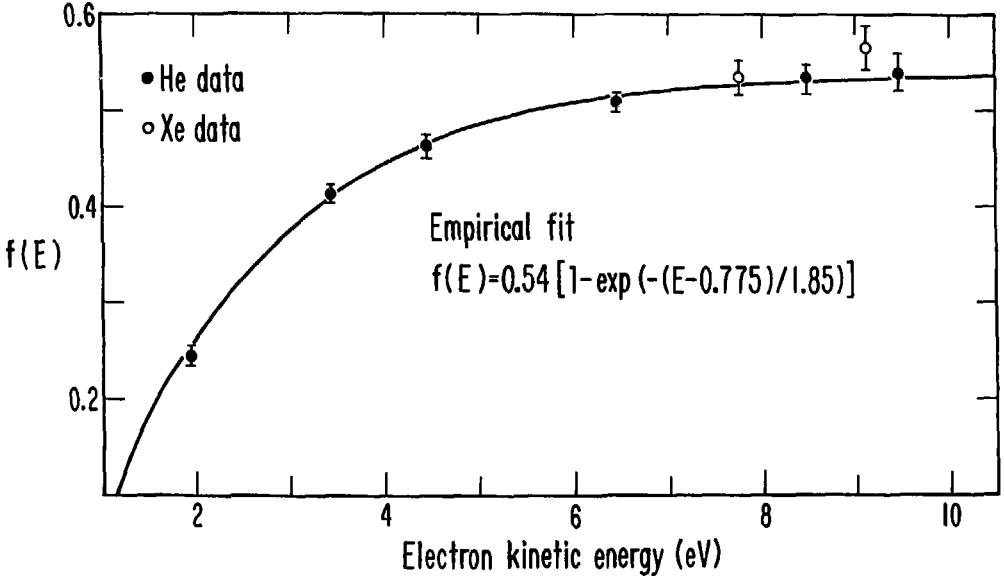
0.6
0.4
0.2
f(E)
• He data
○ Xe data
Empirical fit
f(E)=0.54[1-exp(-(E-0.775)/1.85)]
2
4
6
8
10
Electron kinetic energy (eV)

XBL798-2724

Figure 14. TOF photoelectron spectra of the 5p shell of Xe taken at both 0° and 54.7° with respect to the polarization vector of the radiation. Note the difference signal level and energy resolution between the two spectra.

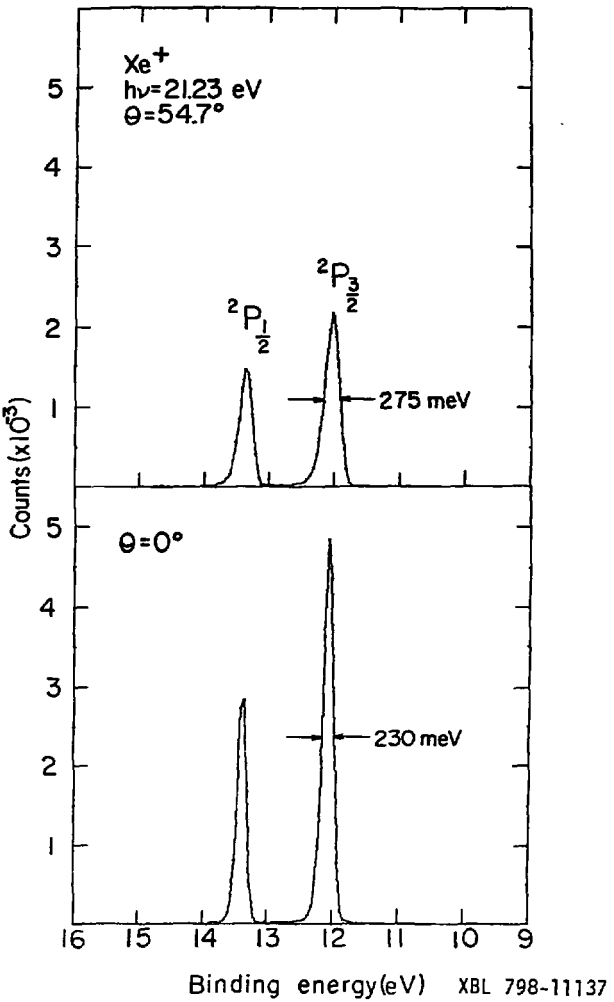
Xe+
hν=21.23 eV
θ=54.7°
²P1/2
²P3/2
275 meV
θ=0°
230 meV
Counts (x10⁻³)
Binding energy(eV)
XBL 798-11137

Figure 15. Photograph of the interaction region of the TOF photoelectron spectrometer. The 54.7° analyzer is furthest to the left, the gas inlet probe enters from the top and the 0° analyzer is pointing perpendicular to the plane of the picture.

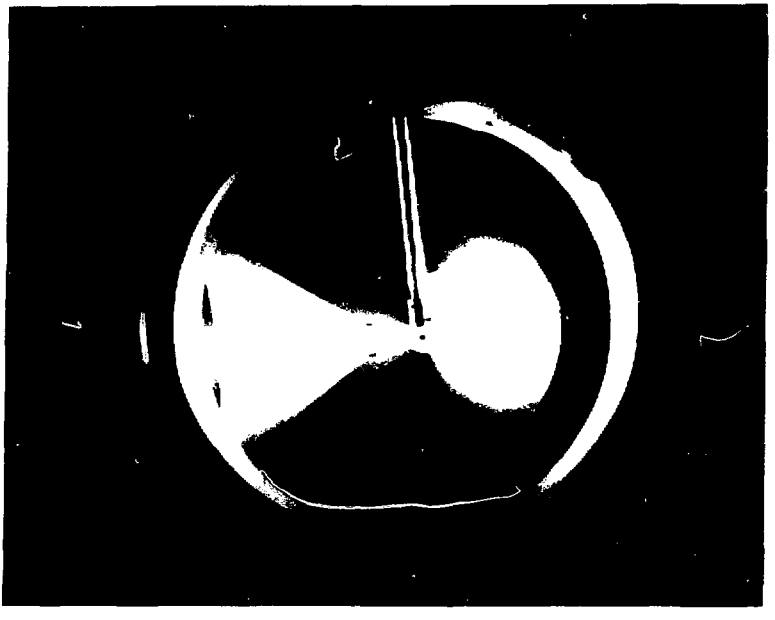

CBB 794-10892

Chapter III

Spin-Orbit Effects in the Xe 5s → εp Photoelectron Angular Distribution*

Abstract

The angular distribution of Xe 5s → εp photoelectrons has been measured at kinetic energies near the Cooper minimum. The angular measurements were made using pulsed synchrotron radiation in conjunction with a highly efficient time-of-flight (TOF) photoelectron spectrometer. The measured asymmetry parameters, β_{5s}, differ markedly from the non-relativistic value of 2, particularly near the Cooper minimum in qualitative agreement with theoretical models based on a purely jj coupling scheme. Comparison to recent fully-relativistic calculations also indicates the relative importance of interchannel coupling in the 5s → εp photoionization process.

---

*Work done in collaboration with S. H. Southworth, R. A. Rosenberg, E. D. Poliakoff, P. Kobrin and D. A. Shirley.

A. Theoretical Description of the ns → εp Photoelectron Angular Distributions of the Rare Gases

As discussed briefly in Chapter I, several theoretical expressions for the asymmetry parameter β have been derived at various levels of approximation and coupling conditions. In describing the ns photoionization reaction it is particularly useful to employ the most general of these theories, that of the angular momentum transfer theory (AMTT) of Fano and Dill.[1] In the AMTT framework, the asymmetry parameter is expressed by an average over asymmetry parameters for the allowed values of j_t, the angular momentum transferred to the target by photoionization. The advantage to this formulation is that the geometrical parameters which depend only on the observed quantities in the photoionization process, i.e., total angular momentum and parity, are separated from the dynamical factors which determine the transition amplitudes. In addition, all dynamical interactions (electrostatic and magnetic) between the ion core and photoelectron are included implicitly. This later property of the AMTT is particularly useful for the description of ns subshell photoionization since spin-orbit interactions (magnetic) and interchannel correlations (electrostatic) have a pronounced effect on the ns → εp angular distribution.

In the AMTT, photoionization of the ns subshells is given by the reaction

$$A(ns^2np^6;\ J_A = 0,\ \pi_A = +1) + \gamma(j_\gamma = 1,\ \pi_\gamma = -1)$$

$$\longrightarrow A^+(nsnp^6;\ J_C = \tfrac{1}{2},\ \pi_C = +1) + e^-(\ell,\ s,\ \pi_e = (-1)^\ell) \qquad (1)$$

where the subscripts A, γ and C refer to the neutral target rare gas atom, the ionizing photon and the residual ionic core, respectively.

By conservation of total angular momentum and parity

$$\vec{J} = \vec{J}_A + \vec{j}_\gamma = \vec{J}_C + \vec{s} + \vec{\ell} \tag{2}$$

$$\pi = \pi_A \pi_\gamma = \pi_C \pi_e = \pi_C (-1)^\ell \tag{3}$$

the orbital angular momentum of the continuum electron is fixed at $\ell=1$ (p wave). This result is simply a restatement of the dipole selection rule $\Delta\ell = \pm 1$ for atomic s shell ionization. It is convenient to describe reaction (1) by the angular momentum transferred to the target by the photoionization process defined by[1]

$$\vec{j}_t = \vec{J}_I - \vec{J}_A = \vec{j}_\gamma - \vec{\ell} \tag{4}$$

where the angular momentum of the residual core, $\vec{J}_C$, and the unobserved photoelectron spin, $\vec{s}$, have been coupled to give $\vec{J}_I (= \vec{S}_C + \vec{s})$. In terms of j_t, the differential cross section is given by[1]

$$\frac{d\sigma}{d\Omega} = \frac{3\pi\lambda^2}{2J_A+1} \sum_{j_t} \sum_{\ell,\ell'} \langle J_I \ell | \bar{S}(j_t) | J_A j_\gamma \rangle$$

$$\times \langle J_A j_\gamma | \bar{S}(j_t)^* | J_I \ell' \rangle \, \Theta(j_t;\, j_\gamma m_\gamma;\, \ell\ell') \tag{5}$$

where λ is the photon wavelength divided by 2π, $\langle \bar{S}(j_t) \rangle$ are the reduced scattering amplitudes and Θ are the geometrical functions which describe the angular distribution for each j_t. The Θ take on a particular simple form for values of j_t where $j_t + \ell + j_\gamma$ is odd. For these angular momentum transfers, the angular distribution is simply a $\sin^2\theta$ distribution with $\beta_{unfav}(j_t) = -1$. These values of j_t are called parity unfavored[2] and for excitation by linearly polarized radiation ($j_\gamma = 1$, $m_\gamma = 0$) parity unfavored transfers occur for $j_t = \ell = \ell'$.

For ns photoionization, Equation (4) becomes

$$\vec{j}_t = \vec{S}_C + \vec{s} \tag{6}$$

for which j_t takes on the parity favored value $j_t = 0$ and the parity unfavored value $j_t = 1$. From the parity favored geometrical function $\Theta(0;\ 10;\ 11,\ \theta)$ we find $\beta_{fav}(j_t = 0) = 2.$[1] The observed asymmetry parameter can then be expressed as the incoherent sum over the parity favored and unfavored $\beta(j_t)$'s weighted by their cross sections, i.e.,

$$\beta_{ns} = \frac{2\sigma(0)-\sigma(1)}{\sigma(0)+\sigma(1)} \tag{7a}$$

$$= 2 - \frac{3\sigma(1)}{\sigma(0)+\sigma(1)} \tag{7b}$$

where for reaction (1) the integrated cross se tions are given by

$$\sigma(j_t) = \pi\lambda^2(2j_t+1)\,|\bar{S}(j_t)|^2. \tag{8}$$

Equation (7) is completely general and has been derived without imposing any angular momentum coupling scheme, e.g., LS or jj coupling. The numerical value of β_{ns} ultimately depends on the detailed evaluation of the scattering amplitudes in Equation (8), however, several limiting cases can be considered. If strict LS coupling is adopted, $\vec{S}_C$ and $\vec{s}$ are required to remain coupled to a singlet, i.e., $\vec{S}_C + \vec{s} = 0$. In this case j_t is restricted to the parity favored value ($j_t = 0$) and one obtains the LS coupling result ($\beta_{ns} = 2$) of Cooper and Zare[3] for single channel $ns \rightarrow \varepsilon p$ ionization. The He $1s \rightarrow \varepsilon p$ angular distribution is accurately described in this limit,[4] however, a measurement of the Xe $5s \rightarrow \varepsilon p$ angular distribution at $h\nu = 40.8$ eV resulted in $\beta_{5s} = 1.4 \pm .1$.[5] This deviation from the LS result is attributed to spin-orbit interactions

between the core and photoelectron. This interaction leads to two dipole allowed channels $ns_{1/2} \rightarrow \epsilon p_{1/2}$ and $ns_{1/2} \rightarrow \epsilon p_{3/2}$ which can interfere resulting in $\beta_{ns} < 2$.[6] Spin-orbit effects in the AMTT are described by parity unfavored angular momentum transfers resulting from anisotropic interactions (magnetic) between the core and photoelectron. In the case of ns photoionization we see from Equation (6) that the parity unfavored transition ($j_t = 1$) results in a "flip" of the photoelectron spin, $\vec{s}$. Equation (7b) shows that photoejection with $j_t = 1$ will cause $\beta_{ns} < 2$, to an extent dependent on the relative strength of the unfavored process.

The scattering amplitudes appearing in Equations (7) and (8) are in general very complex and can include interactions with all the possible continuum channels.[5,7] In this respect the evaluation of the scattering matrix elements is very similar to the many-body treatments employing the random-phase approximation (RPA) in which the interchannel interactions are treated in a perturbation expansion of the dipole amplitudes.[8] These interactions consist of introducing electrostatic ($1/r_{12}$) interactions between the various continuum final states of J=1 and odd parity ($\pi_c\pi_e = -1$). For the ns photoionization of the heavier rare gases (Ar, Kr, Xe) these continua include those allowed final states resulting from the $(n-1)d^9\,\epsilon p$ or ϵf, $np^5\epsilon s$ or ϵd and $ns\epsilon p$ configurations. Interchannel couplings alone, however, do not lead to $\beta_{ns} < 2$ since this result is purely a relativistic effect. For this reason it is useful to consider the evaluation of the scattering amplitudes in the absence of interchannel couplings. In this limit Dehmer and Dill[5] have shown

$$\bar{S}(0) = 3^{-1/2}(D_{1/2} + \sqrt{2}\, D_{3/2})\, \exp[i(\sigma+\pi/2)] \tag{9a}$$

$$\bar{S}(1) = 3^{-1}(\sqrt{2}\, D_{1/2} - D_{3/2})\, \exp[i(\sigma+\pi/2)] \tag{9b}$$

where $D_j \equiv D_j \exp(i\delta_j)$ are the dipole amplitudes for dissociation channel $|\varepsilon p_j\rangle$ (see Appendix A) with electron-core short range phase shift δ_j and coulomb phase shift σ.[7] Substitution into Equations (8) and (7) results in

$$\beta_{ns} = 2 - \frac{(\sqrt{2}D_{1/2}-D_{3/2})^2}{D_{1/2}^{\ 2}+D_{3/2}^{\ 2}} . \tag{10}$$

This expression is identical to that derived in strict jj coupling by Walker and Waber[6] (as expected from the neglect of electrostatic interactions discussed above) and shows the explicit dependence of β_{ns} on the two interferring dipole allowed continuum channels. Even for Xe the spin-orbit interaction is expected to be weak for most photoelectron kinetic energies so that $D_{3/2} \sim \sqrt{2}\, D_{1/2}$, $\delta_{1/2} \sim \delta_{3/2}$ and $\beta_{ns} \sim 2$.[6,9-11] Relativistic effects, however, can have a dramatic effect on β_{ns} in the neighborhood of the Cooper minimum where the ns integrated cross section for the heavier rare gases (Ar, Kr, Xe) is near zero.[6,9-11] Because of differences in the radial wavefunctions of the $j = \ell \pm 1/2$ continuum states, the $ns_{1/2} \rightarrow \varepsilon p_{1/2}$ and $ns_{1/2} \rightarrow \varepsilon p_{3/2}$ amplitudes vanish at slightly different energies.[12] From Equation (10) we see that $\beta_{ns} \rightarrow 1$ as $D_{1/2} \rightarrow 0$ and $\beta_{ns} \rightarrow 0$ as $D_{3/2} \rightarrow 0$ so that β_{ns} is expected to decrease rapidly as the Cooper minimum is approached from low energy.

An alternative form of Equation (10) can be made by the recoupling transformation jj → LS (see Appendix B) from which the cross sections (j_t) can be written

$$\sigma(0) = \pi\lambda^2 \ |D_S|^2 \tag{11a}$$

$$\sigma(1) = \pi\lambda^2 \ |D_T|^2 \tag{11b}$$

where D_S and D_T are the dipole amplitudes to $|^1P_1\rangle$ and $|^3P_1\rangle$ final states, respectively. The asymmetry parameter then becomes

$$\beta_{ns} = 2 - \frac{3|D_T|^2}{|D_S|^2+|D_T|^2} . \tag{12}$$

This recoupling more clearly shows that in the jj coupling limit (no interchannel coupling), the parity favored ($j_t = 0$) transition corresponds to the allowed LS coupling transition $^1S_0 \rightarrow {}^1P_1$ while the parity unfavored ($j_t = \ell = 1$) reaction involves a spin reorientation, $^1S_0 \rightarrow {}^3P_1$. With the introduction of *intra*channel coupling (analogous to intermediate coupling for bound states) the $^3P_1$ and $^1P_1$ are mixed and the relationship between parity favoredness and spin orientation becomes less meaningful.

Equations (3) and (5) have been the basis of several theoretical calculations on the β_{ns} for the rare gases and particularly for Xe. These include Dirac-Slater (DS)[6] and Dirac-Fock (DF)[11] relativistic single-particle calculations and relativistic many-body calculations employing the random-phase-approximation (RPA).[9,10] Aside from He, however, only one[5] experimental measurement of β_{ns} for the rare gases has been performed. The difficulty arises from the extremely low cross sections of the ns subshells (≤.5 Mb). In particular, the most interesting effects are expected near their Cooper minima where the cross sections are ~.1 Mb at best. Hence, very long collection times and/or extremely efficient electron analyzers are necessary. In this work we report measurements of the Xe 5s → εp angular distribution at three kinetic energies near the Cooper minimum. The β_{ns} measurements were made using pulsed synchrotron radiation in conjunction with a highly efficient time-of-flight photoelectron spectrometer. The experimental

details are discussed in Section B and the measured β_{5s} values compared with theory in Section C.

B. Experimental

The experiments were performed on the 8° beam line at the Stanford Synchrotron Radiation Laboratory (SSRL). A complete description of the apparatus has been given in Chapter II. Briefly, highly plane-polarized (>97%) synchrotron radiation intersected a gas beam formed by effusive expansion through a microchannel array. Sample densities were estimated to be $\sim 2 \times 10^{-3}$ Torr in the interaction volume and the background pressure in the sample chamber and detectors was $\leq 5 \times 10^{-5}$ Torr. These operating conditions were chosen to keep signal loss due to electron-atom scattering to a negligible level. Ejected photoelectrons were detected by two TOF analyzers placed at 0° and 54.7° with respect to the photon polarization vector. The TOF analyzers utilized the unique time structure of the storage ring at SSRL (300 psec pulse duration (FWHM), 780 nsec repetition period) and are orders of magnitude more efficient than the more conventional single channel deflection-type analyzers. Employing the input routing electronics described in Chapter II, the output of the two detectors was simultaneously analyzed with a single time-to-amplitude converter and stored separately in a multichannel analyzer. The β_{5s} values were corrected for the relative counting efficiencies of the two TOF detectors by calibrating the apparatus with He for which $\beta = 2$ for the energies used in this work. Additional corrections for the finite solid angles of the detectors ($\sim 8 \times 10^{-3}$ sr) and the slight amount of unpolarized radiation ($\lesssim 3\%$) were found to be small (<1%) relative to the statistical error in the peak areas.

Measurements were made at photon energies of 26.8 eV, 30.0 eV and 32.0 eV. Due to the combination of low photon flux on the 8° line above 25 eV and the low 5s cross section (~.1 Mb) it was necessary to open the monochromator slits to an 8.7 Å (FWHM) band pass. The point at $h\nu$ = 30.0 eV was repeated on a separate run and the β_{5s} values agreed to within 1% ($\Delta\beta/\beta$) indicating the level of reproducibility of our measurements.

It should be emphasized at this time that these experiments would have been virtually impossible to do without the use of TOF photoelectron energy analysis. The most important aspects of TOF analysis for very low signal experiments such as the β_{5s} measurements are (1) the entire spectrum is collected simultaneously and (2) random background contributions are distributed uniformly over the entire time spectrum. These properties permitted accumulation times for the 5s peaks to be 2-4 hrs with resulting signal-to-background ratios of between .5 to 1.0. In contrast, a single-channel deflection-type analyzer, e.g., 180° hemispherical electrostatic analyzer, would have required at least 10 times the accumulation time and still resulted in signal-to-background ratios smaller than that obtained by TOF analysis. Under these circumstances it would have been nearly impossible to make the β_{5s} measurements with statistical uncertainties of less than 100% within the allotted time.

C. Results and Discussion

The measured asymmetry parameters are given in Table 1. Very low 5s signals recorded in spectra taken at $h\nu$ = 34.0 eV do not allow a precise value for β_{5s} to be reported, however, our analysis indicates that $_{ns}$ is non-negative at this energy. The conservative error estimates in Table 1 reflect the very low cross section of the 5s line near its Cooper minimum.

From Table 1 we note that the β_{5s} decreases as the Cooper minimum ($h\nu \sim 35.4$ eV) is approached and increases again after the minimum is passed. This is in qualitative agreement with our earlier discussion concerning the jj coupling limit (Eqn. (10)) in which $\beta_{5s} \to 1$ as the $5s_{1/2} \to \epsilon p_{1/2}$ amplitude approaches zero. At this energy ($h\nu \sim 30$ eV, from our data) photoionization proceeds via the $5s_{1/2} \to \epsilon p_{3/2}$ channel only. The introduction of interchannel couplings can modify the actual value of β_{5s} away from these limiting cases, however, the qualitative trends predicted by the jj limit are evidently still followed.

In Table 1 we have also given the strength parameters, s, defined by Dill[7] as

$$s = \frac{\sigma(0)-\sigma(1)}{\sigma(0)+\sigma(1)} \tag{13}$$

which measures the relative "strength" of the parity favored photoionization channels. The values of the strength parameters follow the same trend as the β_{5s} versus energy, approaching the pure parity favored limit (LS coupling limit) $s = 1$ at low energy and steadily decreasing as the parity unfavored contribution increases closer to the Cooper minimum. Based on the measurement of Dehmer and Dill[5] at $h\nu = 40.8$ eV, the strength parameter increases again beyond the Cooper minimum and can be expected to approach the parity favored limit at even higher energies.[14]

In Figure 1 we compare the measured asymmetry parameters with the results of the various theoretical calculations. One notes that the only point[5] previously measured is in approximate agreement with nearly all the calculations with the exception of the K-matrix results.[15] The additional data of this work clearly shows that only the many-body RPA calculations which have included the full 5s, 5p and 4d interchannel

correlations are in good agreement with all the experimental points. Due to the neglect or incomplete treatment of interchannel couplings the fully relativistic DS and DF calculations predict the Cooper minimum to lie too low (in the discrete spectrum) and the relativistic RRPA(5s + 5p) places the minimum too high in energy. Hence, although these calculations correctly predict a resonance in β due to spin-orbit effects in the continuum, they do not reproduce the actual energy position of the resonance.

The high energy cut-off, approximately 34 eV, of the 8° line monochromator prevented measurements of β_{5s} at and beyond the Cooper minimum. Accurate measurements of β at the Cooper minimum are highly desirable for determining the importance of performing the fully relativistic RRPA(5s, 5p, 4d) calculation[10] in comparison to the non-relativistic RPAE(5s, 5p, 4d) model in which spin-orbit effects were included semi-empirically.[9] Comparison of the RRPA(5s, 5p) and RRPA(5s, 5p, 4d) curves in Figure 1 shows that the predicted minimum value of β_{5s} depends strongly on the extent of inclusion of interchannel interactions. Measurement of the limiting value of β_{5s} would provide a very sensitive test to the quality of these calculations.

At this point it is interesting to compare the kind of information derived from an angular distribution measurement with that obtained from related experiments in which the photoelectron spin polarization is measured. Specifically, if circularly polarized radiation ($j_\gamma = 1$, $m_\gamma = +1$) is used in the photoionization of the ns subshells of the rare gases, the differential cross section for producing photoelectrons with propagation vector $\vec{k}_e$ and spin polarization $\vec{s}$ is given by[16]

$$\frac{d\sigma}{d\Omega}(\vec{k}_e, \vec{s}) = \frac{\sigma_{ns}}{8\pi}\left\{1 - \frac{\beta_{ns}}{2} P_2(\vec{k}_\gamma \cdot \vec{k}_e) + \alpha(\vec{k}_\gamma \cdot \vec{s}) - \gamma\left[\frac{3}{2}(\vec{k}_\gamma \cdot \vec{k}_e)(\vec{s} \cdot \vec{k}_e) - \frac{1}{2}(\vec{k}_\gamma \cdot \vec{s})\right]\right\} \tag{14}$$

where σ_{ns} and β_{ns} have previously been defined and k_γ is the photon propagation direction.[17] In a jj coupling scheme, the α and γ coefficients are

$$\alpha = \frac{\frac{3}{2} D_{3/2}^{\ 2} - \frac{1}{3}\left|\sqrt{2}\, D_{3/2} + D_{1/2}\right|^2}{D_{3/2}^{\ 2} + D_{1/2}^{\ 2}} \tag{15a}$$

$$2\gamma = \frac{\frac{1}{3}\left|\sqrt{2}\, D_{3/2} + D_{1/2}\right|^2 - 3D_{1/2}^{\ 2}}{D_{3/2}^{\ 2} + D_{1/2}^{\ 2}} . \tag{15b}$$

We note that the first two terms of Equation (14), are just those which define the angular distribution for circularly polarized light irrespective of the photoelectron spin.[18] Experimental measurements of spin polarization are usually done for $\vec{s} \| \vec{k}_\gamma$ and for angle integrated photoelectron collection.[19] Under these conditions, the degree of spin polarization for ns photoionization is given by

$$\langle P_\| \rangle_{\vec{k}_e} = \alpha \tag{16}$$

where α has been defined in Equation (15a).[20] This expression was first derived by Fano[21] in relation to photoionization of the outer ns electron of the alkali metal atoms. We note that the existence of a net spin polarization is simply a result of spin orbit effects in the continuum since in the non-relativistic limit $D_{3/2} = \sqrt{2}\, D_{1/2}$ and $\delta_{3/2} = \delta_{1/2}$

resulting in $\alpha = 0$. Hence, spin polarization measurements on the ns subshells can be used to derive the identical information, i.e., the relative magnitudes of $D_{3/2}$ and $D_{1/2}$, that β_{ns} experiments afford. In perfect analogy with the β_{ns} measurements we note that α will show its largest deviations from the non-relativistic limit ($\alpha = 0$) where one or both of the continuum channel amplitudes are varying rapidly. In particular, near the Cooper minimum where $D_{1/2} \rightarrow 0$ and $D_{3/2} \neq 0$, the net spin polarization can be as high as 80%. In general, however, spin polarization measurements are several orders of magnitude more difficult experimentally than the corresponding β measurements. These difficulties arise from two main sources: (1) methods for circularly polarizing VUV radiation are very inefficient at lower energies ($\leq$10 eV) and virtually non-existent for higher energies; (2) detection of spin polarization involves high energy Mott scattering which has a conversion efficiency (incident current/scattered current) of at best $\sim 10^{-3}$.[19] For these reasons, angular distribution measurements represent one of the few techniques available for the detailed investigation of relativistic effects in the continuum.

References Chapter III

1. U. Fano and D. Dill, Phys. Rev., A6, 185 (1972); D. Dill and U. Fano, Phys. Rev. Lett., 29, 1203 (1972).

2. U. Fano, Phys. Rev., 135, B863 (1964).

3. J. Cooper and R. N. Zare, J. Chem. Phys., 48, 942 (1968); Lectures in Theoretical Physics, edited by S. Geltman, K. T. Mahanthappa and W. E. Brittin (Gordon and Breach, New York, 1969), Vol. XI-C, pp. 317-37.

4. W. S. Watson and D. T. Stewart, J. Phys., B7, L466 (1974); J. L. Dehmer, W. A. Chupka, J. Berkowitz and W. T. Jivery, Phys. Rev., A12, 1966 (1975).

5. J. L. Dehmer and D. Dill, Phys. Rev. Lett., 37, 1049 (1973).

6. T. E. H. Walker and J. T. Waber, J. Phys., B6, 1165 (1973); J. Phys., B7, 674 (1974).

7. D. Dill, Phys. Rev., A7, 1976 (1973).

8. M. Ya. Amusia, V. K. Ivanov, N. A. Cherepkov and L. V. Chernysheva, Sov. Phys.-JEPT, 39, 752 (1974); M. Ya. Amusia and N. A. Cherepkov, Case Studies in Atomic Physics, 5, 47 (1975); M. Ya. Amusia, Comments Atom Mol. Phys., 8, 61 (1979).

9. N. A. Cherepkov, Phys. Lett., A66, 204 (1978).

10. W. R. Johnson and K. T. Cheng, Phys. Rev. Lett., 40, 1167 (1978); Phys. Rev. A, to be published.

11. W. Ong and S. T. Manson, J. Phys., B11, L65 (1978).

12. For the $j = \ell - \frac{1}{2}$ ($\varepsilon p_{1/2}$) continuum function the spin-orbit interaction is attractive and as a consequence the $j = \ell - \frac{1}{2}$ component is drawn closer to the nucleus. Hence, the matrix element $\langle ns_{1/2}|D|\varepsilon p_{1/2}\rangle$ will pass through zero at a lower kinetic energy than the corresponding matrix element for the $\varepsilon p_{3/2}$ channel.

13. Equation (11) can also be derived by substituting the recoupling transformation directly into Equation (3) as was done in Reference (10).

14. Torop, et al., have reported $1.8 \le \beta_{5s} \le 2$ for a single measurement at $h\nu = 83$ eV, well above the Cooper minimum. The resulting strength parameter for this measurement lies between .9 and the parity favored limit $s = 1.0$. See L. Torop, J. Morton and J. B. West, J. Phys., B9, 2035 (1976).

15. K. N. Huang and A. F. Starace, private communication to Reference (10).

16. N. A. Cherepkov, Sov. Phys.-JETP, 38, 463 (1974).

17. Similar expressions for initial states with $\ell > 0$ have also been derived for circularly, linearly and unpolarized radiation (see N. A. Cherepkov, Phys. Lett., A40, 119 (1972); J. Phys., B11, L435 (1978) and Reference (16)).

18. V. Schmidt, Phys. Lett., A45, 63 (1973).

19. See for example, U. Heinzmann, J. Phys., B11, 399 (1978).

20. The choice of circularly polarized radiation is necessary since the angle averaged net spin polarization given by Equation (16) is zero for linearly polarized and unpolarized radiation (see J. Kessler, Polarized Electrons (Springer-Verlag, Berlin, 1976), Chapter 5.)

21. U. Fano, Phys. Rev., 178, 131 (1969); Phys. Rev., 184, 250 (1969).

Table I. Experimental β_{5s} Values and Strength Paramet ~ ($s = [\sigma(0)-\sigma(1)]/[\sigma(0)+\sigma(1)]$)

$h\nu$(eV)	β_{ns}	s
26.8	1.9 ± .2	.93
30.0	1.6 ± .2	.73
32.0	1.1 ± .3	.40
40.8	1.4 ± .1[a]	.60

[a]Reference (5).

Figure 1. Comparison of theoretical and experimental asymmetry parameters for Xe 5s → εp photoionization versus energy. Experiment: ⊕ this work; ⊕ Dehmer and Dill, Reference 5. Theory: — ·· — Walker and Waber, Reference 6; -- x — Ong and Manson, Reference 11; — · — Cherepkov, Reference 9; ——— Johnson and Cheng, Reference 10; - - - Huang and Starace, Reference 14.

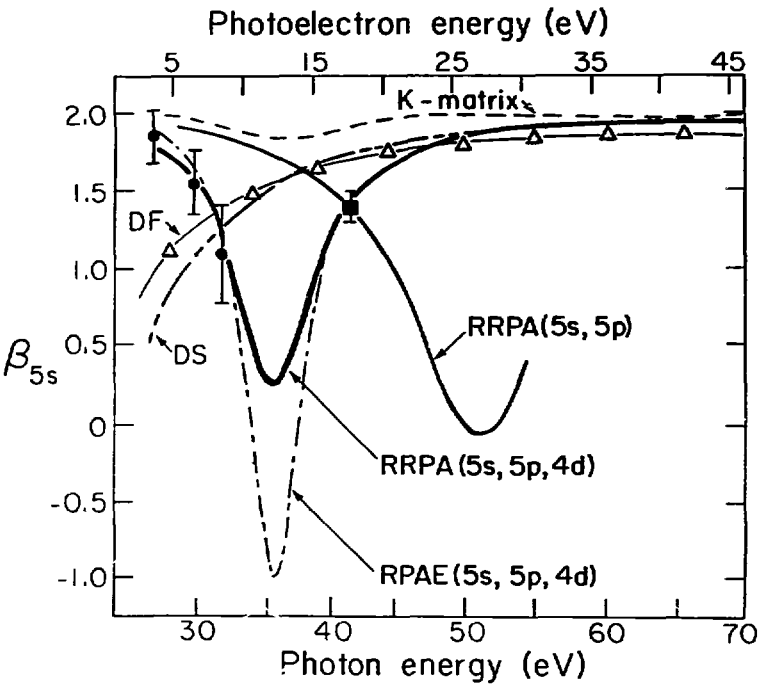
Photoelectron energy (eV)
5
15
25
35
45
K-matrix
2.0
1.5
1.0
0.5
0
-0.5
-1.0
DF
DS
β_{5s}
RRPA(5s, 5p)
RRPA (5s, 5p, 4d)
RPAE (5s, 5p, 4d)
30
40
50
60
70
Photon energy (eV)

XBL 798-2500

Appendix A

Dipole Matrix Elements in jj Coupling

In this appendix we wish to establish the relationship between the dipole amplitudes D_α and the radial dipole matrix elements R_α from which photoionization transition strengths are usually calculated. The formalism will be applied to ns subshell photoionization, although the treatment outlined here is completely general.

We consider the photoionization transition from an initial state $|i\rangle = |ns_{1/2}\ ns_{1/2};\ J_i = 0,\ M_i = 0\rangle$ to the dipole allowed final states $|f_j\rangle = |ns_{1/2}\ \varepsilon p_j;\ J_f = 1,\ M_f\rangle$ ($j = 1/2,\ 3/2$) produced by absorption of a linearly polarized photon. The transition strength to final state $|f_j\rangle$ is proportional to the matrix element

$$\langle f_j|\sum_i z_i|i\rangle = \langle f_j|D_0^{(1)}|i\rangle \tag{A1}$$

where the polarization vector of the radiation lies along the z axis. $D_0^{(1)}$ is the dipole operator for linearly polarized light given by

$$D_q^{(k)} = \sum_i r_i C_q^{(k)}(\theta_i,\phi_i). \tag{A2}$$

The r_i represent the coordinates of the ith electron and the $C_q^{(k)}$ are related to the spherical harmonics by

$$C_q^{(k)} = \left(\frac{4\pi}{2k+1}\right)^{\frac{1}{2}} Y_{kq}(\theta,\phi) \tag{A3}$$

By the Wigner-Eckart theorem, Equation (A1) becomes

$$\langle f_j|D_0^{(1)}|i\rangle = (-1)^{J_f-M_f}\begin{pmatrix} J_f & 1 & J_i \\ M_f & 0 & M_i \end{pmatrix} D_j \tag{A4}$$

where the quantity in brackets is a 3-j coupling coefficient and where we have defined the dipole amplitude D_j as the reduced dipole matrix element, i.e.,

$$D_j = (ns_{1/2}\ \varepsilon p_j;\ J_f = 1 \| D^{(1)} \| ns_{1/2}\ ns_{1/2};\ J_i = 0). \tag{A5}$$

The 3-j symbol is non-zero only for $M_f = M_i$ (=0) so that

$$\langle f_j | D_0^{(1)} | i \rangle = \frac{1}{\sqrt{3}} D_j. \tag{A6}$$

The relationship between the dipole amplitudes D_j and the radial dipole matrix elements can now be found through the following expression[1]

$$(j_1 j_2';\ J' \| T^{(k)} \| j_1 j_2;\ J) = (-1)^{j_1+j_2+J'+k} [(2J+1)(2J'+1)]^{\frac{1}{2}} \times \begin{Bmatrix} j_2' & J' & j_1 \\ J & j_2 & k \end{Bmatrix} \times (j_2' \| T^{(k)} \| j_2) \tag{A7}$$

where {} represents a 6-j symbol. This expression is appropriate for evaluating reduced matrix elements in a coupled scheme where the operator $T^{(k)}$ acts only on the indices 2. In our example, $j_1 = j_2 \equiv ns_{1/2}$ and $j_2' \equiv \varepsilon p_j$ and the dipole operator affects the one-electron transitions between $ns_{1/2}(j_2)$ and $\varepsilon p_j(j_2')$. Through the use of Equation (A7), the dipole amplitudes become

$$D_{1/2} = \frac{\sqrt{2}}{2} (\varepsilon p_{1/2} \| D^{(1)} \| ns_{1/2}) \tag{A8a}$$

$$D_{3/2} = \frac{\sqrt{2}}{2} (\varepsilon p_{3/2} \| D^{(1)} \| ns_{1/2}) \tag{A8b}$$

As the final step, the reduced dipole matrix elements are separated into their radial and angular parts, i.e.,

$$(\varepsilon p_j \| D^{(1)} \| ns_{1/2}) = (\varepsilon p_j \| r \| ns_{1/2})(\varepsilon p_j \| C^{(1)} \| ns_{1/2}). \qquad \text{(A9)}$$

The reduced matrix elements of the spherical harmonics in jj coupling, $(1/2\ \ell' j' \| C^{(k)} \| 1/2 \ell j)$, are easily evaluated[2] from which we obtain the desired relationships

$$D_{1/2} = \frac{1}{\sqrt{3}} (\varepsilon p_{1/2} \| r \| ns_{1/2}) = \frac{1}{\sqrt{3}} R_{1/2} \qquad \text{(A10)}$$

$$D_{3/2} = \sqrt{\frac{2}{3}} (p_{3/2} \| r \| ns_{1/2}) = \sqrt{\frac{2}{3}} R_{3/2}. \qquad \text{(A10b)}$$

In the non-relativistic limit $R_{3/2} = R_{1/2}$ which implies $D_{3/2} = \sqrt{2}\, D_{1/2}$ in the same limit. The numerical evaluation of radial dipole matrix elements in jj coupling involving continuum states has been described in detail in a series of papers by Walker and Waber.[3]

References Appendix A

1. A. R. Edmonds, Angular Momentum in Quantum Mechanics (Princeton University Press, Princeton, NJ, 1960), p. 111.

2. G. Racah, Phys. Rev., 62, 438 (1942).

3. T. E. Walker and J. T. Waber, Phys. Rev. Lett., 30, 307 (1973); J. Phys., B6, 1165 (1973); 7, 674 (1974).

Appendix B

Determination of LS-jj Coupling Transformation for $Xe(5s\epsilon p)_{J=1}$ Final States

A two-electron LS eigenstate formed by the coupling of ℓ_1, ℓ_2 (orbital) and s_1, s_2 (spin) angular momenta can be expanded over its corresponding jj coupled eigenstates by the expression[1]

$$|(\ell_1\ell_2)\ L,(s_1s_2)\ S,\ J\rangle$$

$$= \sum_{j_1j_2} ((\ell_1\ell_2)\ L,(s_1s_2)\ S,\ J|(\ell_1s_1)\ j_1,(\ell_2s_2)\ j_2,J)$$

$$\times\ |(\ell_1s_1)j_1,(\ell_2s_2)\ j_2,\ J\rangle. \tag{B1}$$

The LS-jj recoupling coefficients in Equation (B1) are given by

$$((\ell_1\ell_2)\ L,(s_1s_2)\ S,\ J|(\ell_1s_1)\ j_1,(\ell_2s_2)\ j_2,\ J)$$

$$= [(2L+1)(2S+1)(2j_1+1)(2j_2+1)]^{\frac{1}{2}} \begin{Bmatrix} \ell_1 & \ell_2 & L \\ s_1 & s_2 & S \\ j_1 & j_2 & J \end{Bmatrix} \tag{B2}$$

where the quantity {} is a 9-j symbol. For ns photoionization, the two possible LS final states are $|ns\epsilon p,\ ^1P,\ J=1\rangle$ and $|ns\epsilon p,\ ^3P,\ J=1\rangle$ and the two jj coupled final states are $|ns_{1/2}\ \epsilon p_{1/2},\ J=1\rangle$ and $|ns_{1/2}\ \epsilon p_{3/2},\ J=1\rangle$. For these two LS eigenstates Equation (B1) can be used to obtain

$$|ns\varepsilon p,\ ^1P,\ J{=}1\rangle = 2\sqrt{3}\left[\begin{Bmatrix} 0 & 1 & 1 \\ 1/2 & 1/2 & 0 \\ 1/2 & 1/2 & 1 \end{Bmatrix} |ns_{1/2}\ \varepsilon p_{1/2},\ J{=}1\rangle\right.$$

$$\left. + \sqrt{2}\begin{Bmatrix} 0 & 1 & 1 \\ 1/2 & 1/2 & 0 \\ 1/2 & 3/2 & 1 \end{Bmatrix} |ns_{1/2}\ \varepsilon p_{3/2},\ J{=}1\rangle\right] \tag{B3a}$$

and

$$|ns\varepsilon p,\ ^3P,\ J{=}1\rangle = 6\left[\begin{Bmatrix} 0 & 1 & 1 \\ 1/2 & 1/2 & 1 \\ 1/2 & 1/2 & 1 \end{Bmatrix} |ns_{1/2}\ \varepsilon p_{1/2},\ J{=}1\rangle\right.$$

$$\left. + \sqrt{2}\begin{Bmatrix} 0 & 1 & 1 \\ 1/2 & 1/2 & 1 \\ 1/2 & 3/2 & 1 \end{Bmatrix} |ns_{1/2}\ \varepsilon p_{3/2},\ J{=}1\rangle\right]. \tag{B3b}$$

The 9-j symbols in the expansion of the singlet state take on a particularly simple form[2]

$$\begin{Bmatrix} \ell_1 & \ell_2 & L \\ 1/2 & 1/2 & 0 \\ j_1 & j_2 & J \end{Bmatrix} = \frac{(-1)^{\ell_1+j_2+J+1/2}}{[2(2L+1)]^{1/2}} \begin{Bmatrix} J & j_1 & j_2 \\ 1/2 & \ell_2 & \ell_1 \end{Bmatrix} \tag{B4}$$

where the quantity on the r.h.s. of the equation is a 6-j symbol. The 6-j symbols are readily found[3] and the singlet final state is given by

$$|ns\varepsilon p,\ ^1P,\ J{=}1\rangle = \frac{1}{\sqrt{3}}\left(|ns_{1/2}\ \varepsilon p_{1/2},\ J{=}1\rangle + \sqrt{2}\ |ns_{1/2}\ \varepsilon p_{3/2},\ J{=}1\rangle\right). \tag{B5}$$

For the triplet final state, the 9-j symbols can be evaluated using the more cumbersome expression[2]

$$\begin{Bmatrix} \ell_1 & \ell_2 & L \\ 1/2 & 1/2 & 1 \\ j_1 & j_2 & J \end{Bmatrix} = \left[\frac{(-1)^{2\lambda}}{3} \begin{Bmatrix} j_1 & j_2 & J \\ 1/2 & \lambda & \ell_2 \end{Bmatrix} \begin{Bmatrix} \ell_2 & \ell_1 & L \\ 1/2 & \lambda & j_1 \end{Bmatrix} \right.$$

$$\left. + \frac{(-1)^{\ell_1+j_2-\lambda+1}}{6(2J+1)} \begin{Bmatrix} J & \ell_2 & \ell_1 \\ 1/2 & j_1 & j_2 \end{Bmatrix} \delta(LJ) \right]$$

$$\times \begin{Bmatrix} J & L & 1 \\ 1/2 & 1/2 & \lambda \end{Bmatrix}^{-1}$$

where $\lambda = (L+J)/2$ for $L \neq J$ or $\lambda = L + 1/2$ if $L = J$ and δ is Kronecker delta. The numerical values of the 6-j symbols can be found in Reference (3) and the triplet state expansion becomes

$$|ns\varepsilon p,\ ^3P,\ J=1\rangle = \frac{1}{\sqrt{3}} \left(\sqrt{2}\ |ns_{1/2}\ \varepsilon p_{1/2},\ J=1\rangle - |ns_{1/2}\ \varepsilon p_{3/2},\ J=1\rangle\right). \quad \text{(B7)}$$

The dipole matrix elements for photoionization from the ground state $|ns^2,\ ^1S,\ J=0\rangle$ $(=|ns_{1/2}\ ns_{1/2},\ J=0\rangle)$ to the singlet and triplet final states are given by

$$\langle ns\varepsilon p,\ ^1P,\ J=1|D_0^{(1)}|ns^2,\ ^1S,\ J=0\rangle$$

$$= \frac{1}{\sqrt{3}}\{\langle ns_{1/2}\ \varepsilon p_{1/2},\ J=1|D_0^{(1)}|ns_{1/2}\ ns_{1/2},\ J=0\rangle$$

$$- \sqrt{2}\ \langle ns_{1/2}\ \varepsilon p_{3/2},\ J=1|D_0^{(1)}|ns_{1/2}\ ns_{1/2},\ J=0\rangle\} \quad \text{(B8)}$$

with a similar expression for excitation to the $^3P_1$ final state. From the definitions of the dipole amplitudes D_α given in Appendix A and Equations (B5), (B7) and (B8), we obtain the dipole amplitudes for the $^1P_1$ and $^3P_1$ final states

$$D_S = \frac{1}{\sqrt{3}} (D_{1/2} + \sqrt{2}\, D_{3/2}) \tag{B9a}$$

$$D_T = \frac{1}{\sqrt{3}} (\sqrt{2}\, D_{1/2} - D_{3/2}) \tag{B9b}$$

where the subscripts S and T refer singlet and triplet states. Comparison of the above expressions with the equations for the scattering amplitudes in jj coupling (Eqns (9a) and (9b), Chapter III) leads to the final result

$$\bar{S}(0) = D_S \exp[i(\sigma+\pi/2)] \tag{B10a}$$

$$\bar{S}(1) = D_T \exp[i(\sigma+\pi/2)] \tag{B10b}$$

where σ is coulomb phase shift. Hence, the parity favored channel ($\bar{S}(0)$) corresponds to excitation to $^1P_1$ continuum states and the parity ($\bar{S}(1)$) unfavored transitions lead to $^3P_1$ final states.

References Appendix B

1. B. W. Shore and D. H. Menzel, Principles of Atomic Spectroscopy (Wiley, New York, 1968), p. 364.

2. A. R. Edmonds, Angular Momentum in Quantum Mechanics (Princeton University Press, Princeton, 1960), pp. 107-8.

3. M. Rotenberg, R. Bivins, N. Metropolis and J. K. Wooten, The 3-j and 6-j Symbols (Technology Press, M.I.T., 1959).

Chapter IV

The Photoelectron Angular Distributions of HBr and HI at $h\nu = 21.2$ eV*

Abstract

The photoelectron angular distributions for the $^2\Pi_{3/2,\ 1/2}\ (p\pi)^{-1}$ and $^2\Sigma^+_{1/2}\ (p\sigma)^{-1}$ ionic states of HBr and HI have been measured at a photon energy of 21.2 eV. The asymmetry parameters for the highly localized $p\pi$ orbitals closely follow those of the "lone pair" orbitals of the related CH_3X molecules and the outer np atomic orbitals of the corresponding united atoms. Furthermore, the asymmetry parameters for the $^2\Pi_{3/2}$ and $^2\Pi_{1/2}$ states were found to be equal (within experimental uncertainty), despite the large spin-orbit splittings of these heavy molecules. Finally, the asymmetry parameters for the $^2\Sigma^+(p\sigma)^{-1}$ ionic states are significantly smaller than for the $^2\Pi(p\pi)^{-1}$ states, in variance with recent predictions based on the angular momentum transfer theory.

---

* This work done in collaboration with S. H. Southworth and D. A. Shirley.

A. Introduction

The importance of relativistic effects in atomic photoionization processes has been the subject of intense theoretical and experimental work in recent years. These studies have included measurements of partial cross sections,[1] angular distributions[2] and spin-polarization[3] and have yielded important new information concerning spin-orbit interactions in continuum processes. Overall, the atomic work indicates that spin-orbit effects are usually small and can be treated as a slight perturbation to the non-relativistic picture.[4] At certain energies, however, particularly near Cooper minima and autoionization resonances, spin-orbit effects are "amplified", leading to very different cross sections or angular distributions than otherwise predicted non-relativistically.[4,5]

In contrast, only a few experiments and virtually no calculations have been performed on the photoionization of molecules containing heavy atoms. Furthermore, most of the photoelectron measurements on relativistic molecules have been concerned primarily with the spin-orbit interactions in the bound states of the neutral[6] or ionic core.[7] More detailed information, including the effects of spin-orbit interactions in the continuum, could be obtained from angular distribution measurements on these same molecules. To date, only the measurements of Carlson, et al.,[8] on the methyl halides (CH_3X, X = F, Cℓ, Br, I) have investigated the angular distributions of relativistic molecules. For CH_3Br and CH_3I only small differences were observed for the asymmetry parameters for the spin-orbit split $^2E_{3/2}$ and $^2E_{1/2}$ ionic states, similar to the results obtained for atomic systems.

To further investigate the effects of spin-orbit coupling on the angular distribution of relativistic molecules, we have measured the asymmetry parameters for HBr and HI at the HeI photon energy ($h\nu$ = 21.2 eV). These molecules are primary candidates for such studies, since they have relatively simple valence electronic structures and exhibit large energy separations between the spin-orbit split $^2\Pi_{3/2}$ and $^2\Pi_{1/2}$ ionic states. In addition, these data permit comparisons to be made with the existing data on HCℓ[8] and the related CH_3X molecular series.

B. Experimental

The experiments were performed on the 8° beam line at the Stanford Synchrotron Radiation Laboratory (SSRL). A complete description of the apparatus has been given in Chapter II. Briefly, a monochromatic beam of highly plane-polarized (>97%) synchrotron radiation (21.24 eV, 8.7 Å band pass) intersected a gas jet formed by effusive expansion through a microchannel array. Sample densities were estimated to be ~2 × 10^{-3} Torr in the interaction volume and the background pressure in the sample chamber and detectors was ≤5 × 10^{-5} Torr. These operating conditions were sufficient to keep signal loss due to electron-molecule scattering to a negligible level. Ejected photoelectrons were detected by two time-of-flight (TOF) analyzers placed at 0° and 54.7° with respect to the photon polarization vector. The TOF analyzers utilized the unique time structure of the storage ring at SSRL (300 psec pulse duration (FWHM), 780 nsec repetition period) and are orders of magnitude more efficient than the more conventional single channel deflection-type analyzers. The output of the two detectors was simultaneously analyzed

with a single time-to-amplitude converter and stored separately in a multichannel analyzer. The resulting β values were corrected for the relative counting efficiencies of the two TOF detectors by calibrating the apparatus with Ne for which β = 2. Additional corrections for the finite solid angles of the detectors (~8 × 10^{-3} sr) and the slight amount of unpolarized radiation (≤3%) were found to be small (<1%) relative to the statistical error in the peak areas.

The HI gas sample was obtained commercially (Matheson) and used without further purification. Although the original intent was to run HI and HBr separately, the HI gas sample contained sufficient HBr impurity so that its spectrum could be obtained simultaneously with the HI spectrum. In addition, a small amount of HCℓ impurity was also observed, although it was too weak to interfere with the spectra of HBr and HI.

Peak areas were obtained by computer deconvolution of the spectra to gaussian distributions. Since the vibrational structure of the ionic states was not well resolved, the reported asymmetry parameters are vibrationally averaged values.

C. Results and Discussion

In (ω,ω) coupling,[9] appropriate for describing the electronic structure of relativistic molecules, the ground state of the heavy HX diatomics can be written as

$$\Psi({}^1\Sigma^+_{0^+}) = A(N)\,|\cdots(s\sigma_{1/2})^2(p\sigma_{1/2})^2(p\pi_{1/2})^2(p\pi_{3/2})^2|$$

where A(N) is the N-electron antisymmetrizer and where we have indicated the united atom designations of the outer valence orbitals.

Photoionization at $h\nu = 21.2$ eV leads to the three ionic states, $^2\Pi_{3/2}$, $^2\Pi_{1/2}$ and $^2\Sigma^+_{1/2}$ corresponding to ionization from the three outermost valence orbitals (the $(s\sigma_{1/2})^{-1}$ ionization will not be observed since its binding energy exceeds 21.2 eV).[10] The 0° and 54.7° TOF spectra of HBr^+ and HI^+ are shown in Figure 1 and are assigned according to the early photoelectron studies by Lenka, et al.[11] The $^2\Pi_{3/2,\ 1/2}$ ionization bands consist primarily of a strong $v' = 0 \leftarrow v'' = 0$ vertical transition in qualitative agreement with the non-bonding, "lone-pair" character of the $p\pi$ molecular orbital. The strong bonding nature of the $p\sigma$ orbitals are reflected by the broad Franck-Condon envelopes of the $^2\Sigma^+_{1/2}$ ionization bands.

The asymmetry parameters, β, for the ionic states of these molecules are summarized in Table 1. The HCℓ results are from Carlson, et al.,[12] and are included for comparison. The error limits of our results for HBr and HI result from the statistical errors incurred in the computer fit of the areas. The larger errors quoted for the HBr β values reflect the more severe overlapping of the $^2\Pi_{3/2}$ and $^2\Pi_{1/2}$ levels. From this table we note first that the β values for ionization from the $p\pi_{3/2}$ and $p\pi_{1/2}$ orbitals are essentially equal within experimental uncertainty. This is not unexpected for HCℓ where the spin-orbit interactions are small, however, for HI this result is somewhat surprising consider g the large spin-orbit splitting (.66 eV) of the $^2\Pi_{3/2}$ - $^2\Pi_{3/2}$ ionic states. Secondly, the $^2\Pi(p\pi)^{-1}$ asymmetry parameters are in every case significantly larger than the corresponding values for the $^2\Sigma^+(p\sigma)^{-1}$ ionic states.

Because the $p\pi$ orbital is highly localized on the halogen, the asymmetry parameters for the $p\pi$ orbitals might be expected to be similar

to other halogen containing molecules which have "lone-pair" orbitals. In Table 2 we compare the β values for the outer "lone-pair" orbitals for the HX and CH_3X series. For the bromine and iodine compounds the β values for these orbitals are essentially identical, although for HCℓ and $CH_3Cℓ$ the asymmetry parameters are very different. This difference in the chlorine compounds was explained by Carlson, et al.,[8] as resulting from the expectation that the pπ orbital in HCℓ is a "purer lone-pair" than the $e(p_x)$ orbital[13] in $CH_3Cℓ$. Based on the results of this work on the heavier molecules, this explanation can be further generalized. Since the pπ atomic orbitals of the bromine and iodine atoms are so much larger and of much lower energy than the atomic orbitals of the carbon and hydrogen atoms, they are not expected to mix strongly in molecular formation. Hence, the pπ and $e(p_x)$ "lone-pair" orbitals retain their np atomic character as reflected in their very similar β values. For the chlorine and especially the fluorine atoms, however, the size and energy of the np atomic orbitals better match those of the carbon and hydrogen atoms; hence, they can be expected to mix more strongly.[14] Therefore, one might expect larger differences in the β values of the "lone-pairs" of the HX and CH_3X molecules for the lighter halogens.

In Table 2 we have also listed the asymmetry parameters for the outermost np shells of the rare gases which represent the united atom limits of the HX molecules. Except for the HCℓ value of Carlson, et al.,[12] the "lone-pair" asymmetry parameters are smaller (15-30%) than the corresponding atomic values, although they do follow the same trend of increasing magnitude with increasing size. The decrease in β(np) as one moves from the united-atom limit can in part be attributed

to "ℓ-spoiling" resulting from the reduction of symmetry from the atom to diatomic molecule. Since only the projection of the orbital angular momentum on the internuclear axis is well-defined (m_ℓ or λ), higher ℓ components can mix with the p(ℓ = 1) atomic orbitals in formation of the $\pi(\lambda = m_\ell = \pm 1)$ molecular orbital. In general, it has been found that for atoms, the higher the ℓ value of the initial orbital the lower the β value.[15] This generalization has been used by Carlson[12] to interpret a wide range of asymmetry parameters for various small molecules by expanding the molecular orbitals over spherical harmonics about some center of symmetry.[16] Although this generalization is more appropriate to the x-ray limit of photoionization, any admixture of higher ℓ-wave components into the π-orbital can be expected to alter the β value away from the atomic limit. A recent one-center expansion calculation on HBr,[17] in which the molecular orbitals are expanded over basis functions centered on the Br atom, indicate some small 4d, 5d and 4f character in the outer π molecular orbital, in support of the above arguments. The "anomalously" large $\beta(p\pi_{3/2})$ and $\beta(p\pi_{1/2})$ values for HCℓ do not follow the above trends for the other HX and CH_3X molecules, including $CH_3C\ell$. Without further experimental work, however, it is impossible to judge whether the HCℓ data actually are different or are incorrect.

From Table 2 we also note that for the heavy HX and CH_3X molecules and the heavy rare gas atoms, the differences between the asymmetry parameters for the spin-orbit components of the pπ and np orbitals are very small. At these kinetic energies even Xe, with a $^2P_{3/2} - {}^2P_{1/2}$ energy separation of 1.31 eV a the branching ratio, $^2P_{3/2}:{}^2P_{1/2}$, of 1.6:1 (compared to the non-relativistic value of 2:1),[18] has β values for the spin-orbit split $^2P_{3/2}$ and $^2P_{1/2}$ ionic states that differ by only 2%.

From recent fully relativistic calculations on Kr and Xe[4,19] one finds that for photon energies below ~50 eV, the energy dependence of $\beta(np_{3/2})$ and $\beta(np_{1/2})$ are very similar. The small differences between $\beta(np_{3/2})$ and $\beta(np_{1/2})$ has therefore been interpreted as resulting primarily from the displacement of the two curves by their difference in binding energies. This simple argument correctly predicts that $\beta(np_{3/2}) > \beta(np_{1/2})$ at photon energies below ~33 eV and $\beta(np_{3/2}) < \beta(np_{1/2})$ at higher energies. Similar behavior is expected for the heavy molecules and from Table 2 we see that $\beta(\omega = \frac{3}{2}) \gtrsim \beta(\omega = \frac{1}{2})$ for the "lone-pair" orbitals for those experiments where the error limits are reasonably small. Hence, the small differences in the asymmetry parameters for ionization of the $p\pi_{3/2}$ and $p\pi_{1/2}$ orbitals are most likely a result of kinetic energy effects and not of variations in their continuum matrix elements or phase shifts. We note, however, that at the kinetic energies at which the comparisons of Table 2 are made, the atomic $np_{3/2}$ and $np_{1/2}$ asymmetry parameters are converging.[19] At higher or lower kinetic energies the difference between the $\beta(np_{3/2})$ and $\beta(np_{1/2})$ parameters are larger; this is particularly true at higher kinetic energies where differences between the radial functions of the more penetrating $np_{1/2}$ and more diffuse $np_{3/2}$ orbitals become important.[4] This suggests that larger deviations between the asymmetry parameters for the $p\pi_{3/2}$ and $p\pi_{1/2}$ orbitals of the HX molecules may also be observed at other photon energies. Such experiments are highly desirable, since these data can in principle yield important information concerning both the bound and continuum wavefunctions.

As pointed out earlier, the β values for the $^2\Sigma^+(p\sigma)^{-1}$ ionic states were consistently lower than those found for the $\Pi(p\pi)^{-1}$ levels. This

result is in disagreement with the qualitative predictions of Cheng[20] in which the asymmetry parameters for $\Sigma^{\pm} \rightarrow \Sigma^{\pm}$ ionization transitions should *always* be greater than that for $\Sigma^{\pm} \rightarrow \Pi$ transitions. This conclusion was based on the application of the angular momentum transfer theory (AMTT)[21] to molecular photoionization. By conservation of parity and total angular momentum, $\Sigma^{\pm} \rightarrow \Sigma^{\pm}$ transitions should include only parity favored contributions while $\Sigma^{\pm} \rightarrow \Pi$ transitions include both parity favored and unfavored processes. Because $\beta = -1$ for a parity unfavored process, these contributions will tend to lower the overall asymmetry parameters for $\Sigma^{\pm} \rightarrow \Pi$ transitions. This analysis is consistent with much of the existing data on small molecules, e.g., N_2, CO and O_2, however, it ignores the details of the dynamical factors, i.e., the dipole matrix elements and phase shifts, which determine the relative weights of the parity favored-to-unfavored contributions to the overall measured value of β(see for example Eqn. 7, Chpt. III). The deviation from the Cheng prediction is mostly likely a result of the fact that $p\pi$ orbitals are essentially atomic and hence have large β values consistent with their atomic counterparts. The asymmetry parameters for the $^2\Sigma^+(p\sigma)^{-1}$ ionic states of the HX^+ ions are more like those obtained for ionization of strongly bonding σ type orbitals of other small molecules with $\beta_{avg}(\sigma) \sim 1$.[12,20]

References Chapter IV

1. See for example: J. A. R. Samson and J. L. Gardner, Phys. Rev. Lett., 33, 671 (1974); F. Wuilleumier, M. Y. Adam, P. Dehz, N. Sander, V. Schmidt and W. Mehlhorn, Phys. Rev., A16, 646 (1977).

2. See for example: D. L. Miller, J. D. Dow, R. G. Houlgate, G. V. Marr and J. B. West, J. Phys., B10, 3205 (1977); J. L. Dehmer, W. A. Chupka, J. Berkowitz and W. T. Jivery, Phys. Rev. A, 12, 1966 (1977); A. Niehaus and M. W. Ruf, Z. Phyz., 252, 84 (1971).

3. See for example: U. Heinzmann, J. Kessler and J. Lorentz, Z. Phys., 240, 42 (1970); U. Heinzmann, G. Schönheuse and J. Kessler, Phys. Rev. Lett., 42, 1603 (1979).

4. T. E. H. Walker and J. T. Waber, J. Phys., B7, 674 (1974).

5. N. A. Cherepkov, Phys. Lett., A66, 204 (1978); W. R. Johnson and K. T. Cheng, Phys. Rev. Lett., 40, 1167 (1978); see also Chapter III of this thesis.

6. S.-T. Lee, S. Süzer and D. A. Shirley, Chem. Phys. Lett., 41, 25 (1976).

7. See for example: R. Manne, K. Wittel and B. S. Mohanty, Mol. Phys., 29, 485 (1975); J. Berkowitz, J. L. Dehmer and T. E. H. Walker, J. Chem. Phys., 59, 3645 (1973); see also Chapter V of this thesis.

8. T. A. Carlson and R. M. White, Faraday Discussions, 54, 285 (1972).

9. G. Herzberg, Spectra of Diatomic Molecules (Van Nostrand Reinhold, New York, 1950), Chpt. V, pp. 337-8.

10. The ($s\sigma_{1/2}$) molecular orbital is expected to be mainly ns atomic character of the halogen atom. The bromine 4s and iodine 5s atomic ionization potentials are 23.9 eV and 20.8 eV, respectively; these lines are too high in energy to be observed with 21.2 eV photons (the $I(5s)^{-1}$ would have a kinetic energy ~.5 eV, which is beyond the detection limits of our apparatus; see Figure 13, Chap. II).

11. J. H. Lemka, T. R. Passmore and W. C. Price, Proc. Roy. Soc., A304, 53 (1968).

12. T. A. Carlson, G. E. McGuire, A. E. Jonas, K. L. Cheng, C. P. Anderson, C. C. Lu and B. P. Pullen, in Electron Spectroscopy, edited by D. A. Shirley (North-Holland, Amsterdam, 1972), p. 207.

13. The designation of the "lone-pair" orbitals of the CH_3X molecules is given by the irreducible molecular symmetry designation e(in C_{3v} symmetry) and its major atomic orbital constituent, the outer np orbitals of the halogen atoms.

14. Non-relativistic *ab initio* calculations on HF and CH_3F indicate substantially more localization of the "lone-pair" orbital on the fluorine atom in HF than in CH_3F. See, P. E. Cade and W. Huo, At. Data and Nucl. Data Tables, 12, 415 (1973); L. C. Snyder and H. Basch, Molecular Wave Functions and Properties (Wiley-Interscience, New York, 1972) C. R. Brundle, M. R. Robin and H. Basch, J. Chem. Phys., 53, 2196 (1970).

15. M. O. Krauss, Phys. Rev., 177, 151 (1968).

16. Expansions of the bound molecular orbitals over central field functions are commonly employed in the theoretical treatments of molecular photoionization. See, A. D. Buckingham, B. J. Orr and J. M. Sichel, Phil. Trans. Roy Soc. Lond., A268, 147 (1970).

17. R. G. A. R. Maclagan, Aust. J. Chem., 28, 927 (1975).

18. F. Wuillumier, M. Y. Adam, P. Dhez, N. Sander, V. Schmidt and W. Mehlhorn, Phys. Rev., A16, 646 (1977).

19. W. R. Johnson and K. T. Cheng, Phys. Rev., A, to be published.

20. E. S. Cheng, J. Phys., B11, L293 (1978).

21. U. Fano and D. Dill, Phys. Rev., A6, 185 (1972).

Table 1. Experimental asymmetry parameters for photoionization ($h\nu$ = 21.2 eV) from the $p\pi_{3/2}$, $p\pi_{1/2}$ and $p\sigma_{1/2}$ orbitals of the HX (X = Cℓ, Br, I) molecules.

X	$p\pi_{3/2}$	$p\pi_{1/2}$	$p\sigma_{1/2}$
Cℓ[a]	1.40(5)	1.40(5)	.75(10)
Br[b]	1.2(2)	1.1(2)	.9(1)
I[b]	1.47(9)	1.47(9)	.89(8)

[a] From Reference (12).

[b] This work.

Table 2. Comparison of β values for the outer "lone-pair" orbitals of the HX and CH_3X molecules and the outermost np orbitals of the corresponding rare gas atoms, A.

	HX	CH_3X[c]	A[d]
X, A	$p\pi_{3/2}$, $p\pi_{1/2}$	$e(p_X)_{3/2}$, $e(p_X)_{1/2}$	$np_{3/2}$, $np_{1/2}$
Cℓ, Ar	1.40[a]	.9	1.26
Br, Kr	1.2, 1.1[b]	1.2, 1.15	1.43, 1.40
I, Xe	1.47, 1.47[b]	1.5, 1.45	1.81, 1.77

[a] From Reference (12).

[b] This work.

[c] From Reference (8).

[d] The $\beta(np_{3/2})$ and $\beta(np_{1/2})$ are for the same kinetic energies as the $^2\Pi_{3/2}$ and $^2\Pi_{1/2}$ states of the HX^+ ions, respectively. The β(npj) data were obtained from theoretical relativistic many-body calculations which are in excellent agreement with the few experimental points available for comparison. See Reference (19).

Figure 1. The 0° and 54.7° TOF spectra of HBr^+ and HI^+ taken at $h\nu$ = 21.24 eV The difference in resolution between the 0° ($\Delta E/E$ = 2.3%) and 54.7° ($\Delta E/E$ = 3.0%) TOF analyzers results from the 54.7° analyzer sampling a larger portion of the interaction volume. See M. G. White, R. A. Rosenberg, G. Gabor, G. Thornton, E. D. Poliakoff, S. H. Southworth and D. A. Shirley, Rev. Sci. Instrum., 50, 53 (1979).

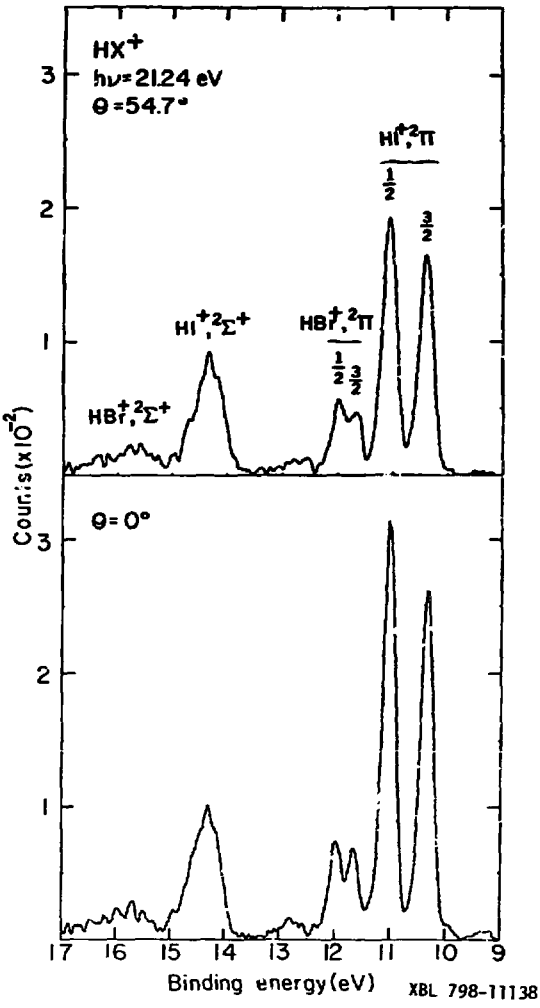
HX+
hν=21.24 eV
θ=54.7°
HI+,2Π
1/2
3/2
HI+,2Σ+
HBr+,2Π
1/2 3/2
HBr+,2Σ+
θ=0°
Counts(x10-2)
3
2
1
17 16 15 14 13 12 11 10 9
Binding energy(eV)
XBL 798-11138

Chapter V

The He I Photoelectron Spectroscopy of Heavy Group IV-VI Diatomics. The GeX (X = O, S, Se, Te) and SnX(X = S, Se, Te) Diatomics*

Abstract

The He I photoelectron spectra of the Group IV-VI diatomics GeO, GeS, GeSe, GeTe, SnS, SnSe, and SnTe are presented. The outermost valence structure of these molecules is similar to that observed in the lighter series CO, CS, etc. of this valence iso-electronic group; in each case a relatively sharp peak is assigned to ionization from the nominally non-bonding 3σ orbital and a broader band to ionization from the bonding 1π orbital. At higher binding energies the spectra exhibit several peaks where only a single peak is expected, from the $(2\sigma)^{-1}$ hole state. This structure is assigned to correlation peaks resulting from configuration interaction among hole states of $^2\Sigma^+$ ($\Omega = 1/2$) symmetry. Semi-empirical CNDO-MO calculations have been performed for these molecules, and the results are used to interpret the observed trends. In addition, a simple molecular orbital model is employed to estimate the importance of spin-orbit coupling in the valence electronic structure of the heavy IV-VI ions.

---

*Work done in collaboration with R. A. Rosenberg, S.-T. Lee and D. A. Shirley (J. Electron Spectroscopy, to be published).

A. Introduction

Considerable effort in ultraviolet photoelectron spectroscopy (UPS) has been focused on elucidating periodic trends in the electronic structure of molecules that are isoelectronic in the valence shells. Recently, the use of high temperature ovens in UPS research has allowed heavier molecules to be studied in the vapor phase. For the (Group VI) dichalcogenides - O_2, S_2, Se_2, Te_2,[1-3] - and the two III-VII series TlX (X = F, Cl, Br, I) and InX (X = Cl, Br, I),[4a-4c] the molecular orbital intensity patterns and relative energy ordering remain similar in the heavier molecules. As the atomic numbers of the constituent atoms increase, however, spin-orbit effects become dominant, leading to large splittings between the Ω substates and in some cases to non-statistical intensity ratios. In addition, the transition from Hund's case (a) coupling in the light molecules to case (c) coupling for the heavier molecules results in a relaxation of symmetry conditions for configuration mixing of multiplets within the initial and final states.[3] Hence, many-electron correlation effects become increasingly important, making a one-electron molecular orbital description inappropriate for relativistic molecules.

The photoelectron spectrum of Bi_2^+ was recorded recently in this laboratory.[5] In addition to the expected large spin-orbit splittings, it showed a reversal in the binding energy ordering of the outermost molecular orbitals relative to that observed for the lighter homologues of this group, N_2 and PN. Further studies on the Group V series are hampered by the instability of the diatomic molecules in the vapor phase. In contrast, the vapors of most of the isoelectronic Group IV-Group VI compounds consist primarily of the IV-VI diatomic molecules at temperatures below 1000°K. Hence, the IV-VI molecules are suitable for further

study of the variation of valence molecular orbital structure with molecular weight.

The He I spectra of the IV-VI molecules GeX (X = S, Se), SnX (X = S, Te), and PbTe have recently been reported by Wu and Fehlner[6] and that of SiO by Colbourn, et al.[7] In the work of Wu and Fehlner,[5] the low binding energy regions of these spectra, containing the outermost $^2\Sigma^+$ and $^2\Pi$ ionization bands, were presented. Except for the GeS^+ spectrum, however, they did not report the weaker structure expected to lie at higher binding energies. Such structure results from electron correlation between the inner $(\sigma)^{-1}$ primary hole states and closely lying excited ionic states as observed in the photoelectron spectra of CO^+ and CS^+. In this work, we present additional He I spectra for the GeX and SnX molecules in which the correlation states are evident, as well as the previously unpublished spectra of GeO, GeTe, and SnSe. Our peak assignments are based on semi-empirical LCAO-MO-SCF calculations, band shape and intensity arguments and comparison with photoelectron data for the lighter members of this series. A simple molecular orbital model is employed to estimate the spin-orbit splittings and the importance of $^2\Sigma^+$ ($\Omega = 1/2$) and $^2\Pi$ ($\Omega = 1/2$) mixing in the final ionic state. Finally, the observed trends are discussed in relation to the general valence electronic structure of the Group IV-VI molecules.

B. Experimental

The spectra were recorded in a modified Perkin-Elmer PS-18 photoelectron spectrometer operating at a nominal energy resolution of 80-90 meV (FWHM) as measured on the Xe $5p_{1/2}$ - $5p_{3/2}$ doublet. The oven and experimental procedure have been described in detail elsewhere.[8a]

Because of continuous deposition of the sample on critical surfaces, the energy resolution and peak position could vary considerably during a single run (which took from one to ten hours). Energy calibration was done by introducing Xe and N_2 together with the sample in separate runs.

The samples were obtained commercially.[8b] All samples were of at least 99.9% purity and were used without further purification. The GeO sample was loaded into the spectrometer under a dry nitrogen atmosphere, while all other samples were loaded in air. Only in the vaporization of the SnS sample were appreciable impurities encountered. Near 400°C, an intense spectrum of $SnCl_2^+$ was observed as identified from the He I UPS data of Evans and Orchard.[9] The intensity of these bands decreased at higher temperatures and eventually disappeared after several hours. To confirm the data obtained with the SnS sample, additional experiments were performed using SnS_2. At elevated temperatures SnS_2 is unstable with respect to disproportionation, i.e., $SnS_2(g) \rightarrow SnS(g) + S_2(g)$. The spectra at lower temperatures (~400°C) were characteristic of S_2^+,[1,2] while at higher temperatures a spectrum identical to that observed in the SnS vaporization was dominant.

The oven temperatures at which the spectra were recorded were: GeO(570°C), GeS(380°C), GeSe(405°C), GeTe(550°C), SnS(610°C), SnSe(590°C), and SnTe(650°C). The thermocouple that monitored the temperature was in contact with a slightly cooler part of the oven; hence, the actual sample temperatures may have been up to 30° higher. At these temperatures the vapor pressures of the MX(g) molecules were between 10 milliTorr and 100 milliTorr as extrapolated from the vapor pressure data for these systems,[10-14] and mass spectroscopic studies have shown in each case that the MX(g) diatomic molecule is the principal component in the vapor phase.[6,10-16]

In high temperature UPS experiments the analysis of the vibrational fine structure is complicated by the fact that the ground state molecule is in a thermal distribution of vibrational levels. This is particularly important for heavy molecules, for which the vibrational frequencies of the neutral ground states are small. The thermal vibrational distributions for the molecules studied in this work are given in Table I. For the heavier members of this series, particularly the MSe and MTe diatomics, the vibrational excitation is extensive, with significant populations up to $v'' = 4$. The effect of this distribution is to wash out the fine structure of the closely lying $^2\Sigma^+$ and $^2\Pi$ levels. In addition, the band shapes yield less information concerning geometry changes upon photoionization because the Franck-Condon envelope is thermally averaged over many initial and final vibrational transitions.

C. Theory

The ground electronic state of a IV-VI diatomic can be represented by the single determinantal wavefunction

$$\Psi(^1\Sigma^+) = A(10)\ \{1\sigma^2\ 2\sigma^2\ 3\sigma^2\ 1\pi^4\} \tag{1}$$

where we have explicitly considered only the outermost filled valence molecular orbitals, and $A(N)$ represents the N-electron antisymmetrizer. Neglecting relativistic interactions at this point, photoionization from the σ shell and any of the π shells will result in $^2\Pi$ and $^2\Sigma^+$ ionic states, respectively. To estimate the binding energies of these orbitals, we have performed semi-empirical CNDO[17] valence molecular orbital calculations for the molecules discussed in this paper. The calculations were carried out using an extensively modified CNDO code parameterized

for atoms through Xe (Z = 54).[18] Calculations employing both nsnp and nsnp(n+1)d basis were performed. The overall molecular orbital character and energy level ordering for these basis sets were similar. Because the unoccupied d orbitals make a negligible contribution to the spin-orbit matrix elements discussed below, only the nsnp basis results are reported here. Equilibrium bond lengths were taken from Reference (19).

The orbital eigenvalues are compared with the experimental binding energies in Tables II and III. The eigenvalues have been empirically reduced by 15% to account for final ionic state relaxation. This factor was estimated by averaging the percentage errors of the CNDO eigenvalues from the experimental binding energies for the lighter members of this series (CO, CS, and SiO). Table IV summarizes the Mulliken population analyses for the valence molecular orbitals.

For the heavier members of both the GeX and the SnX series, spin-orbit interactions become appreciable and remove the degeneracy of the $\Omega = 1/2$ and $\Omega = 3/2$ sublevels of the $^2\Pi$ ionic state. In addition, the ionic states of the heavier molecules are more appropriately described in a (ω,ω) (Hund's case (c)) rather than a (Λ,Σ) (Hund's case (a)) coupling scheme.[20] In the former coupling scheme, the closely spaced $^2\Sigma^+_{1/2}(3\sigma)^{-1}$ and $^2\Pi_{1/2}(1\pi)^{-1}$ ionic states can interact strongly and the resulting $\Omega = 1/2$ states can be expressed as linear combinations of the (Λ,Σ) states; i.e.,

$$\Psi(\Omega = 1/2) = a\Psi(^2\Sigma^+_{1/2}) + b\Psi(^2\Pi_{1/2}). \qquad (2)$$

This interaction has been shown to be very important in rationalizing the observed spin-orbit splittings in the UPS spectra of I_2^+ [21] and the cesium halides.[22]

To estimate the importance of these final ionic state interactions, we used an approximate spin-orbit model based on the CNDO wavefunctions. This method parallels similar semi-empirical calculations by others.[23-25] The molecular spin-orbit operator was approximated as

$$\mathcal{H}_{so} = \sum_N \sum_i \zeta_N^{eff} \vec{\ell}_{iN} \cdot \vec{s}_i \tag{3}$$

where the sums over N and i refer to atomic centers and electrons, respectively, and where ζ_N^{eff} is the effective atomic spin-orbit coupling constant. In a $|\Lambda S \Sigma \Omega\rangle$ basis, the $(3\sigma)^{-1}$ and $(1\pi)^{-1}$ final ionic states can be represented by the single determinants

$$^2\Sigma^+_{1/2}: \quad |0\ 1/2\ 1/2\ 1/2\rangle = A(9)\{\ldots 3\sigma\alpha(5) 1\pi_+\alpha(6) \times 1\pi_+\beta(7) 1\pi_-\alpha(8) 1\pi_-\beta(9)\}$$

$$^2\Pi_{1/2}: \quad |1\ 1/2\ -1/2\ 1/2\rangle = A(9)\{\ldots 3\sigma\alpha(5) 3\sigma\beta(6) \times 1\pi_+\alpha(7) 1\pi_+\beta(8) 1\pi_-\beta(9)\}$$

$$^2\Pi_{3/2}: \quad |1\ 1/2\ 1/2\ 3/2\rangle = A(9)\{\ldots 3\sigma\alpha(5) 3\sigma\beta(6) \times 1\pi_+\alpha(7) 1\pi_+\beta(8) 1\pi_-\alpha(9)\}$$

where the degenerate $-(\Lambda+\Sigma)$ combinations have not been given. Since $\mathcal{H}_{so}$ of Equation (3) is only a one-electron operator, and noting the identity $\vec{\ell}\cdot\vec{s} = \ell_z s_z + \frac{1}{2}(\ell_+ s_- + \ell_- s_+)$, the non-zero matrix elements are readily evaluated as

$$\langle {}^2\Pi_{3/2} | \mathcal{H}_{so} | {}^2\Pi_{3/2} \rangle = \langle 1\pi_-\alpha | \mathcal{H}_{so} | 1\pi_-\alpha \rangle = -A/2 \tag{4a}$$

$$\langle {}^2\Pi_{1/2} | \mathcal{H}_{so} | {}^2\Pi_{1/2} \rangle = \langle 1\pi_-\beta | \mathcal{H}_{so} | 1\pi_-\beta \rangle = A/2 \tag{4b}$$

$$\langle {}^2\Sigma^+_{1/2} | \mathcal{H}_{so} | {}^2\Pi_{1/2} \rangle + \langle 3\sigma\beta | \mathcal{H}_{so} | 1\pi_-\alpha \rangle = \varepsilon \tag{4c}$$

Where A is proportional to the spin-orbit splitting within a given electronic term.[26] The 3σ and 1π wavefunctions were taken from the calculated molecular orbitals of the ground state as a Koopmans' approximation to the hole state wavefunctions. We can then obtain the matrix elements of $\mathcal{H} = \mathcal{H}_0 + \mathcal{H}_{so}$ to give the total interaction matrix

	$^2\Pi_{3/2}$	$^2\Pi_{1/2}$	$^2\Sigma^+_{1/2}$
$^2\Pi_{3/2}$	$E(^2\Pi)-1/2A$	0	0
$^2\Pi_{1/2}$	0	$E(^2\Pi)+1/2A$	ε
$^2\Sigma^+_{1/2}$	0	ε	$E(^2\Sigma^+)$

where $\mathcal{H}_0$ is the electrostatic Hamiltonian. For the purpose of the calculation, $E(^2\Pi)$ was set equal to zero and $E(^2\Sigma^+)$ was varied until the $^2\Pi_{3/2} - {}^2\Sigma^+_{1/2}$ separation resulting from the diagonalization matched experiment. The evaluation of the spin-orbit matrix elements for these molecules is discussed more fully in Appendix C. The values of ζ_N^{eff} and the appropriate matrix elements, as well as the calculated spin-orbit splittings, are summarized in Table V.

D. Results

The He I spectra of the seven molecules studied are shown in Figures 1-5, with the assignments of the prominent bands labeled. The peaks marked S are photoelectron bands from the GeX^+ diatomic produced by the He Iβ satellite line at 23.07 eV. The assignments and experimental binding energies for the GeX and SnX molecules are summarized in Tables II and III, respectively.

1. The GeX Series

Below 12 eV, the spectra of the GeX^+ ions exhibit two close, intense ionization features (Figs. 1 and 2). In this binding energy range, two ionic states corresponding to the $(3\sigma)^{-1}$ and $(1\pi)^{-1}$ hole states are predicted. The UPS spectra of the lighter members of this series, CO,[27] CS,[28] and SiO,[7] characterize the 3σ and 1π MO's as non-bonding and bonding, respectively; the $(3\sigma)^{-1}$ ionization bands consist primarily of a strong $v'' = 0$ to $v' = 0$ transition while the $(1\pi)^{-1}$ band exhibits a broad Franck-Condon envelope with vibrational frequencies lower than in the ground state molecule. On this basis we assign the sharper, narrower band in each of these spectra to the $^2\Sigma^+(3\sigma)^{-1}$ state and the broader band to the $^2\Pi(1\pi)^{-1}$ ionic state. We note that this level ordering is further supported by the CNDO-MO calculations (see Table II).

Figure 3 shows the overlapping bands of the $^2\Sigma^+$ and $^2\Pi$ states of GeO^+ taken with slightly higher resolution (50 meV at 10 eV). Because of the poor counting statistics encountered at higher resolution, it was necessary to add several spectra together and then computer smooth the resulting spectrum to $\sqrt{N}$ statistics. For the $^2\Pi$ state, a single vibrational progression of 675 ± 70 cm^{-1} is observed; the small spin-orbit splitting of ~400 cm^{-1} (see Table V) expected for the $^2\Pi_{1/2}$ and $^2\Pi_{3/2}$ components could not be resolved. This vibrational spacing is roughly 30% less than that of the neutral ground state, in qualitative agreement with its bonding character. At lower binding energies, another regularly spaced progression of 1010 ± 35 cm^{-1} is evident, which includes the strong vertical vibrational transition of the $X^2\Sigma^+(3\sigma)^{-1}$ state. If this progression were the vibrational envelope of the $X^2\Sigma^+$ state, the vertical I.P. would then correspond to a $v'' = 0 \rightarrow v' = 3$ transition. Since the

observed spacing is very close to that of the neutral ground state (985.7 cm^{-1}) and this ionization is from a non-bonding orbital, the internuclear distance of the $X^2\Sigma^+$ should be essentially unchanged from that of the neutral. This is inconsistent with a strong $v'' = 0 \rightarrow v' = 3$ transition since the $v'' = 0 \rightarrow v' = 0$ transition should dominate for an ionization in which the internuclear distance remains approximately constant. A vertical transition of $v'' = 0 \rightarrow v' = 0$ is also consistent with the observed vibrational envelopes of the $X^2\Sigma^+$ states of the other Group IV-VI oxides, CO^+ [27] and SiO^+.[7] A more reasonable assignment of these peaks are that they are "hot bands", arising from photoemission from vibrationally excited neutral GeO. This view is supported by the fact that the observed spacing approximately equals that of the neutral ground state (within experimental uncertainty) and that the relative intensities of these peaks are consistent with the thermal vibrational populations given in Table I. The assignment of these peaks to "hot band" ionizations is tentative since experimental difficulties prevented us from obtaining high resolution spectra at significantly higher temperatures which could help determine the origin of this structure.

Due to the small vibrational frequencies expected for the ionic states ($v' < 500$ cm^{-1}) and the extensive thermal excitation of the neutral ground states (see Table I), the vibrational structure of the heavier GeX^+ ions could not be resolved. In addition, the $^2\Pi_{1/2}$ and $^2\Pi_{3/2}$ spin-orbit partners are also not well resolved, even though for $GeTe^+$ this splitting is predicted to be several tenths of an eV (see Table V). The overlap of the vibrationally excited Franck-Condon envelopes is at least partially responsible for the lack of observed structure.

At higher binding energies, a single ionization band corresponding to the $B^2\Sigma^+(2\sigma)^{-1}$ state is predicted (the $(1\sigma)^{-1}$ hole state will not be observed because its binding energy lies above the He I resonance line energy of 21.2 eV). In GeO^+ a weak band is observed at a vertical I.P. of 15.16 eV with vibrational spacing of [illegible] ± 125 cm^{-1}. The structure and low intensity of this band is similar to the $(2\sigma)^{-1}$ ionization observed in CO^+, CS^+, SiO^+, N_2^+, and P_2^+. A decrease in the vibrational spacing relative to the neutral ground state (986 cm^{-1}) is in agreement with the slight bonding character of the 2σ orbital as predicted by the molecular orbital calculations. The small intensity of the $(2\sigma)^{-1}$ level results presumably from the low photoionization cross section of the Ge 4s atomic orbital which largely comprises the 2σ molecular orbital (see Table IV).

The spectra of the GeS, GeSe, and GeTe, however, show several weak ionization bands in this energy range. This structure is attributed to primary photoelectric excitation of the GeX^+ ions rather than to inelastic processes, because the relative intensities of these bands were invariant with temperature. These peaks are tentatively assigned to correlation or configuration interaction (CI) satellites[29] arising from many-electron effects involving the $(2\sigma)^{-1}$ primary hole state. Similar CI states have been observed in the soft x-ray and He I and He II spectra of CO^+,[30] N_2^+,[31] and CS^+.[28] From theoretical studies on these lighter homologues,[32] however, we expect one of the CI levels to be predominantly $(2\sigma)^{-1}$ primary hole state in character. If we assign the band at 15.16 eV in GeO^+ to the $B^2\Sigma^+(2\sigma)^{-1}$ hole state, then the binding energy of the 2σ orbital in the heavier molecules should lie below ~15 eV, because the atomic ionization potentials decrease as one proceeds down the GeX series.

Applying this reasoning and using the calculated binding energies of the 2σ orbitals given in Table II, we have tentatively assigned the $B^2\Sigma^+(2\sigma)^{-1}$ states for the GeX^+ ions. The fact that the intensity of the $(2\sigma)^{-1}$ hole state is shared nearly equally among several bands in the spectra of $GeSe^+$ and $GeTe^+$, however, indicates that configuration mixing is much greater than that found for the CX^+ homologues. Therefore, the designation of one of these levels to the $(2\sigma)^{-1}$ ionic state can be considered only tentative.

Configuration interaction calculations for CO^+, CS^+, and N_2^+ [32] indicate that the excited ionic configuration most strongly coupled to the single-hole $^2\Sigma^+$ ionic state is

$$\Psi(^2\Sigma^+) = A(9)\{1\sigma^2\ 2\sigma^2\ 3\sigma^1\ 1\pi^3\ 2\pi^1\}.$$

Satellite lines based on this configuration derive their intensities from both the $(2\sigma)^{-1}$ and $(3\sigma)^{-1}$ primary hole state although those satellites associated with the $(2\sigma)^{-1}$ hole state are found to be more intense. A more complete assignment of the correlation states is severely hampered by the lack of additional theoretical or experimental information on the highly excited ionic states of the GeX^+ ions. The situation is further complicated by the fact that these molecular ions are best described in Hund's case (c) coupling, in which $\Omega = 1/2$ excited states ($^2\Sigma^-_{1/2}$, $^2\Pi_{1/2}$, $^4\Delta_{1/2}$, etc.) may also interact with the $(2\sigma)^{-1}$ and $(3\sigma)^{-1}$ hole states.

In addition to the features ascribed to the GeX^+ diatomics, our spectra of both GeO^+ and $GeTe^+$ contain ionization bands from other species. For the temperature range in which the GeO^+ spectrum was taken, the vapor has been reported to consist of the $(GeO)_{n=1,2,3}$ species in the approximate ratio 3:1:1.[10] The intensities of the bands at 8.5 - 11 eV and

13 - 14 eV in the GeO^+ spectrum varied with temperature independently of the intense features at 11.4 eV: these bands are thus clearly not associated with GeO^+. Although they are weaker than the above ratio would imply, they lie at slightly lower binding energies than the main peaks in GeO^+, as might be expected for polymeric species.

To obtain a theoretical estimate of the level structure of these polymeric molecules, CNDO-MO calculations were performed for $(GeO)_2$ and $(GeO)_3$ using the approximate geometries derived from infrared analysis.[33] The resulting eigenvalue spectra of these molecules are concentrated in the regions 8.7 - 11 eV and 13.5 - 16.0 eV. This is in qualitative agreement with both the UPS spectrum and the appearance potential IP's of 8.7 ± 1 eV and 8.6 ± 1 eV for $(GeO)_2$ and $(GeO)_3$, respectively.[10] It seems probable that these weak features in the GeO^+ spectrum are due to the $(GeO)_{n=2,3}$ species.

In addition to direct vaporization, GeTe also undergoes the disproportionation reaction, $GeTe(s) \rightarrow Ge(s) + \frac{1}{2} Te_2(g)$.[16] The presence of Te_2^+ in our spectrum of $GeTe^+$ was readily identified by comparison with the UPS data of Streets and Berkowitz.[3]

2. <u>The SnX Series</u>

The He I UPS spectrum of SnS^+ is shown in Figure 4 and the spectra of $SnSe^+$ and $SnTe^+$ in Figure 5. We note that the same general features and trends observed in the GeX^+ series are evident in these spectra; a sharp narrow band assigned to the $^2\Sigma^+(3\sigma)^{-1}$ ionic state and the broader spin-orbit split $^2\Pi(1\pi)^{-1}$ ionization band. In the spectrum of $SnTe^+$, the $^2\Pi_{1/2}$ and $^2\Pi_{3/2}$ states are clearly discernable and the intensity ratio $^2\Pi_{1/2}$:$^2\Pi_{3/2}$ is greater than the predicted statistical ratio of 1:1. As in the heavier GeX^+ ions, we again note the extensive structure at higher

binding energies, which is tentatively assigned to configuration interaction satellites of the $^2\Sigma^+$ primary hole states. More satellite bands appear, and they cover a wider range of binding energies than in the GeX^+ ions, which is consistent with the larger number of low lying excited valence states found in the absorption spectra of the neutral SnX molecules.[34] The position of the $B^2\Sigma^+(2\sigma)^{-1}$ hole state is indicated for each spectrum, based on the results of the CNDO-MO calculations. Of course no $(2\sigma)^{-1}$ hole state can be said to exist, though several $^2\Sigma^+$ states are apparent: configuration interaction has distributed the $(2\sigma)^{-1}$ state over all of these peaks.

Finally, we note that the spectrum and assignment of the SnS^+ ion reported here differs markedly from that given by Wu and Fehlner.[6] In their work, ionization bands centered at 9.55 eV and 10.2 eV were observed, and the relative intensities of these bands were found to be temperature dependent. The 9.55 eV peak was assigned to the decomposition product, S_2, while the band at 10.2 eV was assigned to the SnS^+ ion. In our studies involving the vaporization of SnS(s), however, no bands attributable to S_2^+[1,2] were observed, in agreement with the vapor pressure data of colin and Drowart,[13] who did not observe $S_2(g)$ in detectable quantities. To check our spectrum of SnS^+ obtained by the direct vaporization of SnS(s), additional experiments employing $SnS_2(s)$ were performed. At temperatures below 450°C, the spectrum of S_2^+ was dominant and the strong $^2\Pi_g$ ionization band of S_2^+ at 9.41 eV masked the spectrum of SnS^+. The spectra at temperatures near 600°C, however, were identical to that found in the SnS(s) vaporization. Furthermore, the band shapes of the $A^2\Sigma^+$ and $X^2\Pi$ levels in our SnS^+ spectrum are very similar to those observed for the other GeX^+ and SnX^+ ions and are

consistent with band shapes expected for nominally non-bonding and bonding molecular orbitals, respectively. Hence, we believe the spectrum given in Figure 4 represents the SnS^+ ion, while the ionization bands observed by Wu and Fehlner must arise at least in part from impurities or high temperature reaction products.

E. Discussion

The sharply peaked bands of the $^2\Sigma^+(3\sigma)^{-1}$ levels of the GeX^+ and SnX^+ ion characterize the 3σ molecular orbital as essentially non-bonding. Furthermore, in a higher-resolution spectrum of GeS^+, Wu and Fehlner reported a small increase in the vibrational spacing ($\Delta\nu \sim 25\ cm^{-1}$) in the $^2\Sigma^+(3\sigma)^{-1}$ band relative to the neutral ground state. This indicates that for GeS^+, at least, the 3σ orbital is actually weakly anti-bonding. In contrast, the calculated overlap populations tabulated in Table III suggest that the 3σ orbital is weakly *bonding* for all GeX and SnX molecules. A similar situation is found in the heavy Group III-VII diatomics (InX, TlX; X = Cl, Br, I) for which the molecular bond is considered somewhat ionic in nature, i.e., $M^+ - X^-$.[4a-4c] For these molecules, which are isoelectronic with the IV-VI series, extended Hückel calculations predict the 3σ orbital to be predominantly (~75%) localized on the In or Tl atom and to be nominally nonbonding. Because of this localization, however, ionization from the 3σ orbital leads to an increase in the ionic character of the III-VII bond, i.e., $M^{++} - X^-$, resulting in a shortening of the bond length and an increase in the vibrational frequency of the $(3\sigma)^{-1}$ hole state. Hence, the shape of the $^2\Sigma^+(3\sigma)^{-1}$ photoelectron peak is characteristic of an anti-bonding orbital.[4b] Although the atomic orbital composition of the 3σ orbital in the IV-VI diatomics is similar to that of the III-VII series, the localization on

the Group IV atom is smaller, giving less ionic character (see Table IV). Thus, the small increase in the polarity of the IV-VI bond upon ionization from the 3σ orbital is somewhat cancelled by the loss of covalent bond overlap. Therefore, in the more ionic IV-VI molecules GeO and GeS (as determined by the extent of charge transferred from the Group IV to the Group VI atom), the resulting $^2\Sigma^+(3\sigma)^{-1}$ photoelectron bands will have the structure of a slightly anti-bonding level, while in the more covalent molecules, MSe and MTe, these bands will have the structure of a non-bonding orbital.

A similar argument explains the large decrease in vibrational spacing (~30%) in the $^2\Pi(1\sigma)^{-1}$ ionic state of GeO^+, even though the overlap population of the 1π orbital is small compared to that in most of the other GeX and SnX molecules. Because the 1π orbital is primarily localized on the Group VI atom (>70%), ionization from this orbital decreases the ionic character of the bond, and therefore increases the bond length. Hence, the $^2\Pi$ band exhibits a broader Franck-Condon envelope and smaller vibrational frequency than would otherwise be expected.

For both the GeX and SnX series, an energy stabilization of the 3σ orbital relative to the 1π orbital develops with increasing molecular weight. A similar trend was observed in the (isoelectronic) Group V-V series, in which the $^2\Pi - {}^2\Sigma(3\sigma)^{-1}$ energy ordering reverses between N_2^+ and P_2^+ and their separation increases in going to Bi_2^+. Süzer, et al.,[5] found a linear relationship between the internuclear distance and the energy separation between the $(3\sigma)^{-1}$ and $(1\pi)^{-1}$ ionic states of these V-V molecules. This correlation was based on the interpretation of Price[35] in which the 3σ orbital supplies little bonding energy at short

internuclear distances because the nuclei have been pulled through some of the 3σ electron cloud. Hence, for the light diatomics, e.g., N_2, the 3σ orbital is destabilized relative to the 1π and lies at lower binding energy. As the valence atomic orbitals become larger in the heavier atoms, the internuclear distance increas , thereby increasing (decreasing) the bonding effectiveness of the 3σ orbital (1π orbital).

A similar explanation should apply to the IV-VI diatomics, to explain the large differences between the $^2\Pi - {}^2\Sigma^+(3\sigma)^{-1}$ energy separation in the light CX^+ ions and that in the heavy GeX^+ and SnX^+ ions. Wu and Fehlner suggest that the rapid decrease in the $^2\Pi - {}^2\Sigma^+(3\sigma)^{-1}$ separation from the light to heavy IV-VI molecules results from a sharp decrease in the π-type interaction between the atoms. This conclusion is qualitatively supported by the fact that the 1π CNDO-MO overlap population for CO, .2343, is significantly larger than the overlap populations for the 1π orbitals in the GeX and SnX molecules (see Table IV). The particularly small 1π overlap population of GeO as compared to the other GeX and SnX molecules results from the small atomic pπ overlap due to the large difference in size between the Ge(4p) and O(2p) atomic orbitals. In addition, the overlap population of the 3σ orbital in CO is -.0130, indicating that it is anti-bonding in character, while the overlap populations for the 3σ orbitals in the GeX and SnX molecules are all positive. These trends in overlap populations are consistent with the explanation given by Price[35] to describe changes in the bonding character of 3σ and 1π orbitals between the second row and heavier isoelectronic molecules. Within the GeX and SnX series, however, the relative stabilities of the 3σ and 1π orbitals change only slowly with increasing bond length; the $^2\Pi - {}^2\Sigma^+(3\sigma)^{-1}$ energy difference decreases by 0.71 eV from GeO^+ to $GeTe^+$

with a corresponding increase in bond length of 0.72 Å, while between CO^+ and GeO^+ the energy separation decreases by 2.38 eV for a 0.50 Å bond length increase. The trends within these heavy series are more readily interpreted on the basis of their calculated charge distributions (see Table IV). As noted previously the 1π orbital is localized principally on the chalcogenide while the 3σ orbital is more equally distributed between both atoms. Hence, as one proceeds down the GeX or SnX series, the ionization potentials of the $(3\sigma)^{-1}$ and $(1\pi)^{-1}$ hole states decrease, following the decrease in ionization potential of the Chalcogenide ns and np atomic orbitals. The 1π energy will decrease faster, however, because it has the proportionally higher Group VI atomic character. Finally, the $^2\Pi - {}^2\Sigma^+(3\sigma)^{-1}$ energy separation does not vary linearly with internuclear distance for the IV-VI molecules unlike the isoelectronic V-V diatomics. The simple relationship between atomic orbital overlap and bond length observed for the homonuclear V-V series is less appropriate in the heteronuclear IV-VI molecules because the two atoms have differences in both orbital size and atomic potentials.

If the spin-orbit interaction between the $\Omega = 1/2$ substates is neglected, the constant A defined by Equations (4a) and (4b) would give the energy separation between the $^2\Pi_{1/2}$ and $^2\Pi_{3/2}$ ionic states. The 1π orbital is predominantly chalcogenide in character; hence the calculated A values reflect the spin-orbit splitting of the np shell of the Group VI atom. With the inclusion of $\Omega = 1/2$ interaction, the agreement with experiment for the $GeSe^+$, $GeTe^+$, and $SnTe^+$ ions is significantly improved while for the others the interaction matrix elements, ε, are small and have little effect. These results are very different from the findings of Berkowitz, et al.,[22] for a similar $^2\Pi_{1/2} - {}^2\Sigma^+_{1/2}$ spin-orbit interaction

in the ionic states of the cesium halides. For the CsX^+ ions, the off-diagonal matrix elements were approximated as $A/\sqrt{2}$ based on the assumption that the matrix elements $\langle^2\Sigma|\zeta(r)|^2\Pi\rangle$ are well approximated by $\langle^2\Pi|\zeta(r)|^2\Pi\rangle$ where $\zeta(r) = Z/r^3$. When applied to the GeX^+ and SnS^+ ions this approximation clearly results in off-diagonal energies which are overall much larger than those calculated by Equation (4c). The relatively small interaction matrix elements obtained by Equation (4c) can be rationalized by examining the wavefunctions for the 3σ and 1π orbitals. The 3σ and 1π molecular orbitals expanded in an LCAO basis are approximately

$$\psi(3\sigma) = c_{IV,3\sigma}\, p\sigma_{IV} - c_{VI,3\sigma}\, p\sigma_{VI} \tag{5a}$$

$$\psi(1\pi) = c_{IV,a\pi}\, p\pi_{IV} + c_{VI,1\pi}\, p\pi_{VI} \tag{5b}$$

where we have ignored the contributions from the $s\sigma_{IV}$ and $s\sigma_{VI}$ atomic orbitals to $\psi(3\sigma)$ since they do not contribute to the spin-orbit interaction matrix element. Because of the anti-symmetric nature of the 3σ orbital, matrix elements given by Equation (4c) will have large contriuting terms of opposite sign. The resulting $\Omega = 1/2$ interaction energy therefore depends on the relative magnitude of these terms which are ultimately determined by the molecular orbital coefficients in Equations (5a) and (5b). In the limit that the coefficients of the atomic orbitals are equal, i.e., a homonuclear molecule, the interaction energy is zero as a consequence of the general selection rule that g and u symmetry states cannot be connected by the totally symmetric spin-orbit operator (see Appendix C). Hence, the heavy homonuclear V-V diatomi ·, such as Bi_2^+ do not exhibit a shift in the $^2\Pi_{u,1/2}$ and $^2\Pi_{u,3/2}$ spin-orbit splitting, because the $^2\Sigma^+_{g,1/2} - {}^2\Pi_{u,1/2}$ interaction is strictly

forbidden. For the cesium halides the outer σ and π orbitals are >90% localized on the halogen atom, so that only the halogen atomic orbitals contribute significantly to the interaction matrix element. Consequently, there is little cancellation and the resulting interaction energy is larger than that for the Group IV-VI diatomics where the localization is not as great. Hence, the approximation $c \sim A/\sqrt{2}$ is more appropriate for the cesium halide systems than the heavy Group IV-VI molecules.

Finally, we noted that in the case in which the $^2\Pi_{1/2}$ and $^2\Pi_{3/2}$ states were well separated, $SnTe^+$ (Fig. 4), the $^2\Pi_{1/2}$:$^2\Pi_{3/2}$ intensity ratio was found to be greater than the statistical ratio of 1:1. This was also observed in the UPS spectrum of Bi_2^+, where the $^2\Pi_{1/2}$:$^2\Pi_{3/2}$ intensity ratio was reported to be 1.5:1.[5] Such a difference in cross section between the $\pi_{1/2}$ ($\omega = \lambda-1/2$) and $\pi_{3/2}$ ($\omega = \lambda+1/2$) components of the bound π molecular orbital is analogous to that observed for the $j = \ell \pm 1/2$ spin-orbit components of relativistic atoms. In Hg^+, for instance, the $^2D_{5/2}$:$^2D_{3/2}$ branching ratio varies between 2.5 and the statistical value of 1.5 for photon energies between 18 eV and 30 eV.[36] For atoms this behavior has been attributed to the differences between the $j = \ell-1/2$ and $j = \ell+1/2$ bound state radial wavefunctions (the $j = \ell-1/2$ radial function lies closer to the nucleus than the $j = \ell+1/2$ component) and the differences in the kinetic energies of the continuum electrons at a given photon energy.[37] These considerations lead to the generalization that the $\sigma_{\ell+1/2}/\sigma_{\ell-1/2}$ branching ratio is greater than the statistical value if the partial cross sections are rising, while the ratio is less than statistical if the cross sections are falling. Extending these arguments to the IV-VI molecules in which $\sigma_{\pi 3/2}/\sigma_{\pi 1/2}$ is

less than unity, the partial cross sections of the $\pi_{1/2}$ and $\pi_{3/2}$ molecular orbitals are evidently decreasing at the He I photon energy (21.2 eV). Furthermore, the kinetic energies of the photoelectrons are much greater than the spin-orbit splitting of the $^2\Pi_{1/2}$ and $^2\Pi_{3/2}$ states at this photon energy. Hence, the cross section differences are primarily caused by the difference in the $\pi_{1/2}$ and $\pi_{3/2}$ bound state wavefunctions and not to relative kinetic energy effects.[37] Additional studies at various photon energies particularly near the $^2\Pi_{1/2,3/2}$ thresholds would provide the necessary data to extend these qualitative theories for the heavy atoms to relativistic molecules.

References Chapter V

1. J. M. Dyke, L. Golob, N. Jonathan, and A. Morris, J.C.S. Faraday II, 71, 1026 (1975).

2. J. Berkowitz, J. Chem. Phys., 62, 4074 (1975).

3. D. G. Streets and J. Berkowitz, J. Electron Spectrosc., 9, 269 (1976).

4. a) J. Berkowitz, J. Chem. Phys., 56, 2766 (1972);

   b) J. Berkowitz and J. Dehmer, J. Chem. Phys., 57, 3194 (1972);

   c) J. L. Dehmer and J. Berkowitz, J. Chem. Phys., 58, 568 (1973).

5. S. Süzer, S.-T. Lee, and D. A. Shirley, J. Chem. Phys., 65, 412 (1976).

6. M. Wu and T. P. Fehlner, J. Am. Chem. Soc., 98, 7578 (1976).

7. E. A. Colbourn, J. M. Dyke, E. P. F. Lee, A. Morris, and I. R. Trickle, Mol. Physics, 35, 873 (1978).

8. a) S. Süzer, M. S. Banna, and D. A. Shirley, J. Chem. Phys., 63, 3473 (1975).

   b) We obtained the GeS, GeSe, SnS, and SnSe samples from Research Organic/Inorganic Chemical Corp., Sun Valley, CA 91352; GeO and SnS_2 from Atomergic Chemetals Corp., Plainview, NY 11803; SnTe from Alfa Products, Beverly, MA 01923; and GeTe from ICN Pharmaceuticals, Inc., Plainview, NY 11803.

9. S. Evans and A. F. Orchard, J. Electron Spectrosc., 6, 207 (1975).

10. J. Drowart, F. Degreve, G. Verhaegan, and R. Collin, Trans. Faraday Soc., 61, 1075 (1965). Vapor pressure data for GeO.

11. V. I. Davydov and N. P. Diev, J. Inorg. Chem. USSR 119, 31 (1957). Vapor pressure data for GeS.

12. L. Chün-Hua, A. S. Pashinkin, and A. V. Novoselova, Russ. J. Inorg. Chem., 7, 496 (1962). Vapor pressure data for GeSe and GeTe.

13. R. Colin and J. Drowart, J. Chem. Phys., 37, 1120 (1962). Vapor pressure data for SnS.

14. C. Hirayama, Y. Ichikawa, and A. M. DeRoo, J. Phys. Chem., 67, 1039 (1963). Vapor pressure data for SnSe and SnTe.

15. R. Colin and J. Drowart, J. Chem. Phys., 68, 428 (1964).

16. R. Colin and J. Drowart, Trans. Faraday Soc., 60, 673 (1964).

17. J. A. Pople and D. L. Beveridge, Approximate Molecular Orbital Theory, (McGraw-Hill, New York, 1970).

18. P. M. A. Sherwood, J. C. S. Faraday Trans. II., 72, 1791 (1976); 72, 1805 (1976).

19. F. J. Lovas and D. R. Lide, Jr., Adv. in High Temp. Chem. 3, 177 (1971), and references therein.

20. G. Herzberg, Spectra of Diatomic Molecules, (Van Nostrand Reinhold, New York, 1950), Chapter V.

21. K. W. Hel, Chem. Phys. Lett., 15, 555 (1972).

22. J. Berkowitz, J. L. Dehmer, and T. E. H. Walker, J. Chem. Phys., 59, 3645 (1973).

23. E. Ishuguro and M. Kobori, J. Phys. Soc. Jap., 22, 263 (1967).

24. R. K. Hinkley, T. E. H. Walker, and W. G. Richards, Mol. Phys., 24, 1095 (1972).

25. F. A. Grimm, J. Electron Spectrosc., 2, 475 (1973).

26. See Reference 20, page 215.

27. D. W. Turner, Molecular Photoelectron Spectroscopy, (Wiley-Interscience, London, 1970), p. 36.

28. D. C. Frost, S.-T. Lee, and C. A. McDowell, Chem. Phys. Lett., 17, 153 (1972); N. Jonathan, A. Morris, M. Okuda, K. J. Ross, and D. J. Smith, Disc. Faraday Soc., 54, 48 (1972).

29. R. L. Martin and D. A. Shirley, Electron Spectroscopy: Theory Techniques and Applications, C. R. Brundle and A. D. Baker, editors (Academic Press, New York, 1977), Vol. 1.

30. U. Gelius, E. Basilier, S. Svensson, T. Bergmark, and K. Siegbahn, J. Electron Spectrosc., 2, 405 (1974).

31. R. Nilsson, R. Nyholm, A. Berndtsson, J. Hedman, and C. Nordling, J. Electron Spectrosc., 9, 337 (1976).

32. W. Domcke, L. S. Cederbaum, W. von Niessen, and W. P. Kraemer, Chem. Phys. Lett., 43, 258 (1976); P. S. Bagus and E.-K. Viinikka, Phys. Rev., A15, 1486 (1977); J. Schirmer, L. S. Cederbaum, and W. Domcke, submitted for publication.

33. J. S. Ogden and M. J. Ricks, J. Chem. Phys., 52, 352 (1970).

34. G. D. Rochester, Proc. Roy. Soc. Lond., 150, 668 (1935); J. W. Walker, J. W. Straley, and A. W. Smith, Phys. Rev., 53, 140 (1938); R. F. Barrow and E. E. Vago, Proc. Phys. Soc., 55, 326 (1943); R. F. Barrow and E. E. Vago, Proc. Phys. Soc., 56, 78 (1944).

35. W. C. Price, in Molecular Spectroscopy, edited by P. Hellpe (Institute of Petroleum, London, 1968).

36. J. L. Dehmer and J. Berkowitz, Phys. Rev., A10, 484 (1974); S. P. Shannon and K. Codling, submitted for publication.

37. T. E. H. Walker, J. Berkowitz, J. L. Dehmer, and J. T. Waber, Phys. Rev. Lett., 31, 678 (1973); T. E. H. Walker and J. T. Waber, J. Phys. B: Atom. Molec. Phys., 7, 674 (1974).

Table I

THERMAL VIBRATIONAL DISTRIBUTIONS OF THE GeX and SnX NEUTRAL GROUND STATES

Molecule	$\nu''(cm^{-1})^a$	T(°C)	Vibrational Population (% of N_o)							
			N_1	N_2	N_3	N_4	N_5	N_6	N_7	N_8
GeO	985.7	570	19	4	1					
GeS	575.8	380	28	8	2	1				
GeSe	406.8	405	43	18	8	3	1			
GeTe	323.4	550	57	33	19	11	6	4	2	
SnS	487.7	510	45	20	9	4	2	1		
SnSe	331.2	590	47	33	19	11	6	3	2	1
SnTe	259.5	650	67	45	30	20	14	9	6	4

a) Reference 20.

Table II. Experimental and theoretical I.P.'s for the GeX (X = O,S,Se,Te) molecules.

Molecule	Ionic State	Experimental I.P.'s (eV)[a] This Work[a]	Wu + Fehlner[b]	Theory (eV)[c]
GeO	$X^2\Sigma^+_{1/2}$	11.25(1)	---	11.61
	$A^2\Pi_{1/2,3/2}$	11.40(5)	---	12.16
	$B^2\Sigma^+_{1/2}$	15.16(2)	---	15.21
	$C^2\Sigma^+_{1/2}$	---	---	30.97
GeS	$X^2\Pi_{3/2,1/2}$	10.34(5)	10.29	10.17
	$A^2\Sigma^+_{1/2}$	10.43(2)	10.39	10.28
	$B^2\Sigma^+_{1/2}$	14.00(4)	---	14.40
	CI State	14.6(1)	---	---
	CI State	15.28(5)	---	---
	CI State	18.86(6)	---	---
	$C^2\Sigma^+_{1/2}$	---	---	22.27
GeSe	$X^2\Pi_{3/2}$	9.8(1)	---	10.14
	$X^2\Pi_{1/2}$	9.95(5)	9.95	
	$A^2\Sigma^+_{1/2}$	10.16(1)	10.20	10.37
	$B^2\Sigma^+_{1/2}$	13.56(5)	13.4	13.92
	CI State	14.0(1)	---	---
	CI State	14.88(5)	14.9	---
	CI State	16.31(5)	---	---
	$C^2\Sigma^+_{1/2}$	---	---	22.50
GeTe	$X^2\Pi_{3/2}$	9.1(1)	---	8.67
	$X^2\Pi_{1/2}$	9.32(2)	---	
	$A^2\Sigma^+_{1/2}$	9.76(1)	---	9.55
	$B^2\Sigma^+_{1/2}$ (?)	13.31(1)	---	13.56
	CI State	13.88(6)	---	---
	CI State	15.20(5)	---	---
	$C^2\Sigma^+_{1/2}$	---	---	20.63

[a]Vertical ionization potentials. Uncertainties are specified in parenthesis.

[b]Ref. (6).

[c]Koopmans Theorem ionization potentials, empirically reduced by 0.85 to reflect final ionic state relaxation.

Table III. Experimental and theoretical I.P.'s for the SnX (X = S,Se,Te) molecules.

Molecule	Ionic State	Experimental I.P.'s (eV)[a] This Work[a]	Ho + Pehlmer[b]	Theory (eV)[c]
SnS	$X^2\Pi_{1/2,3/2}$	9.42(5)	---	9.33
	$A^2\Sigma^+_{1/2}$	9.73(3)	10.20	9.55
	CI State	11.95(5)	---	---
	$B^2\Sigma^+_{1/2}$	13.09(5)	---	13.60
	CI State	14.03(5)	---	---
	CI State	15.46(6)	---	---
	CI State	18.12(6)	---	---
	$C^2\Sigma^+_{1/2}$	---	---	20.80
SnSe	$X^2\Pi_{3/2}$	9.0(1)	---	9.30
	$X^2\Pi_{1/2}$	9.2(3)	---	
	$A^2\Sigma^+_{1/2}$	9.56(1)	---	9.77
	$B^2\Sigma^+_{1/2}$	12.7(1)	---	12.80
	CI State	13.65(5)	---	---
	CI State	14.99(5)	---	---
	$C^2\Sigma^+_{1/2}$	---	---	20.85
SnTe	$X^2\Pi_{3/2}$	8.61(4)	8.65	8.58
	$X^2\Pi_{1/2}$	8.91(2)	8.95	
	$A^2\Sigma^+_{1/2}$	9.30(1)	9.39	9.57
	CI State	10.[illegible](5)	---	---
	CI State	11.02(5)	---	---
	$B^2\Sigma^+_{1/2}$ (?)	11.91(1)	---	12.48
	CI State	12.8(1)	---	---
	CI State	14.33(5)	---	---
	$C^2\Sigma^+_{1/2}$	---	---	18.89

[a]Vertical ionization potentials. Uncertainties are specified in parenthesis.

[b]Ref. (6).

[c]Koopmans theorem ionization potentials. Empirically reduced by 0.85 to reflect final ionic state relaxation.

Table IV.

POPULATION ANALYSIS OF THE VALENCE SHELL

	Atomic Orbital											
	1s				2s				3s			
	II		VI		II		VI		II		VI	
Molecule	S	Pz	S	Pz	S	Pz	S	Pz	S	Pz	S	Pz
GeO	.1055	.1070	.7857	.0909	.1666	.0006	.0778	.4556	.3555	.2962	[illegible]	.3129
GeS	.2048	.0751	.7011	.0177	.6000	.0118	.2015	.1857	.1511	.3297	.0135	.4757
GeSe	.2018	.1014	.5875	.0515	.4583	.0175	.2963	.2285	.1918	.3555	.0225	.3911
GeTe	.3416	.0915	.4958	.0202	.4498	.0130	.3719	.1351	.1522	.3864	.0125	.3561
SnO	.1[illegible]	.0745	.7765	.0093	.6187	.0015	.1[illegible]	.2061	.1495	.4119	.0117	.4277
SnS	.1985	.1060	.6584	.0372	.4795	.0017	.2393	.2796	.2476	.4049	.0181	.3371
SnTe	.2600	.1009	.5557	.0520	.4976	.0139	.3[illegible]9	.1846	.1691	.4125	.0571	.3563

	Atomic Orbital				Bond Orbital Populations			
	1s		1s 2s					
	IV	VI	IV	VI				
Molecule	P	P			1s	2s	S	P
GeO	.2[illegible]	.7162	3.6545	6.3[illegible]	.1[illegible]	.0[illegible]5	.01[illegible]	[illegible]
GeS	.2585	.7690	[illegible]	6.2[illegible]	.5[illegible]	.0[illegible]	.11[illegible]	[illegible]
GeSe	.2612	.7558	3.9078	6.0922	.6[illegible]	.0251	.05[illegible]	[illegible]
GeTe	.2[illegible]	.7510	3.8910	6.1090	.5[illegible]	.0515	.11[illegible]	[illegible]
SnO	.2014	.7955	3.[illegible]	6.2300	.1[illegible]	.0510	.12[illegible]	.1[illegible]
SnS	.2566	.7651	3.8120	[illegible]	.5[illegible]	.0150	.1[illegible]	[illegible]
SnTe	.2212	.7785	3.7916	[illegible]	.5172	.0156	.11[illegible]	.1[illegible]

Table V

Summary of Spin-Orbit Calculations (meV)

Molecule	ζ_{IV}^{eff} [a]	ζ_{VI}^{eff} [b]	A	ε	$^2\Pi_{1/2} - {}^2\Pi_{3/2}$ Theory	Expt [c]
GeO	134	20	49	19	51	-
GeS	131	54	72	5	71	-
GeSe	127	232	204	-60	161	(80)
GeTe	127	521	423	-183	288	230
SnS	319	53	107	-44	98	-
SnSe	312	232	251	15	250	(260)
SnTe	312	521	475	135	390	300

[a] For the Group IV atoms, $\zeta_{IV,P}$ and $\zeta^{+}_{IV,P}$ obtained from Landé Interval rule for the lowest multiplets of the $ns^2\,np^2$ and ns^2np configurations, respectively.

[b] The oxygen and sulfur atomic s.o. parameters taken from reference (25). For Se and Te the intermediate coupling values for $\zeta_{VI,P}$ were used. See S.-T. Lee, S. Süzer, and D. A. Shirley, Chem. Phys. Lett. 41, 25 (1976).

[c] Values in parenthesis are tentative due to the severe overlapping of the $^2\Pi_{1/2}$ and $^2\Pi_{3/2}$ ionization bands.

Figure 1. The He I photoelectron spectra of GeO^+ and $GeSe^+$. The bars above the $B^2\Sigma^+_{1/2}$ ionization band indicate the position of the vibrational levels.

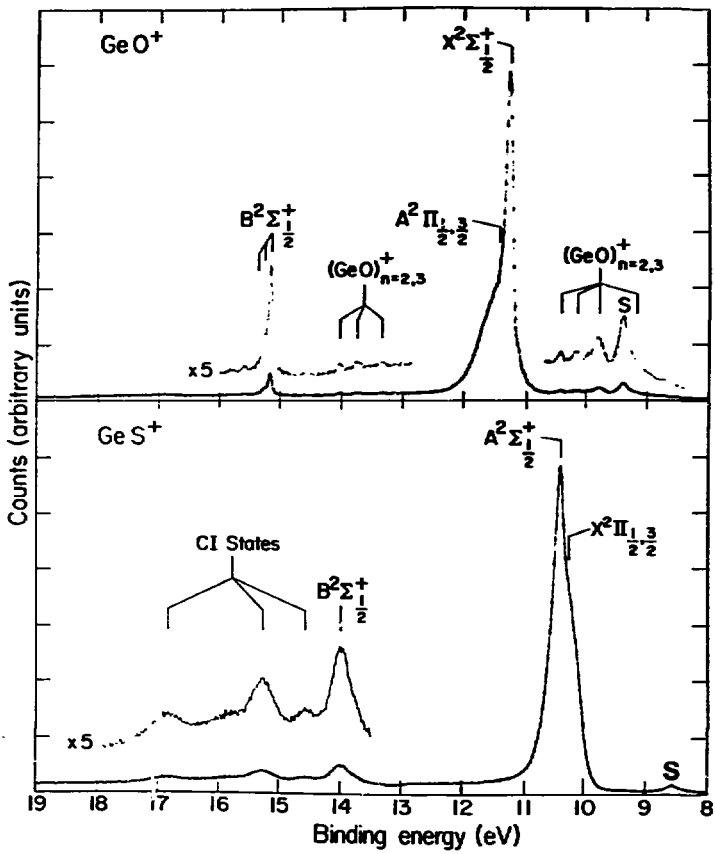

XBL 7712-11403

Figure 2. The He I photoelectron spectra of $GeSe^+$ and $GeTe^+$.

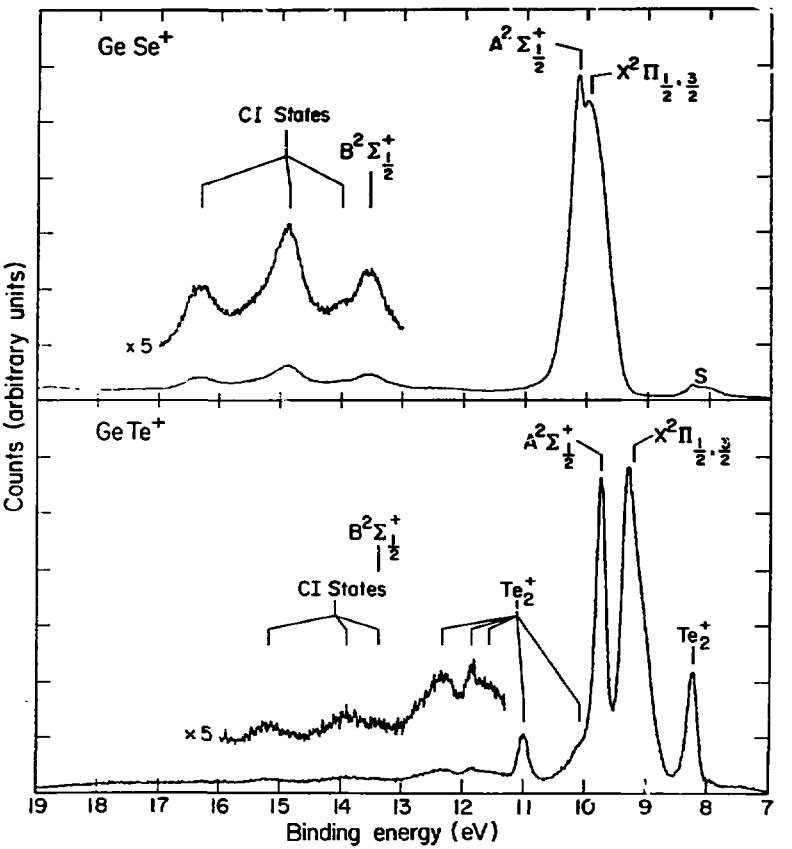

XBL 7712-11404

Figure 3. Higher resolution spectrum of GeO^+ showing the $^2\Sigma^+(3\sigma)^{-1}$ and $^2\Pi(1\pi)^{-1}$ ionization bands on an expanded energy scale.

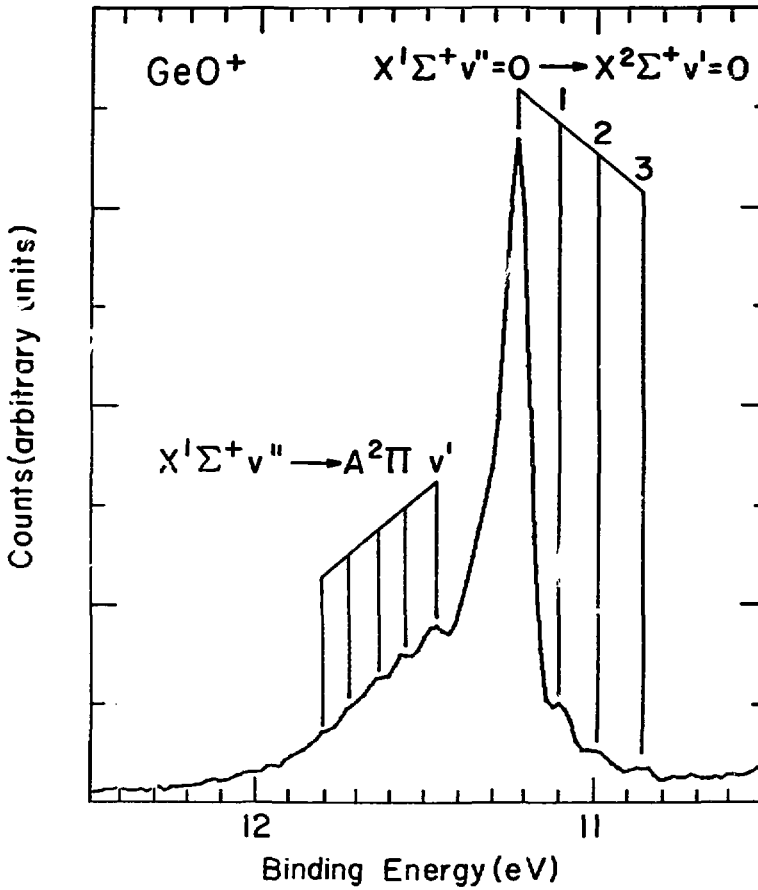
GeO+
X¹Σ⁺v"=0 → X²Σ⁺v'=0
1
2
3
X¹Σ⁺v" → A²Π v'
Counts(arbitrary units)
12
11
Binding Energy (eV)

XBL 793-8794

Figure 4. The He I photoelectron spectrum of SnS^+.

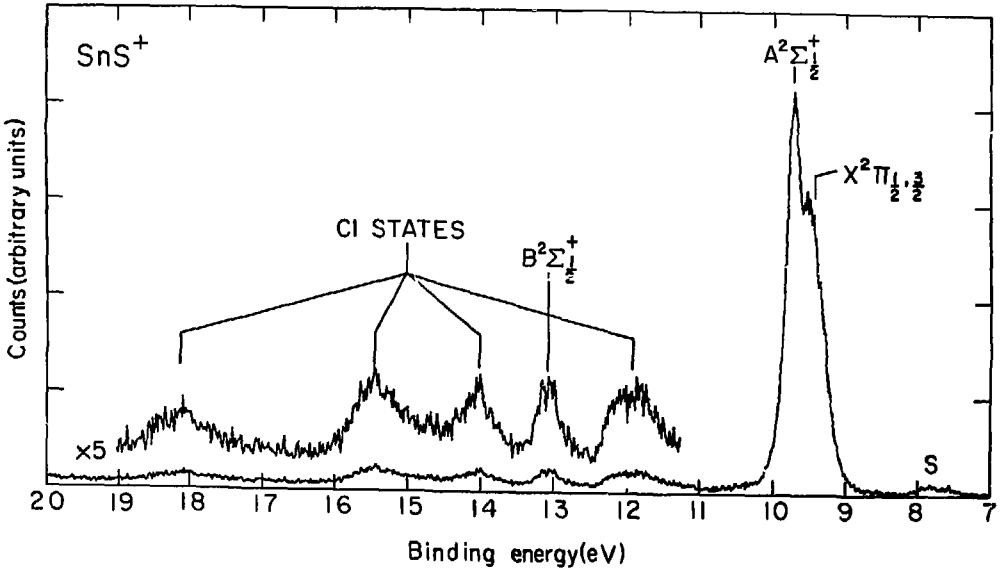

XBL 7712-11404A

Figure 5. The He I photoelectron spectra of $SnSe^+$ and $SnTe^+$. The position of the $B^2\Sigma^+_{1/2}$ state in $SnTe^+$ is uncertain and is shown in parentheses.

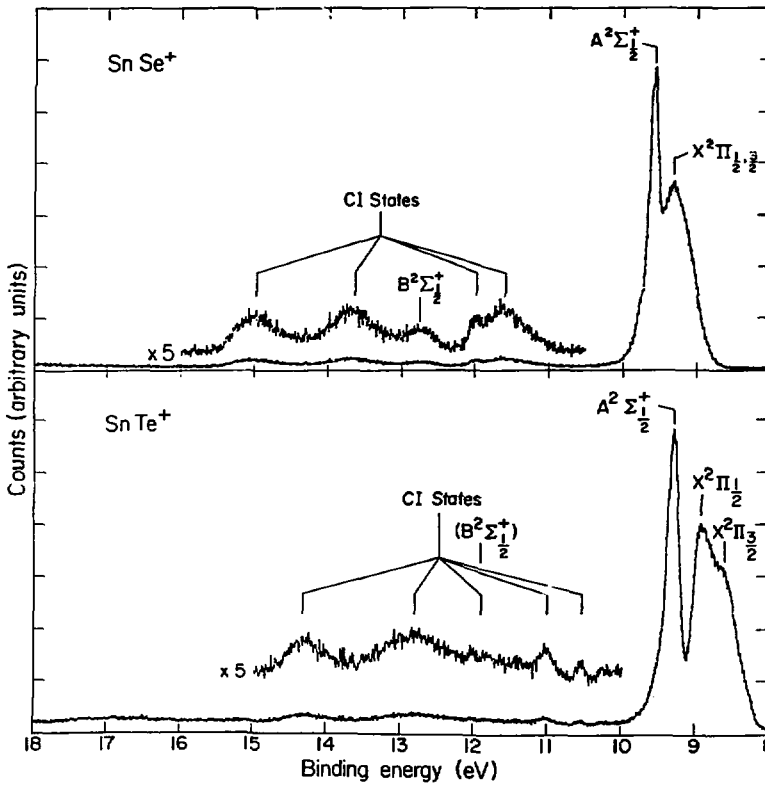
Sn Se+
A²Σ½+
X²Π½,3/2
CI States
B²Σ½+
x 5
Sn Te+
A² Σ½+
X²Π½
X²Π3/2
CI States
(B²Σ½+)
x 5
Counts (arbitrary units)
18
17
16
15
14
13
12
11
10
9
8
Binding energy (eV)
XBL 7712-11405

Appendix C

Evaluation of the $\mathcal{H}_{so}$ Matrix Elements for the Group IV-VI Diatomics

The microscopic spin-orbit hamiltonian for a diatomic molecule is given by[1]

$$\mathcal{H}_{so} = \frac{1}{2}\alpha^2 \sum_i \left(\frac{Z_A}{r_{iA}^3} \vec{\ell}_{iA} \cdot \vec{s}_i + \frac{Z_B}{r_{iB}^3} \vec{\ell}_{iB} \cdot \vec{s}_i \right)$$

$$- \frac{\alpha^2}{2} \sum_{i \neq j} \frac{1}{r_{ij}^3} [\vec{r}_{ij} \times \vec{p}_i (\vec{s}_i) + \vec{r}_{ij} \times \vec{p}_i (2\vec{s}_j)] \qquad \text{(C1)}$$

where α is the fine structure constant and where capital letters refer to nuclei and small letters to electrons. Here the first term represents the spin-orbit coupling of each electron in the coulomb field of the nuclei. The second summation includes both the spin-orbit coupling of each electron i in the coulomb field of electron j, and the interaction of the spin-magnetic moment of electron j with the orbital motion of electron i(spin-other-orbit interaction). Equation (C1) can be rewritten in the form

$$\mathcal{H}_{so} = \mathcal{H}_{so}^{(1)} - \mathcal{H}_{so}^{(2)} \qquad \text{(C2)}$$

where we have separated more explicitly the one- and two-electron operators. The evaluation of the two-electron part of the spin-orbit energy involves integrals over basis functions of the type $\langle ij|\mathcal{H}_{so}^{(2)}|ij\rangle$ and $\langle ij|\mathcal{H}_{so}^{(2)}|ji\rangle$. For atoms the necessary integrations employing analytical or numerical wavefunctions are straightforward, however, for molecules they include multi-center integrations which in general are

more difficult and time consuming. For this reason the total spin-orbit hamiltonian is usually approximated by

$$\mathcal{H}_{so} \sim \mathcal{H}_{so}^{(1)} = \frac{1}{2}\alpha^2 \sum_{i,K} \frac{Z_K}{r_{iK}^3} \vec{\ell}_{iK}\cdot\vec{s}_i. \tag{C3}$$

Recent *ab initio* calculations[2] employing the full hamiltonian (Eqn. (C1) support the approximate form of Equation (C3) since the two-electron integrals tend to cancel so that $\mathcal{H}_{so}^{(2)}$ makes a negligible contribution. In addition, any residual $\mathcal{H}_{so}^{(2)}$ contribution [illegible] to decrease the spin-orbit energy (Eqn. (C2)) and its effect can be roughly interpreted as "screening" the electrons from the full nuclear charge, i.e.,

$$\mathcal{H}_{so} \sim \frac{1}{2}\alpha^2 \sum_{i,K} \frac{Z_{K,eff}}{r_{i,K}^3} \vec{\ell}_{i,K}\cdot\vec{s}_i. \tag{C4}$$

For calculations on the IV-VI diatomics, $\mathcal{H}_{so}$ was approximated by

$$\mathcal{H}_{so} = \sum_{i,K} \zeta_K^{eff}\, \vec{\ell}_{i,K}\cdot\vec{s}_i \tag{C5}$$

where the relationship with Equation (C4) can be made by defining ζ_K^{eff} as

$$\zeta_K^{eff} = \langle\phi_a(1)|\frac{1}{2}\alpha^2 \frac{Z_{K,eff}}{r_{1,K}^3}|\phi_b(1)\rangle \tag{C6}$$

where the ϕ_ℓ are one-electron orbitals. Because ℓ is not a good quantum number for a diatomic molecule (only the projection of ℓ along the internuclear axis, given by λ(or m_ℓ), is conserved), the hamiltonian given by Equation (C5) is not suitable for a direct molecular calculation. For computational purposes, however, the molecular orbitals are expanded over an atomic orbital basis centered on each atom. Hence, matrix elements over molecular orbitals (given by Equations 4(a,b,c), Chapter V)

reduce to a sum over atomic matrix elements like those defined by Equation (C6).

Finally, we note that the molecular (or atomic) orbitals over which the matrix elements are to be calculated are in their complex form, i.e.,

$$\phi_{MO}(\pm\lambda) = e^{\pm i\lambda\phi} f(z,\rho) \tag{C7}$$

where we have employed cylindrical coordinates (z, ρ, ϕ) and $f(z,\rho)$ is the "radial" part (determines the energy) and λ is the orbital angular momentum along the z axis.[3] The π-type molecular orbitals for which the calculations were done, however, were in real form and can be represented by

$$\pi_r = a\pi_x + b\pi_y \tag{C8a}$$

$$\pi_s = a\pi_y - b\pi_x \tag{C8b}$$

and in terms of their atomic composition are

$$\pi_r = a(p_{x,A} + mp_{x,B}) + b(p_{y,A} + mp_{y,B}) \tag{C9a}$$

$$\pi_s = a(p_{y,A} + mp_{y,B}) - b(p_{x,A} + mp_{x,B}). \tag{C9b}$$

Here we have defined the z axis to be collinear with the internuclear axis. The coefficients a, b and m were determined by semi-empirical CNDO-MO calculations as discussed in Chapter V. The relationships between the cartesian and imaginary orbitals are given simply by

$$\pi_x = \frac{\pi_+ + \pi_-}{2} \tag{C10a}$$

$$\pi_y = \frac{\pi_+ - \pi_-}{2i} \tag{C10b}$$

and similar expressions for the atomic orbitals p_x and p_y. Employing Equations (C8)-(C10) we obtain

$$|\pi_{\pm}\rangle = \frac{1}{N}\left(|p_{\pm,A}\rangle + m|p_{\pm,B}\rangle\right) \tag{C11}$$

where N is a normalization constant. The 3σ-type orbitals require no transformation (since $p_\sigma = p_0$) and are given by

$$|\sigma\rangle = c_{A,s}|s_A\rangle + c_{B,s}|s_B\rangle$$

$$+ c_{A,p\sigma}|p_{A,\sigma}\rangle + c_{B,p\sigma}|p_{B,\sigma}\rangle. \tag{C12}$$

where the $c_{K,AO}$ are the molecular orbital coefficients.

With these wavefunctions, the matrix elements of $\mathcal{H}_{so}$ (Eqn. (C5)) can now be determined. The ζ_K^{eff} were taken as empirical quantities and determined from experimental data on the p shells of the particular atoms as discussed in Chapter V. Using the identity $\vec{\ell}\cdot\vec{s} = \ell_z s_z + \frac{1}{2}(\ell_+ s_- + \ell_- s_+)$, the required matrix elements are given by

$$\langle 1\pi_-\alpha|\mathcal{H}_{so}|1\pi_-\alpha\rangle = -\frac{1}{2N^2}\left(\zeta_A^{eff} + m^2\,\zeta_B^{eff}\right) \tag{C13a}$$

$$\langle 1\pi_-\beta|\mathcal{H}_{so}|1\pi_-\beta\rangle = \frac{1}{2N^2}\left(\zeta_A^{eff} + m^2\,\zeta_B^{eff}\right) \tag{C13b}$$

$$\langle 3\sigma\beta|\mathcal{H}_{so}|1\pi\,\alpha\rangle = \frac{\sqrt{2}}{2N}\left[c_{A,p\sigma}\,\zeta_A^{eff} + c_{B,p\sigma}\,m\zeta_B^{eff}\right] \tag{C13c}$$

For the valence-isoelectronic Group V-V mononuclear diatomics the above matrix elements take on a particularly simple form ($m=1$, $N=\sqrt{2}$, $c_{A,p\sigma} = -c_{B,p\sigma}$, $\zeta_A^{eff} = \zeta_B^{eff}$)

$$\langle 1\pi_-\alpha|\mathcal{H}_{so}|1\pi_-\alpha\rangle = -\frac{1}{4}\,\zeta^{eff} \tag{C14a}$$

$$\langle 1\pi_{-}\beta|\mathcal{H}_{so}|1\pi_{-}\beta\rangle = \frac{1}{4}\zeta^{eff} \tag{C14b}$$

$$\langle 3\sigma\beta|\mathcal{H}_{so}|1\pi_{-}\alpha\rangle = 0. \tag{C14c}$$

The result of Equation (C14c) is a simple consequence of the fact that the 3σ and 1π orbitals are of u and g symmetry, respectively, in the $D_{\infty h}$ point group and cannot be connected by the totally symmetric $\mathcal{H}_{so}$ operator.

References Appendix C

1. K. Kayama and J. C. Baird, J. Chem. Phys., 46, 2604 (1967).

2. T. E. Walker and W. G. Richards, Symp. Faraday Soc., 7, 64 (1968); Phys. Rev., 177, 100 (1969).

3. G. Herzberg, Spectra of Diatomic Molecules (Van Nostrand Reinhold, New York, 1950), Chapter V.

Acknowledgements

I would like to take this opportunity to acknowledge and thank the many people who have made my graduate years in Berkeley both scientifically rewarding and just plain fun.

To my wife, Kathleen, I owe my love and deep appreciation for all her support and understanding during these last four years. To our new addition, Sean, whose wide smiles, late bed-times and early mornings kept me constantly cheery (if not constantly sleepy), I owe many happy moments outside the lab.

I would like to thank my research director, Professor David A. Shirley, for his many contributions to the work in this thesis and for providing a stimulating scientific atmosphere in which I could pursue projects of mutual interest.

I have also had the pleasure of working with and learning from the following visiting professors and postdoctoral fellows: Prof. Eckart Matthias, Prof. Harold Basch, Prof. Osama Dabousi, Dr. Shuit-Tong Lee and Dr. Geoffrey Thornton.

I am particularly grateful to the many co-workers within the photoelectron group which I had the good fortune to work with. I would like to thank my closest associates, Dr. Erwin D. Poliakoff, Dr. Richard A. Rosenberg and Mr. Steven H. Southworth for their friendship and invaluable collaboration. Special thanks goes to the other "gas-phasers", Mr. Dennis Trevor and Mr. James Pollard, for their ever helpful suggestions and assistance. Most recently I have had the pleasure of knowing and working with Mr. Paul Kobrin, Mr. Dennis Lindle and Mr. Carlton "Trues" Truesdale.

I should also like to acknowledge the many support personnel who provided invaluable technical assistance in every aspect of my experimental work. Both Mr. Joseph Katz and Mr. George Gabor made major scientific contributions to the design and fabrication of the electronics and electron detectors for the TOF apparatus. Thanks also go to Mr. Read Brandon for his assistance in the construction and testing of the TOF analyzers and also to Mr. Richard Escobales and Mr. Warren Hardnen for their expert help in mechanical design problems.

Finally, I would like to thank Ms. Winifred Heppler and Ms. Karen Janes, both of whom manage to somehow keep our group from attaining a state of enormous entropy.

This work was prepared with the support of the U. S. Department of Energy under Contract W-7405-ENG-48.